



UNIVERSITÀ DEGLI STUDI DI TRIESTE
XXVI CICLO DEL DOTTORATO DI RICERCA IN FISICA

Physical properties and functionalization of low-dimensional materials

Settore Scientifico Disciplinare: FIS/03 Fisica della Materia

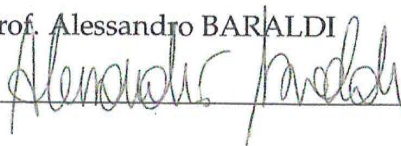
DOTTORANDO
Fabrizio ORLANDO

DIRETTORE DELLA SCUOLA DI DOTTORATO
Chiar.mo Prof. Paolo CAMERINI



SUPERVISORE:

Prof. Alessandro BARALDI



CO-SUPERVISORE:

Dott. Silvano LIZZIT

Anno Accademico 2012-2013

Sommario

Negli ultimi anni abbiamo assistito a rapidi progressi nella ricerca sul grafene, che è uno dei settori più dinamici in fisica dello stato solido, chimica e scienze dei materiali. Il crescente interesse della comunità scientifica verso il grafene, motivato dalle uniche proprietà di questo materiale e dalla vasta gamma di applicazioni per le quali si prospetta un suo utilizzo, ha suscitato un notevole interesse anche verso altri cristalli due-dimensionali (2D) e, in particolar modo, sul nitrato di boro esagonale (*h*-BN). Nonostante il notevole sforzo profuso, una serie di sfide attende ancora la comunità scientifica prima che le potenzialità dei cristalli 2D possano essere pienamente sfruttate, come lo sviluppo di metodi affidabili per la crescita di monostrati atomici di grafene e *h*-BN di alta qualità e la possibilità di modificare in modo controllato la struttura elettronica del grafene.

L'attività di ricerca che ho condotto affronta questi temi focalizzandosi sulla crescita di grafene e *h*-BN sulle superfici dei metalli di transizione – che viene considerata oggi come una delle migliori soluzioni per la produzione su larga scala di strati monoatomici con bassa concentrazione di difetti – e sull'indagine di alcune proprietà fondamentali legate alla presenza del substrato metallico, ma affronta anche problemi legati alla fabbricazione di dispositivi basati sul grafene.

In questo contesto, uno degli obiettivi iniziali è stato far luce sulla morfologia e sulla struttura elettronica del *h*-BN cresciuto sulla superficie Ir(111), oltreché migliorare la strategia per la sintesi di monostrati atomici di *h*-BN di alta qualità.

In una seconda fase, l'attenzione è stata rivolta alla possibilità di controllare finemente le proprietà elettroniche del grafene modificando l'interazione grafene-substrato attraverso l'intercalazione di specie atomiche e molecolari all'interfaccia con il metallo. Questo processo è stato studiato in condizioni di debole (Ir) e forte (Ru) interazione del grafene con il substrato metallico.

Mi sono inoltre occupato di un aspetto maggiormente inerente al settore tecnologico, ovvero lo sviluppo di un metodo per la sintesi diretta di grafene su dielettrici (ossidi).

L'ultimo obiettivo è stato quello di caratterizzare la struttura geometrica di un singolo strato di grafene funzionalizzato con atomi di azoto, che è riconosciuto come una delle vie più dirette per manipolare la chimica di superficie del grafene ed indurre un drogaggio di tipo *n*.

L'uso combinato di una molteplicità di tecniche sperimentali di scienza delle superfici è risultato essere un approccio efficace per conseguire gli obiettivi di questo progetto, avendo fornito l'accesso alla comprensione di diverse proprietà dei sistemi in esame.

Abstract

Recent years have witnessed fast advancements in the research on graphene, which is one of the most active fields in condensed matter physics, chemistry and materials science. The rising interest of the scientific community in graphene, motivated by its fascinating properties and wide range of potential applications, has triggered substantial interest also on other two-dimensional (2D) atomic crystals, and particularly on hexagonal boron nitride (*h*-BN). In spite of much effort, a number of challenges still awaits the scientific community before the full potential of 2D atomic crystals can be exploited, such as the development of reliable methods for the growth of high-quality graphene and *h*-BN single layers or the possibility to tune the graphene electronic structure.

The research activity I have been pursuing faces these requirements by focusing on the growth of graphene and *h*-BN on transition metal surfaces – which appears as the most direct route towards a scalable production of single layers with low concentration of defects – and the investigation of fundamental properties related to the presence of the metal support, but also tackles issues which have a direct link to the fabrication of carbon-based devices.

In this regard, one of the first targets has been to shed light on the morphology and the electronic structure of *h*-BN on Ir(111), and to improve the growth strategy for the synthesis of high-quality *h*-BN layers.

I have subsequently turned my attention to the fine tuning of graphene electronic properties by tailoring the graphene-substrate interaction through intercalation of foreign atoms at the metal interface. This was investigated in the extreme situations of weak (Ir) and strong (Ru) coupling of graphene with the metal support.

I have also focused on an aspect which is related to a specific technological issue, that is, the development of an approach for the direct synthesis of graphene on insulating oxide layers.

Lastly, the structural geometry of single layer graphene functionalized with nitrogen atoms, which is considered as one of the most promising approaches to manipulate graphene chemistry and induce *n*-doping, was also addressed.

The combined use of several surface science experimental techniques has been proved to be of a powerful approach to achieve the targets of this project, having given access to the understanding of different properties of the systems under investigation.

Contents

1	Introduction	1
1.1	The '2D Family'	4
1.2	Our Aim	8
	Bibliography	11
2	Experimental Techniques and Setup	15
2.1	An Introduction to Photoelectron Spectroscopy	15
2.2	The Photoemission Process	17
2.2.1	Fermi Level Referencing	21
2.2.2	The Photoemission Cross-section	22
2.3	Core Level Shifts	24
2.3.1	Surface Core Level Shifts	25
2.3.2	Core Level Photoemission Line Shape	27
2.4	Structural Effects - Photoelectron Diffraction	29
2.5	Absorption Spectroscopy	32
2.6	Experimental Setup	37
2.6.1	The SuperESCA Beamline at Elettra	39
2.6.2	Commissioning of the New Insertion Device	43
	Bibliography	49
3	Epitaxial <i>h</i>-BN on Ir(111)	53
3.1	Introduction	53
3.2	Experimental Details	55
3.3	Results and Discussion	55
3.3.1	Low Temperature Borazine Adsorption	55
3.3.2	From Undissociated Borazine to <i>h</i> -BN	59
3.3.3	<i>h</i> -BN Single Layer	64
	Bibliography	75
4	Intercalated Graphene	81
4.1	Introduction	81
4.2	Experimental Details	84
4.3	Graphene/Ir(111): Results and Discussion	85

4.4	Graphene/Ru(0001): Results and Discussion	94
4.4.1	Graphene Growth	94
4.4.2	Oxygen Intercalation	99
	Bibliography	105
5	Epitaxial Graphene on Oxides	111
5.1	Introduction	111
5.2	Experimental Details	112
5.3	Graphene/SiO ₂ : Results and Discussion	113
5.4	Graphene/Al ₂ O ₃ : Results and Discussion	121
	Bibliography	133
6	N-doped Graphene on Ir(111)	137
6.1	Introduction	137
6.2	Experimental Details	138
6.3	Results and Discussion	138
	Bibliography	145
7	Concluding Remarks and Outlook	147
A	Publications	151
	List of the Acronyms	153

Chapter 1

Introduction

The periodic table counts 114 elements¹, but life on earth needs just five of them: hydrogen, carbon, nitrogen, oxygen and phosphorus, *i.e.* the fundamental constituents of DNA. Among these elements, carbon is undoubtedly the most important, being the key component of every molecule used in the processes of living organisms. The magic of carbon relies in its ability to form different kinds of bonds with neighboring atoms, resulting in a flexibility that gives rise to an unlimited variety of carbon-based structures. It can crystallize forming tetrahedral sp^3 hybrid bonds, such as in the diamond structure, or exist in the sp^2 hybridized bonding configuration, like in graphite.

Carbon was already known to the prehistoric civilizations in the form of charcoal, but reached its moment of greatest glory in the second half of 18th century when it was used, during the industrial revolution, as fuel in steam engines. The experimental investigation of this element has rapidly progressed during the 19th century, when the central role played by carbon in organic matter became clear. In 1865, the German chemist F. A. Kekule realized that benzene is a cyclic molecule. Since then, developments and fundamental discoveries on this element multiplied. More recently, research on carbon gained new interest thanks to the first observation of its 0D and 1D allotropic forms, namely, fullerenes [2] in 1985 and nanotubes [3] in 1991. In 2004, the first isolation of graphene [4], the 2D carbon allotrope, extended the carbon family, which obviously includes also the graphite and diamond 3D forms² (see fig. 1.1). The full range of dimensionality arrangements exhibited by carbon, has given to researchers the opportunity to go

¹At least at the moment! This is the number of elements officially recognized by the International Union of Pure and Applied Chemistry (IUPAC). Very recently, the superheavy element with atomic number 115, ununpentium, has been artificially created by shooting a beam of calcium atoms (20 protons) onto a target made by americium (95 protons) [1].

²The carbon family could get enlarged soon with the arrival of carbyne, a 1D chain of sp -hybridized carbon atoms which has been theoretically predicted to be stable at room temperature [5].

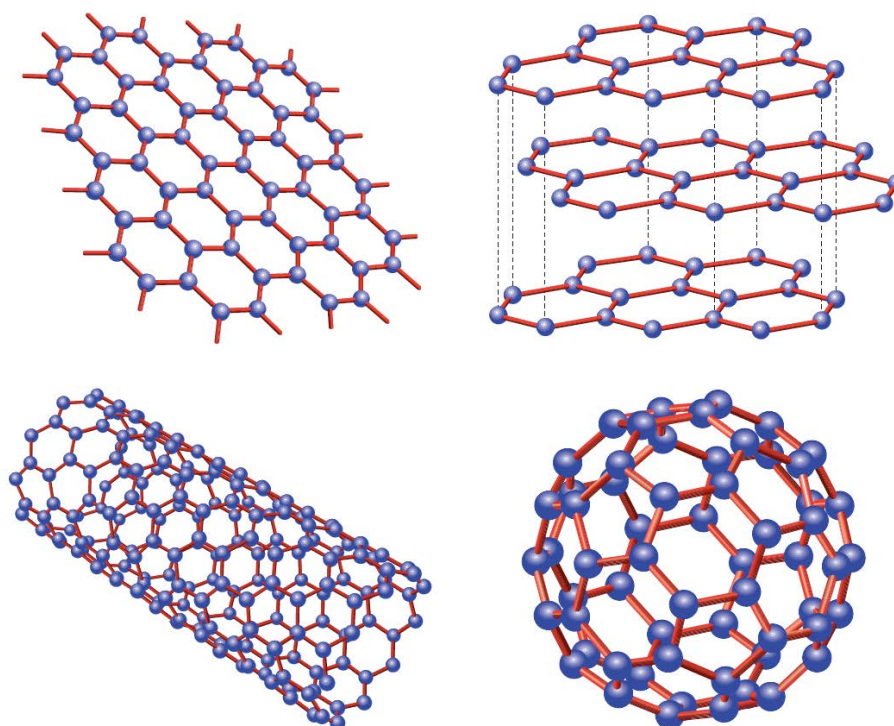


Figure 1.1: Graphene (top left) is a honeycomb network of carbon atoms and is the building block of the carbon family. Graphene sheets can be stacked together to form graphite (top right); carbon nanotubes (bottom left) can be thought as rolled graphene nanoribbons; graphene can also be wrapped into a buckminsterfullerene (bottom right) molecule. Adapted from Ref. [6].

beyond the investigation of 3D bulk systems, providing access to the world of the carbon-based *low-dimensional materials*.

Low-dimensional materials refers to a new class of materials in which the atomic organization along one or more physical dimension(s) is constrained to the nanometer (atomic) scale. When compared to their bulk counterparts, low-dimensional systems exhibit new intriguing phenomena arising from quantum confinement, due to the constraints on the physical dimensions, and surface effects, due to the higher surface-to-volume ratio. Consequently, over the past twenty years, researchers have drawn great attention to the new physical and chemical properties of carbon-based nanosystems, which may be fruitful in a wide range of novel applications, some of which are soon expected on the market. Low-dimensional systems, therefore, are not just a playground for theoreticians.

In the past years, much effort has been spent in the synthesis of 0D

(nanoparticles and nanodots), 1D (nanotubes) and 3D carbon-based materials. The investigation of 2D systems, instead, has remained absent until the development of processes for preparing free-standing graphene [7]. The advancements in the techniques for the synthesis of graphene and, later on, for the manipulation of its properties, have provided new possibilities also for other 2D systems, like hexagonal boron nitride (*h*-BN) and transition metal dichalcogenides. To date, graphene and graphene-like 2D materials are one of the most active fields of research in condensed matter physics and materials science.

The research reported in this thesis concerns the experimental investigation of graphene and *h*-BN single layers epitaxially grown on a variety of metallic substrates, and specifically focuses on the characterization, controllable synthesis and functionalization of these 2D atomic crystals. These fundamental studies play a crucial role in virtue of the high potential that graphene and *h*-BN layers have for various applications.

It's not all graphene. Research on graphene has literally exploded since its isolation was first demonstrated in 2004 [8]. Owing to its extreme properties – including the high carrier mobility at room temperature ($2.5 \times 10^5 \text{ cm}^2 \text{ V}^{-1} \text{ s}^{-1}$) [9], good optical transparency (97.7%) [10], high Young's modulus ($\approx 1 \text{ TPa}$) [11] and excellent thermal conductivity (above $3000 \text{ W m}^{-1} \text{ K}^{-1}$) [12] – and unique band structure, *e.g.* the charge carriers are massless relativistic particles which exhibit the integer and the fractional quantum Hall effect in magnetic fields [13], the worldwide scientific community not only got immediately interested in fundamental research on this material, but also quickly recognized the great potential of graphene for a number of different applications, kicking off the golden age of materials science. There is no wonder that the two scientists who first performed groundbreaking experiments on graphene, A. K. Geim and K. S. Novoselov, were awarded the 2010 Physics Nobel Prize. Past and recent years have witnessed many breakthroughs in graphene research as well as relevant advancements in its mass production. Thousands of papers have been published covering all topics of graphene research: from characterization of the peculiar physical properties arising from the unusual linear π -band dispersion at the Fermi level, to manipulation of the electronic properties and device applications.

Although some theoretical aspects of the many-body physics have not yet been completely understood, making fundamental research on graphene still intriguing, we can probably state that work on graphene is at present mostly about applications. Furthermore, the attention of the scientists has gradually shifted from 'simple' graphene towards other low-dimensional (2D) atomic materials, including *h*-BN, transition metal dichalcogenides and layered oxides [14, 15]. The common feature of these mate-

rials is that their 3D counterparts are stacked structures, with weak van der Waals interactions keeping together the atomic planes. It is worth mentioning also the group IV element graphene-like single layers, silicene and germanene, that have been observed experimentally quite recently even if a layered 3D crystal of these materials does not exist [14, 16]. Each one of these materials has its own characteristics, so that the 2D atomic crystals' family shows a wide range of electronic properties: from insulating to conducting behaviour.

To take advantage of the full potential of 2D materials, and maybe this is the mostly important issue for device applications, scientists have to develop methods to modify their properties. For instance, physical and chemical properties of these 2D crystals can be fine-tuned by functionalization, intercalation with atomic or molecular species, chemical doping and application of strains or electromagnetic fields. In this way one can think and create a variety of artificial materials that do not exist in nature for a number of applications: spintronics, optoelectronics, for the development of catalysts, chemical and biosensors, supercapacitors, solar cells, lithium ion batteries, just to mention a few. This possibility can be exploited even further if we think to pile up different 2D individual sheets to form new 3D heterostructures. This layer-by-layer multistacking procedure results in an artificial material, a so-called van der Waals heterostructure, with tailored properties that can fit an enormous range of applications [17]. This ultimate technology has been recently proved, with the realization of tunneling transistors based on vertical graphene heterostructures showing very promising characteristics [18].

1.1 The '2D Family'

Graphene. Graphene is a single layer of carbon atoms tightly packed into a 2D honeycomb lattice. It is the basic building block of all other well-known carbon materials: 0D fullerenes (wrapped graphene), 1D nanotubes (rolled graphene) and 3D graphite (stacked graphene). Although the popularity achieved in the last decade, the study of graphene is not new and dates back much longer. Graphene linear energy dispersion at the K -point of the Brillouin zone was theoretically predicted already in 1947 by P. R. Wallace [19]. The properties and growth of 'monolayer graphite' on transition metals were first studied in the late 60's [20, 21]. At that time, graphene was mainly considered as an undesired surface contaminant resulting from hydrocarbons dissociation promoted by the catalytic activity of the metal substrate. Graphene formation on silicon carbide (SiC) was also reported already in 1975 [22]. However, these early surface science studies were not aimed to investigate the electronic properties at all, because 2D materials were predicted to be thermodynamically unstable and,

therefore, could not exist [23, 24]. Only the development of a suitable mechanical exfoliation method, in 2004, allowed to isolate high-quality graphene from highly oriented pyrolytic graphite (HOPG) and to verify the predicted unusual physical properties [8]. This plethora of unique properties includes: the anomalous quantum Hall effect, the ambipolar field effect, the extremely high mobility and ballistic transport at room temperature, just to name a few [25].

Top-down exfoliation methods are commonly used to obtain single or few layers from 3D stacked structures by breaking the relatively weak van der Waals forces that keep the individual atomic planes together. Despite its simplicity, mechanical cleavage of bulk graphite [7] does not meet the requirements for a large-scale graphene production, but allows the preparation of very high-quality samples that are currently used for the investigation of fundamental properties such as ballistic transport, carrier mobility and so on. Liquid-phase exfoliation of graphite [26] results in small flakes, which might contain graphene components with several layers. Nonetheless, this technique is promising for the high volume production, and is therefore still suitable for products like conductive inks, printable electronics and coatings.

Graphene can be also synthesized directly on SiC wafers through an effective bottom-up approach [27]. At very high temperatures, the silicon atoms sublime leaving a graphitized surface. Despite the high quality and the sizeable dimensions of the resulting crystallites, graphene growth on SiC has several drawbacks. These include the high growth temperature, that is not compatible with existing silicon electronics, and the cost of SiC wafers. Chemical vapor deposition (CVD) on metal supports is a very promising approach towards graphene production at large scale, with controllable thickness and excellent electronic properties [28]. This well-established method comprises the catalytic dissociation of hydrocarbons (usually ethylene, methane or acetylene) on the hot metal substrate accompanied by hydrogen desorption and the subsequent assembly of graphene. The process is self-limited to the growth of a single layer because it involves a chemical reaction on the active metal surface and, therefore, is strongly suppressed once the substrate is fully covered with graphene, which is completely inert. This approach allows the synthesis of graphene layers with high degree of purity and large grain sizes, depending on the growth parameters. However, electronic applications need graphene on top of an insulating substrate, rendering a transfer process necessary. The transfer consists in the stabilization of the graphene film by a polymer support combined with etching of the metal template and, eventually, release of the graphene onto a target substrate. This procedure obviously adds complications, since it may introduce defects in the lattice or leave polymer residuals on the graphene surface. It would be desirable to avoid this step, for example, by developing a method that allows graphene growth directly

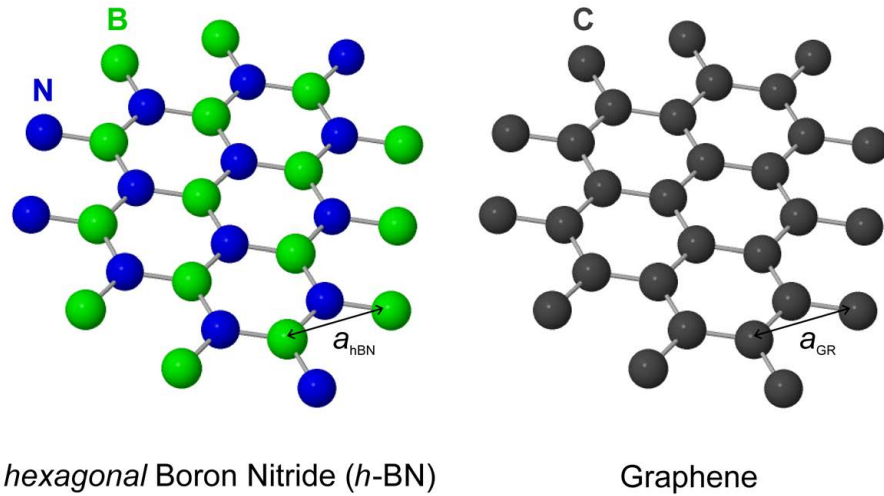


Figure 1.2: Both *h*-BN and graphene are sp^2 hybridized honeycomb structures with very similar lattice constants $a_{\text{hBN}} = 2.50 \text{ \AA}$ and $a_{\text{GR}} = 2.46 \text{ \AA}$, respectively.

onto arbitrary substrates. In this regard, intercalation of a buffer layer, such as Si, potentially provide a new way to decouple CVD graphene from its metallic substrate [29].

As already pointed out, most of the interest in graphene is related to its potential application in next-generation nanoelectronics. Therefore, effort has been devoted to develop new approaches to fine-tune graphene electronic structure and, in particular, to open a band gap: applying electric and magnetic fields to change the density of states, introducing quantum confinement in nanoribbons and quantum dots, varying the concentration and type of defects, bilayer control and tailoring the carrier densities through functionalization with atomic species [30]. However, up to now, all these approaches had limited success. Fundamentally, it is possible to open a band gap, but this leads to the lowering of carrier mobility, which is one of the most striking features of graphene that one would like to exploit.

Hexagonal boron nitride. The *h*-BN single layer is isostructural to graphene, but it is made up of boron and nitrogen atoms alternating in a sp^2 -honeycomb lattice [31]. However, unlike graphene, *h*-BN is an electric insulator with a wide band gap of about 5.9 eV [32].

The approaches for the production of *h*-BN and graphene layers are rather similar. Single or few-layered *h*-BN can be extracted by mechanical or liquid exfoliation from cubic boron nitride [33, 34]. However, these techniques generally suffer either by very low yield, introduction of defects in the lattice or poor control on the number of layers. High-quality *h*-BN

films can be obtained by CVD on hot metal surfaces, including metal foils or single crystal surfaces such as nickel, palladium, platinum and ruthenium [35, 36]. Different precursors have been used: independent nitrogen and boron sources, like diborane (B_2H_6) and ammonia (NH_3) mixtures, or single precursors such as ammonia borane (H_3BNH_3), borazine ($B_3N_3H_6$) or trichloroborazine (Cl_3BNH_3), which have the advantage of a 1:1 B:N stoichiometry.

Owing to its chemical and thermal stability, the *h*-BN nanomesh is very promising as template for trapping molecules in a controlled ordered fashion, thus opening the doors to the engineering of molecular architectures [37]. Moreover, with a lattice constant value very close to that of graphene and a smooth atomic surface free of dangling bonds and charge traps, *h*-BN provides a superior insulating platform to build high-performance graphene devices. Indeed, the use of *h*-BN as a substrate for high-quality graphene electronics has been shown to improve the carrier mobilities and inhomogeneities of one order of magnitude with respect to devices on SiO_2 [38]. Shortly after this discovery, thick boron nitride was used as a gate dielectric in a BN-graphene-BN structure [39], as a tunneling barrier [40] and in graphene-based vertical transistors [18].

It is not hard to imagine that the combination of carbon, boron and nitrogen atoms in the same honeycomb structure could offer many configurations that are intermediate between those of pure graphene (zero-gap semiconductor) and *h*-BN (insulator). Theoretical studies have already anticipated that the electronic properties, and the band gap particularly, would depend on the composition of the three elements in the hexagonal lattice [41]. Obviously this would pave the way to band gap engineering. However, the experimental realization of such structures is still challenging because they tend to form C and BN domains, avoiding the formation of a homogeneous and controlled BCN phase [41].

Other 2D atomic crystals. Beyond graphene and *h*-BN, there are many other known single- and few-layered 2D materials. A representative class of such crystalline structures is that of transition metal dichalcogenides (TMDs), whose general formula is MX_2 , where M is a transition metal atom from group 4-10 and X is a chalcogen [42]. TMDs have received great attention because they exhibit many appealing properties [43]. Depending on the coordination and oxidation state of the metal atom, bulk TMDs can be insulating, such as HfS_2 , semiconducting, like MoS_2 , WS_2 or metallic such as NbS_2 and VS_2 . Exfoliation of these materials into single layers leads to drastic changes in the electronic structure because of lateral confinement effects. For instance, MoS_2 exhibits a transition from an indirect band gap ($E_g = 1.29$ eV) to a direct band gap ($E_g = 1.90$ eV) in going from bulk to single layer, making MoS_2 a promising candidate for optoelectronic de-

VICES in which it interacts with light, particularly in the visible region [44]. There is also interest in using monolayer MoS₂ in FET devices, due to its on/off ratio $> 10^8$ and to a room temperature mobility larger than $200 \text{ cm}^2 \text{ V}^{-1} \text{ s}^{-1}$, which is lower than in graphene but still high compared to other thin-film semiconductors [45]. It is worth noting that research on TMDs focused particularly on exfoliated MoS₂ because of the availability of the parent bulk material, *i.e.* molybdenite crystals, a condition that is not fulfilled for the other metal chalcogenides.

Another interesting group of layered materials is that of 2D oxides, which can be potentially used as high-k dielectrics in next-generation nano-electronics. However, many of these materials, such as Al₂O₃, TiO₂, ZrO₂, HfO₂ and Ta₂O₅, suffer from relatively low values of the dielectric constant ϵ_r , typically < 100 [15]. In this respect, titania and perovskite-like oxide nanosheets exhibit superior high-k performances ($\epsilon_r > 100$) even at thicknesses of few nanometers, which is an essential requirement for the advancement of post-silicon technology [15]. Unfortunately, there is still little information on 2D oxides, thus the design of high-k dielectric thin-films is still a challenging issue to tackle.

1.2 Our Aim

We have seen that for the practical side, CVD on metallic substrates is one of the most promising routes towards the mass production of high-quality graphene and *h*-BN single layers. In this respect, one of the primary goals of the scientific community is to achieve a better control over the CVD conditions to further improve the quality of the resulting monolayers (increased domain size, reduced grain boundaries and ripples, low density of point defects such as vacancies and bi-vacancies, *etc.*) Another relevant breakthrough in CVD technology relates to the possibility of growing 2D crystals on arbitrary surfaces that, at least for graphene, would allow to avoid the transfer step. Therefore, it is clear that CVD synthesis of 2D layers on metal substrates still offers many interesting features to be explored. The purpose of this work is to provide an insight on the epitaxial growth of graphene and *h*-BN on transition metal surfaces, through a detailed investigation of their structural and electronic properties and the introduction of viable routes to overcome the limits set by the current CVD approach.

With the aim of improving the quality of these layers, much effort has been spent in understanding the nature of the bonding with the metal surface. Indeed, the interaction between graphene or *h*-BN with the metal poses some relevant issues because it leads to modifications both in the morphological and in the electronic properties of the overlayer. It is important to stress here that the electronic structure, the strength of the bonding and the degree of corrugation, are strongly correlated quantities that de-

pend on the hybridization, energetic and spatial overlap between the metal states and the π orbitals of the overlayer. In this respect, the situation for *h*-BN is further complicated by its heteroelemental nature, which renders the growth of uniform layers a much more challenging task compared to the case of graphene. Indeed, the elemental polarity (N is more electronegative than B) exhibited by *h*-BN results in a particular alignment and shape of the growing clusters that give rise to rather unique grain boundaries [46]. A deeper understanding of *h*-BN growth mechanism is therefore highly desirable in order to find the optimum approach to grow high-quality defect-free films. We tackled this problem by studying the formation of a *h*-BN single layer on the Ir(111) surface by CVD of borazine (Chapter 3). Firstly, we investigated the low-temperature adsorption of borazine by focusing on the molecular adsorption geometry. The next step consisted in studying borazine dissociation up to the completion of an extended and long-range ordered *h*-BN layer. Finally, we exploited the possibility of tuning the growth parameters (temperature) to enhance the quality of the resulting overlayer.

The already mentioned interaction with the metal substrate is an issue of fundamental importance in epitaxial graphene because, depending on the nature of the bonding (substrate), it changes the doping, *i.e.* the position of the Dirac point with respect to the Fermi energy (E_F), and defines the existence or the absence of the band gap. In the most extreme cases, like for graphene on Ru(0001) or Re(0001), the coupling is sufficiently strong to allow the formation of well ordered graphene layers but, at the same time, to prevent the characteristic electronic properties of graphene from being established. On the other hand, a weak interaction typically leads to the formation of many graphene domains with different orientations. In Chapter 4 we demonstrate that oxygen intercalation is a viable approach to get rid of the graphene/metal coupling both for a weakly and a strongly interacting interface such as Ir(111) and Ru(0001), respectively. In this respect, iridium attracted our interest as a potential substrate for graphene growth because it is a weakly interacting metal on which graphene can be grown with a single-domain structure. We prove that intercalation is possible for a complete graphene layer, under proper conditions of oxygen pressure and substrate temperature, leading to a free-standing layer with unperturbed Dirac cone properties.

The advantages offered by intercalation can be exploited even further to place graphene directly onto an insulating substrate without the need of any transfer process which would introduce defects in the carbon lattice. This fruitful approach is described in Chapter 5. In Section 5.3 it is demonstrated that by a stepwise intercalation of silicon and oxygen below epitaxial graphene on Ru(0001), it is possible to promote the chemical synthesis of a thick SiO₂ layer directly underneath the graphene layer. Furthermore, in Section 5.4 we develop an original shortcut to this approach by taking

advantage of the particular nature of the substrate for the production of the insulating layer. Graphene is first grown on a Ni₃Al(111) alloy surface and, in a second step, exposed to molecular oxygen. This procedure allows the intercalation of oxygen below graphene and the progressive oxidation of the Al atoms at the interface, resulting in the formation of a thin Al₂O₃ buffer layer.

Finally, Chapter 6 is devoted to the study of the chemical doping of graphene by incorporation of nitrogen atoms in the carbon network. Nitrogen-doping of graphene shows promise for a number of different applications in which the tunability of the electronic properties of graphene is required. In this Chapter, the synthesis of N-graphene by nitrogen plasma exposure is presented, together with a detailed investigation of the correlation between the electronic and structural properties of the N-doped graphene layer.

Bibliography

1. Rudolph, D. *et al.* Spectroscopy of Element 115 Decay Chains. *Physical Review Letters* **111**, 112502 (2013).
2. Kroto, H. W., Heath, J. R., O'Brien, S. C., Curl, R. F. & Smalley, R. E. C60: buckminsterfullerene. *Nature* **318**, 162 (1985).
3. Iijima, S. Helical microtubules of graphitic carbon. *Nature* **354**, 56 (1991).
4. Novoselov, K. S. *et al.* Electric field effect in atomically thin carbon films. *Science* **306**, 666 (2004).
5. Liu, M., Artyukhov, V. I., Lee, H., Xu, F. & Yakobson, B. I. Carbyne from first principles: chain of C atoms, a nanorod or a nanorope. *ACS Nano* **7**, 10075 (2013).
6. Castro Neto, A., Guinea, F. & Peres, N. M. R. Drawing conclusions from graphene. *Physics World* **19**, 33 (2006).
7. Novoselov, K. S. *et al.* Two-dimensional atomic crystals. *Proceedings of the National Academy of Sciences of the United States of America* **102**, 10451 (2005).
8. Geim, A. K. & Novoselov, K. S. The rise of graphene. *Nature Materials* **6**, 183 (2007).
9. Mayorov, A. S. *et al.* Micrometer-scale ballistic transport in encapsulated graphene at room temperature. *Nano Letters* **11**, 2396 (2011).
10. Nair, R. R. *et al.* Fine structure constant defines visual transparency of graphene. *Science* **320**, 1308 (2008).
11. Lee, C., Wei, X., Kysar, J. W. & Hone, J. Measurement of the elastic properties and intrinsic strength of monolayer graphene. *Science* **321**, 385 (2008).
12. Balandin, A. A. Thermal properties of graphene and nanostructured carbon materials. *Nature Materials* **10**, 569 (2011).
13. Dean, C. R. *et al.* Multicomponent fractional quantum Hall effect in graphene. *Nature Physics* **7**, 693 (2011).

14. Xu, M., Liang, T., Shi, M. & Chen, H. Graphene-like two-dimensional materials. *Chemical Reviews* **113**, 3766 (2013).
15. Osada, M. & Sasaki, T. Two-dimensional dielectric nanosheets: novel nanoelectronics from nanocrystal building blocks. *Advanced Materials* **24**, 210 (2012).
16. Kara, A. *et al.* A review on silicene – New candidate for electronics. *Surface Science Reports* **67**, 1 (2012).
17. Geim, A. K. & Grigorieva, I. V. Van der Waals heterostructures. *Nature* **499**, 419 (2013).
18. Britnell, L. *et al.* Field-effect tunneling transistor based on vertical graphene heterostructures. *Science* **335**, 947 (2012).
19. Wallace, P. R. The band theory of graphite. *Physical Review* **71**, 622 (1947).
20. Morgan, A. & Somorjai, G. Low energy electron diffraction studies of gas adsorption on the platinum (100) single crystal surface. *Surface Science* **12**, 405 (1968).
21. May, J. W. Platinum surface LEED rings. *Surface Science* **17**, 267 (1969).
22. Bommel, A. V., Crombeen, J. & Tooren, A. V. LEED and Auger electron observations of the SiC(0001) surface. *Surface Science* **48**, 463 (1975).
23. Peierls, R. E. Quelques proprietes typiques des corps solides. *Annales de l'Institut Henri Poincaré* **5**, 177 (1935).
24. Landaue, L. D. Zur theorie der phasenumwandlungen II. *Physikalische Zeitschrift der Sowjetunion* **11**, 26 (1937).
25. Das Sarma, S., Adam, S., Hwang, E. H. & Rossi, E. Electronic transport in two-dimensional graphene. *Reviews of Modern Physics* **83**, 407 (2011).
26. Hernandez, Y. *et al.* High-yield production of graphene by liquid-phase exfoliation of graphite. *Nature Nanotechnology* **3**, 563 (2008).
27. Emtsev, K. V. *et al.* Towards wafer-size graphene layers by atmospheric pressure graphitization of silicon carbide. *Nature Materials* **8**, 203 (2009).
28. Li, X. *et al.* Large-area synthesis of high-quality and uniform graphene films on copper foils. *Science* **324**, 1312 (2009).
29. Mao, J. *et al.* Silicon layer intercalation of centimeter-scale, epitaxially grown monolayer graphene on Ru(0001). *Applied Physics Letters* **100**, 093101 (2012).
30. Zhan, D. *et al.* Engineering the electronic structure of graphene. *Advanced Materials* **24**, 4055 (2012).

31. Paffett, M., Simonson, R., Papin, P. & Paine, R. Borazine adsorption and decomposition at Pt(111) and Ru(001) surfaces. *Surface Science* **232**, 286 (1990).
32. Watanabe, K., Taniguchi, T. & Kanda, H. Direct-bandgap properties and evidence for ultraviolet lasing of hexagonal boron nitride single crystal. *Nature Materials* **3**, 404 (2004).
33. Pacilé, D., Meyer, J. C., Girit, c. O. & Zettl, A. The two-dimensional phase of boron nitride: few-atomic-layer sheets and suspended membranes. *Applied Physics Letters* **92**, 133107 (2008).
34. Coleman, J. N. *et al.* Two-dimensional nanosheets produced by liquid exfoliation of layered materials. *Science* **331**, 568 (2011).
35. Nagashima, A., Tejima, N., Gamou, Y., Kawai, T. & Oshima, C. Electronic structure of monolayer hexagonal boron nitride physisorbed on metal surfaces. *Physical Review Letters* **75**, 3918 (1995).
36. Sutter, P., Lahiri, J., Albrecht, P. & Sutter, E. Chemical vapor deposition and etching of high-quality monolayer hexagonal boron nitride films. *ACS Nano* **5**, 7303 (2011).
37. Corso, M. *et al.* Boron nitride nanomesh. *Science* **303**, 217 (2004).
38. Dean, C. R. *et al.* Boron nitride substrates for high-quality graphene electronics. *Nature Nanotechnology* **5**, 722 (2010).
39. Ponomarenko, L. A. *et al.* Tunable metal-insulator transition in double-layer graphene heterostructures. *Nature Physics* **7**, 958 (2011).
40. Britnell, L. *et al.* Electron tunneling through ultrathin boron nitride crystalline barriers. *Nano Letters* **12**, 1707 (2012).
41. Song, L. *et al.* Binary and ternary atomic layers built from carbon, boron, and nitrogen. *Advanced Materials* **24**, 4878 (2012).
42. Butler, S. Z. *et al.* Progress, challenges, and opportunities in two-dimensional materials beyond graphene. *ACS Nano* **7**, 2898 (2013).
43. Chhowalla, M. *et al.* The chemistry of two-dimensional layered transition metal dichalcogenide nanosheets. *Nature Chemistry* **5**, 263 (2013).
44. Mak, K. F., Lee, C., Hone, J., Shan, J. & Heinz, T. F. Atomically thin MoS₂: a new direct-gap semiconductor. *Physical Review Letters* **105**, 136805 (2010).
45. Radisavljevic, B., Radenovic, A., Brivio, J., Giacometti, V. & Kis, A. Single-layer MoS₂ transistors. *Nature Nanotechnology* **6**, 147 (2010).
46. Lu, J. *et al.* Step flow versus mosaic film growth in hexagonal boron nitride. *Journal of the American Chemical Society* **135**, 2368 (2013).

Chapter 2

Experimental Techniques and Setup

2.1 An Introduction to Photoelectron Spectroscopy

The photoemission spectroscopy technique is based on the photoelectric effect, first discovered by Heinrich Hertz and Wilhelm Hallwachs in 1887, who pointed out that when a solid is exposed to electromagnetic radiation the radiation is absorbed only above a certain threshold frequency, which is specific on the material, and electrons are emitted from the solid. The early attempts to explain this effect within Maxwell's wave theory of light, according to which the energy of the emitted electrons should increase with the intensity of the radiation, finally failed in 1902 when Philippe Lenard observed that the energy of the emitted electrons is proportional to the frequency of the light. In 1905, Albert Einstein solved this problem by postulating the quantum hypothesis for the electromagnetic radiation, for which he was awarded the Nobel Prize in Physics in 1921. According to the Einstein's model, light is composed of discrete *quanta*, that is, photons, rather than continuous waves. A photon transfers its energy completely to the electron in the solid and, if the energy of the electron exceeds a certain threshold energy (work function), it may leave the surface. Later on, between 1950 and 1960, Kai M. Siegbahn developed the Electron Spectroscopy for Chemical Analysis (ESCA) technique in which the photoemission peaks, *i.e.*, the number of the photoemitted electrons measured as a function of their binding energies, are used to determine the composition and chemical state of the sample surface. The development of ESCA, nowadays commonly known as X-ray Photoelectron Spectroscopy (XPS), led to the award of the Physics Nobel Prize in 1981 to Kai M. Siegbahn [1]. Since then, the experimental study of photoelectron spectroscopy has made remarkable progress – especially with the development of high-flux, tunable X-ray sources such as synchrotron facilities (see Section 2.6)

– and has been successfully employed in many fields, including heterogeneous catalysis, materials science or semiconductor technology, just to name a few. In parallel, a deeper theoretical understanding and the development of sophisticated computational methods, allowed to calculate binding energies of very complex systems. Consequently, the combination of high experimental accuracy and theoretical efforts can now yield relevant information about the chemistry of molecules and solids, and makes XPS one of the most powerful and widely used surface characterization tools.

As already discussed, photoemission occurs whenever photons with high enough energy hit the surface and kick out the electrons. Within a one-electron approximation, the kinetic energy (E_{kin}^{vac}) of the photoelectron can be derived from the energy conservation law as

$$E_{kin}^{vac} = h\nu - E_b^F - \phi \quad (2.1)$$

where h is the Planck constant, ν is the frequency of the radiation, E_b^F is the binding energy referenced to the Fermi level (E_F) and ϕ is the specific work function of the material (see fig. 2.4). It is possible to estimate experimentally E_b^F from the XPS spectrum if all the other quantities in eq. 2.1 are known. Since the value of E_b^F in a solid or in a molecule is not far from the corresponding value of the free atom, which is characteristic of each element, XPS can be used for the analysis of the elements in a sample. This *chemical sensitivity* is one of the most striking features of XPS technique. Different types of bond determine the so-called *chemical shift* [2], that is, the deviation of the binding energy from the free atom value. Chemical shifts, which are discussed more in detail in Section 2.3.1, made possible the distinction of atoms or molecules in different structural and/or chemical environments. For instance, these shifts allow to distinguish among chemically non-equivalent atoms within a molecule or, considering photoemission from a solid, to discriminate between surface and bulk atoms [3].

Another important property of photoelectron spectroscopy, namely, the *surface sensitivity*, is related to the inelastic mean free path (IMFP) of electrons in solids. The IMFP is shown in fig. 2.1 as a function of the kinetic energy of the electrons in the range of practical interest for a typical XPS experiment. The behaviour of the experimental points is described by the dashed ‘universal curve’. For energies between 10 and 500 eV, the IMFP is less than 10 Å, which means that only the photoelectrons excited within a depth of 10 Å from the surface can be detected, causing the high surface sensitivity of XPS technique. The universal behaviour of the IMFP in the 10-500 eV interval is due to the main scattering mechanism in this energy window, that is, the excitation of conduction electrons (plasmons) whose density is similar in all metals. At lower energies, electron-hole pair formation and electron-phonon scattering become more important, and the

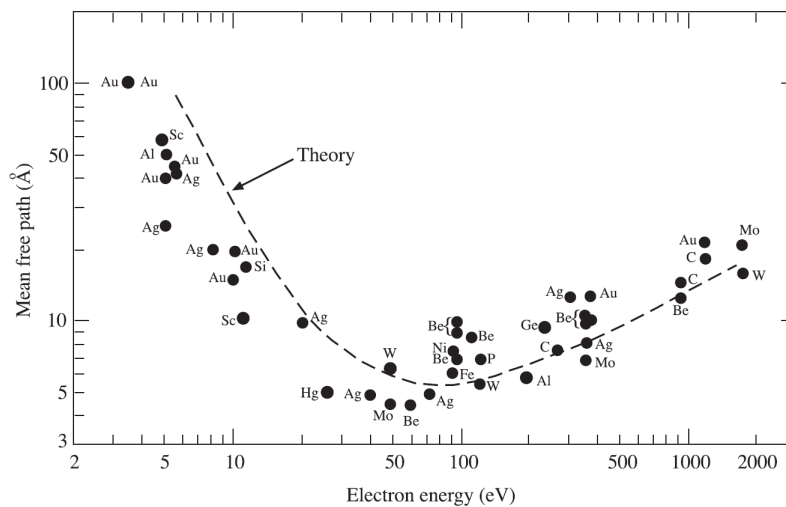


Figure 2.1: Universal curve of the electron IMFP as a function of the electron kinetic energy.

distance between inelastic collisions increases. At higher energies, instead, the rise of the IMFP is due to a decrease of the cross-section for plasmon excitations.

2.2 The Photoemission Process

Photoemission from solids can be described within the so-called *three-step model* [4]:

1. radiation absorption and electron excitation;
2. transport of the photoelectron from the emitter atom towards the surface;
3. electron escape from the surface into the vacuum.

The photoemission process is a photon-induced transition of electrons from initial bound states (occupied orbitals) to empty final states. Considering a system with N electrons, the removal of one electron due to the absorption of a photon with energy $h\nu$ is described as follows

$$\Psi^i(N), E^i(N) \xrightarrow{h\nu} \Psi^f(N-1) + \phi(k), E^f(N-1, k) + E_{kin}, \quad (2.2)$$

where $\Psi^i(N)$ is the wave function of the initial state with N electrons and total energy $E^i(N)$, $\Psi^f(N-1)$ is the final state wave function of the ionic system with energy $E^f(N-1, k)$, $\phi(k)$ is the wave function of the free

electron with kinetic energy E_{kin} . The energy conservation law can be expressed as

$$E^i(N) + h\nu = E^f(N - 1, k) + E_{kin}. \quad (2.3)$$

The binding energy referred to the vacuum level is therefore given by

$$E_b(k) = h\nu - E_{kin} = E^f(N - 1, k) - E^i(N), \quad (2.4)$$

meaning that the binding energy is given by the difference between two total energies and depends on the initial and final state.

The evaluation of the final and initial state wave functions is a complicate theoretical issue. Indeed, such states have to be described by many-electron wave functions. In the Hartree-Fock (HF) approach the N -electron wave function is represented as a self-consistent Slater determinant, *i.e.*, the antisymmetric product of individual electron spin-orbitals. Despite the fact that the HF equations are not true eigenvalue equations, they can be solved by iteration to get the spin-orbital eigenvalues ϵ_k . If we now assume that the spin-orbitals of the $(N - 1)$ -electron system are the same as those of the N -electron system, that is, they do not feel the presence of the hole and no rearrangement of electrons in the sample occurs during the photoemission process, then it is possible to prove that

$$E^f(N - 1, k) - E^i(N) = -\epsilon_k, \quad (2.5)$$

and, by means of eq. 2.4, that

$$E_b(k) = -\epsilon_k. \quad (2.6)$$

Thus the spin-orbital eigenvalue ϵ_k represents approximately the ionization energy of the photoelectron k . This is the essence of the Koopmans' theorem.

In reality, this Koopmans' energy is never measured, because the electrons in the sample are not frozen during the photoemission process. Indeed, the $(N - 1)$ -electron final state undergoes *intra-atomic* relaxation effects due to the presence of the hole, so that the spin-orbitals have to be readjusted according to the new potential. This causes an increase of the kinetic energy of the ejected electron by δE_{rel}^{intra} . In addition, the inclusion of electron correlation, which is not considered in the HF scheme, leads to a negative correction term δE_{corr} . Therefore, a more correct description of $E_b(k)$ is given by

$$E_b(k) = -\epsilon_k + \delta E_{corr} - \delta E_{rel}^{intra}. \quad (2.7)$$

This description would be adequate if the the kinetic energy of the photoelectron is small, thus allowing the system to reach a stable equilibrium. In this case, the core hole potential would be applied adiabatically, corresponding to the slow removal of the photoelectron from the core hole site.

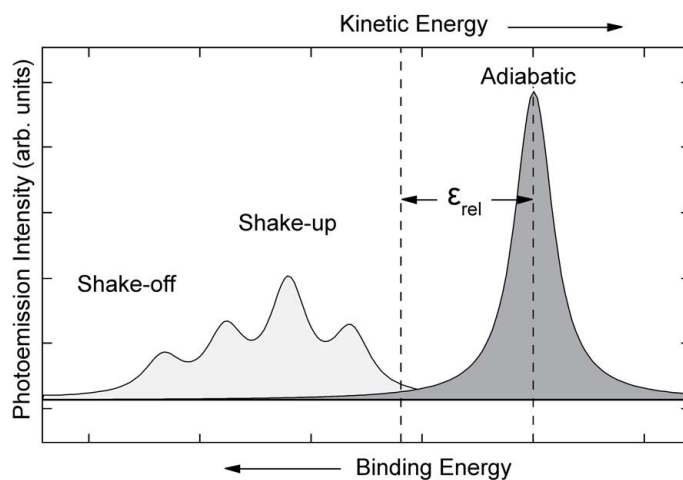


Figure 2.2: Schematic of a core level photoemission spectrum. Besides the main adiabatic peak, if the photoemission process is faster than the electron relaxation, shake-up and shake-off components appear at higher binding energy.

This situation is called the *adiabatic* limit. In reality, the kinetic energy is usually sufficiently high and the photoelectron moves away rapidly from the core hole site. The core hole perturbation is switched on suddenly (*sudden approximation*); the photoemission process is faster than the relaxation mechanism of the $(N - 1)$ -electron system, which is thus left in an excited state. As depicted in fig. 2.2, this mechanism gives rise to lower kinetic energy features, referred as shake-up (excitation to a bound state) or shake-off (excitation to the continuum) satellites, with respect to the main adiabatic peak.

One way to compute more correctly the photoemission spectrum and go beyond the Koopmans' theorem described above, thus taking into account also electron-electron interaction, is to express the final state as a linear combination of the $(N - 1)$ -electron states of the final ion. The coefficients determined by the minimization procedure, known as configuration interaction method [5], give the relative magnitude of shake-up and shake-off satellites. In this regard, it is noteworthy to mention an important sum rule, which states that the sum of the intensities of the shake-up satellites equals the initially expected Koopmans intensity [6]. This can possibly add complication to the quantitative interpretation of XPS spectra. Indeed, the deconvolution of the energy-loss components from the inelastic tail behind the adiabatic peak can be rather difficult, and it is usually easier to measure the area below the main peak. Thus, the value of this area might be not strictly correct for a coverage determination.

So far, we have considered the situation for a free atom. In the case of an atom in a metal, the main difference is due to the presence of the weakly bound valence electrons, which are very mobile and thus can efficiently screen the positive charge of the core hole. In the adiabatic limit, this leads to a positive *interatomic relaxation* shift (δE_{rel}^{inter}) of the photoelectron kinetic energy, and eq. 2.7 becomes

$$E_b(k) = -\epsilon_k + \delta E_{corr} - \delta E_{rel}^{intra} - \delta E_{rel}^{inter}. \quad (2.8)$$

As previously discussed, however, the sudden approximation is more realistic than the adiabatic one, thus we might expect some spectral features reminiscent of shake-up and shake-off satellites. This is indeed the case, but, with respect to the free atom, the excited configurations form a continuum rather than a discrete set of states. Electron-hole pairs around the Fermi level are excited, giving rise to a high binding energy tail behind the adiabatic peak. This effect, first experimentally observed by Hüfner *et al.* [7] on several metals, leads to a characteristic asymmetric line shape of the photoemission peak. This is particularly true for transition metals which, compared to noble metals, exhibits a large asymmetry due to the higher density of states at the Fermi level, that corresponds to a higher probability of electron-hole excitation.

Those just discussed are called *intrinsic losses*, because they occur at the photoemission process itself. However, there is also the possibility for the electrons to incur *extrinsic losses* during their transport from the emitting atom to the surface. These losses lead to similar spectral features (inelastic tail and discrete satellites) as those of the intrinsic losses. Unfortunately, a clear separation between the two effects is complicated, also because the time scale of the photoemission process is comparable to that of the transport through the solid, so that intrinsic and extrinsic processes can interfere coherently.

Other spectral features which can be observed in a photoemission spectrum include plasmon losses and spin-orbit doublets. In the case of photoemission from a metal, the core-hole potential can be also screened by the collective oscillation of the electrons in the valence band, a so-called plasmon. The photoelectron can couple with these collective vibrations leading to characteristic, periodic satellites observed at lower kinetic energy with respect to the adiabatic peak by amounts that are multiples of the plasmon energy. The second spectral feature arises from the spin-orbit interaction, also known as *j-j* coupling, which is quite important for large *Z* elements. Indeed, the magnetic interaction between the spin of the electron and its angular momentum *l* might lead to a splitting of the degenerate state in two components having the total angular momentum quantum number $j = l \pm 1/2$. Obviously, this coupling can occur only if $l \neq 0$, that is, for electrons belonging to *p*, *d* or *f* orbitals. The photoemission intensities of

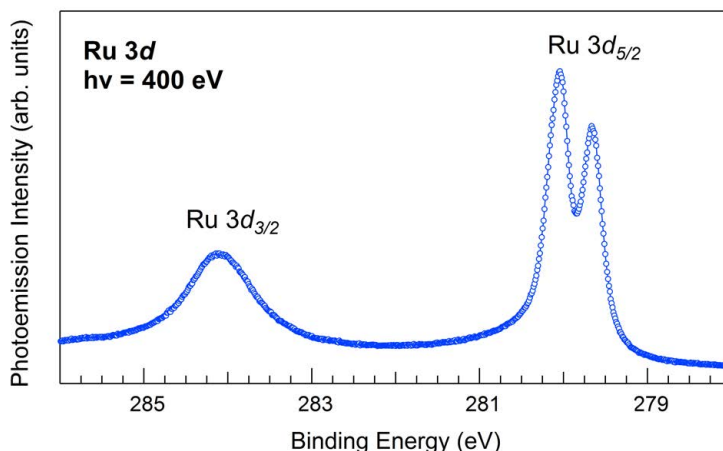


Figure 2.3: Spin-orbit splitted components of the Ru 3d core level. The double-peak structure of the $3d_{5/2}$ stems from the core level shifted components of surface and bulk atoms (see text for details).

the spin-orbitals are determined by the ratio between the corresponding degeneracies, $2j + 1$. Fig. 2.3 shows the $d_{3/2}$ and $d_{5/2}$ spin-orbit splitted component of the Ru 3d photoemission peak. Several spectral contributions can be distinguished in the Ru $3d_{5/2}$ peak; these are the core level shifted components stemming from surface, subsurface and bulk atoms which are explained in detail in Section 2.3.1.

2.2.1 Fermi Level Referencing

In a XPS experiment, the photoelectron escaping from the surface are detected with some kind of analyzer, which is meant to give an accurate measurement of the electron binding energy. This requires to fix a binding energy of reference. The vacuum level is the natural reference for free atoms, but in the case of solids the situation is more complicated. Indeed, the evaluation of the vacuum level in a solid requires the knowledge of the work functions and the contact potentials of the experimental system. Therefore, XPS spectra are usually referenced to the Fermi level.

Fig. 2.4 illustrates how the photoelectron kinetic energy can be easily measured by grounding both the sample and the electron energy analyzer. This aligns the corresponding Fermi levels, so that by simply measuring the photoelectron kinetic energy, it is sufficient to know $\phi_{analyzer}$ to calculate the E_b^F , and eq. 2.1 can be re-written as

$$E_b^F = h\nu - E_{kin}^{meas} - \phi_{analyzer}. \quad (2.9)$$

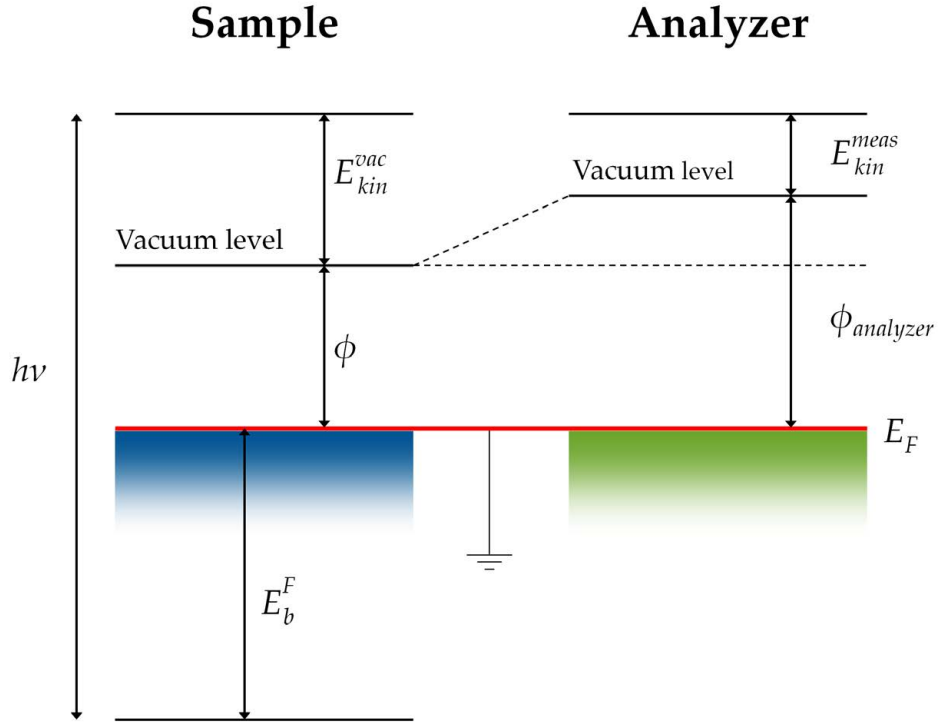


Figure 2.4: Energy level diagram in a typical XPS experiment.

2.2.2 The Photoemission Cross-section

The intensity of a photoemission peak is related to the photoemission cross-section σ , which is defined as the transition probability per unit time of exciting a system from an initial state Ψ^i to a final state Ψ^f by absorbing a photon with energy $h\nu$, divided by the photon flux. The transition rate is provided by the *Fermi golden rule*:

$$W_{fi} = \frac{2\pi}{\hbar} \left| \langle \Psi_f | \hat{H}_{int} | \Psi_i \rangle \right|^2 \delta(E_f - E_i - h\nu), \quad (2.10)$$

where \hat{H}_{int} is term of the non-relativistic Hamiltonian describing the photon-electron interaction.

The Hamiltonian operator of a spinless particle of charge q and mass m in presence of an electromagnetic field is given by:

$$\hat{H} = \frac{1}{2m} \left(\hat{\mathbf{p}} - q\hat{\mathbf{A}} \right)^2 + qV, \quad (2.11)$$

where the electromagnetic field is defined through the scalar and vector potential V and \mathbf{A} , respectively. Therefore, the time-dependent Schrödinger

equation is:

$$\begin{aligned} i\hbar \frac{\partial}{\partial t} \Psi(\mathbf{r}, t) &= \left[\frac{1}{2m} \left(\hat{\mathbf{p}} + \frac{e}{c} \hat{\mathbf{A}} \right)^2 + V + \hat{U} \right] \Psi(\mathbf{r}, t) \\ &= \hat{H} \Psi(\mathbf{r}, t). \end{aligned} \quad (2.12)$$

By using the Coulomb gauge, defined by $\nabla \cdot \mathbf{A} = 0$, and taking $V = 0$, the Schrödinger equation reduces to¹

$$i\hbar \frac{\partial}{\partial t} \Psi(\mathbf{r}, t) = \left[\frac{\hat{\mathbf{p}}^2}{2m} + \hat{U} - \frac{q}{m} \hat{\mathbf{A}} \cdot \hat{\mathbf{p}} \right] \Psi(\mathbf{r}, t), \quad (2.13)$$

in which the $\hat{\mathbf{A}}^2$ term has been neglected because much smaller than the linear term in $\hat{\mathbf{A}}$, and where we have used the fact that in the Coulomb gauge²

$$\begin{aligned} \nabla \cdot (\hat{\mathbf{A}} \Psi) &= \hat{\mathbf{A}} \cdot (\nabla \Psi) + (\nabla \cdot \hat{\mathbf{A}}) \Psi \\ &= \hat{\mathbf{A}} \cdot (\nabla \Psi). \end{aligned} \quad (2.14)$$

The Hamiltonian operator can be written as

$$\hat{H} = \hat{H}_0 + \hat{H}_{int} \quad (2.15)$$

where

$$\hat{H}_0 = \frac{\hat{\mathbf{p}}^2}{2m} + \hat{U}, \quad (2.16)$$

includes the kinetic term and the potential energy \hat{U} (which eventually takes into account the Coulomb interaction with the nucleus, the Coulomb repulsion between the electrons and the spin orbit interaction), while

$$\hat{H}_{int} = \frac{q}{m} \hat{\mathbf{A}} \cdot \hat{\mathbf{p}} \quad (2.17)$$

describes the electric field acting on the electron moments $\hat{\mathbf{p}}$.

The vector potential can be written as a plane electromagnetic wave with wave vector \mathbf{k} , frequency ν and unit vector ϵ ,

$$\mathbf{A} = \epsilon A_0 e^{i(\mathbf{k} \cdot \mathbf{r} - \omega t)}. \quad (2.18)$$

For practical interest we can neglect the spatial variation of the radiation field across the emitter atom, that is, the photon wavelength λ is much

¹A spatial variation of $\hat{\mathbf{A}}$ might occur, but this effect is small if the photon frequency ν exceeds the plasmon frequency, at least on the surface.

²This essentially corresponds to a one photon absorption process, and it is strictly valid only in the weak field case. For high photon density sources, such as lasers, it is no longer possible to neglect the quadratic term.

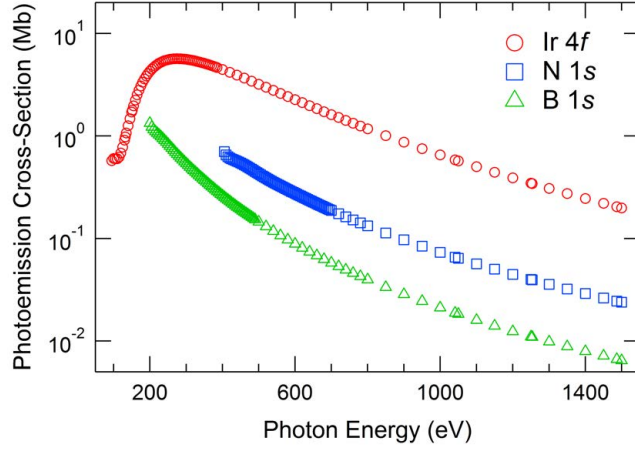


Figure 2.5: Photoemission cross-section for Ir $4f_{7/2}$, B $1s$ and N $1s$ core levels as a function of the energy of the incident photons.

longer than the typical interatomic distances³. This is usually known as *dipole approximation*. Consequently, the exponential can be approximated to

$$\exp(i\mathbf{k} \cdot \mathbf{r}) = 1 + (i\mathbf{k} \cdot \mathbf{r}) + \frac{1}{2!}(i\mathbf{k} \cdot \mathbf{r})^2 + \dots \approx 1. \quad (2.19)$$

With these approximations, after a series of mathematical steps, the absorption cross-section, which is proportional to the transition probability in eq. 2.10, becomes

$$\sigma_{fi} = \frac{4\pi^2 e^2}{3\hbar c} \omega |\langle \Psi_f | \hat{\mathbf{r}} | \Psi_i \rangle|^2. \quad (2.20)$$

As an example, fig. 2.5 shows the variation of the photoionization cross-section as a function of the incident photon energy for some of the characteristic energy levels that have been investigated in the experiments described in this thesis, namely, the Ir $4f_{7/2}$, B $1s$ and N $1s$ core levels. This figure highlights one of the great advantages offered by the use of synchrotron radiation sources, that is, the tunability of the photon energy. Indeed, this offers the possibility to maximize (or minimize) the sensitivity to the core level under investigation by simply selecting the proper photon energy, which allows to optimize the photoemission cross-section.

2.3 Core Level Shifts

Some of the spectral features arising from initial and final state effects in core level XPS have been already introduced in the previous section. This

³This condition certainly holds for photon energies below 1 keV.

section will describe a further spectral contribution which provides a detailed information about the chemical environment and constitutes one of the fundament of XPS technique, namely, the chemical shift. Chemical shifted components result from variations of the core level binding energy that depend on the chemical state of the emitter, like its oxidation state or chemical environment. For instance, the formation of chemical bonds with other atoms affects the initial state of the emitter and, therefore, the E_b of the electrons in that atom (initial state effect). Moreover, the modified charge distribution and density can even lead to a change of the relaxation energy terms appearing in eq. 2.8 (final state effect). As a result, the core level binding energy depends also on the chemical surroundings of the emitting atom. This allows to define the chemical shift as the difference in binding energy of a core level in two atoms of the same element within different chemical (electronic) environments.

The peculiar chemical sensitivity of photoemission spectroscopy was demonstrated by Sokolowski, Nordling and Siegbahn in the late 50's, thanks to the breakthrough of the high-energy resolution ESCA, which was developed by the same group [8]. Siegbahn and co-workers measured a shift of few eV between the C 1s core level in metallic copper and copper oxide [9]. The CLS was even more pronounced for the S 1s core level in sulfur compounds, where a double peaks was observed stemming from two chemically non-equivalent sulfur atoms within the same molecule [10].

By means of eq. 2.4 we can derive the Core Level Shift (CLS) between two different systems A and B as

$$\Delta E_b = E_A^f(N-1) - E_A^i(N) - E_B^f(N-1) + E_B^i(N) \quad (2.21)$$

This equation clearly shows that, in order to properly evaluate the CLS, both initial and final state contributions have to be taken into account.

2.3.1 Surface Core Level Shifts

A specific kind of chemical shift is the so-called *Surface Core Level Shift* (SCLS), which is related to the different structural surroundings of the outermost surface atoms with respect to the atoms in the bulk of a solid. The extent of SCLSs is usually smaller compared to that of CLS of other kinds, therefore High Resolution XPS (HR-XPS) measurements are usually required to detect these shifted components. SCLSs were first observed in the Au $4f_{7/2}$ core level of a polycrystalline gold surface [11]. Since that time, HR-XPS has been successfully employed to investigate the SCLSs of many others clean surfaces as well as adsorbate covered substrates [12–14].

A qualitative explanation of the main trend in SCLSs for transition metals can be derived within a simple initial state picture [15]. Fig. 2.6 depicts a schematic of the *d*-bands of a transition metal, showing the narrowing

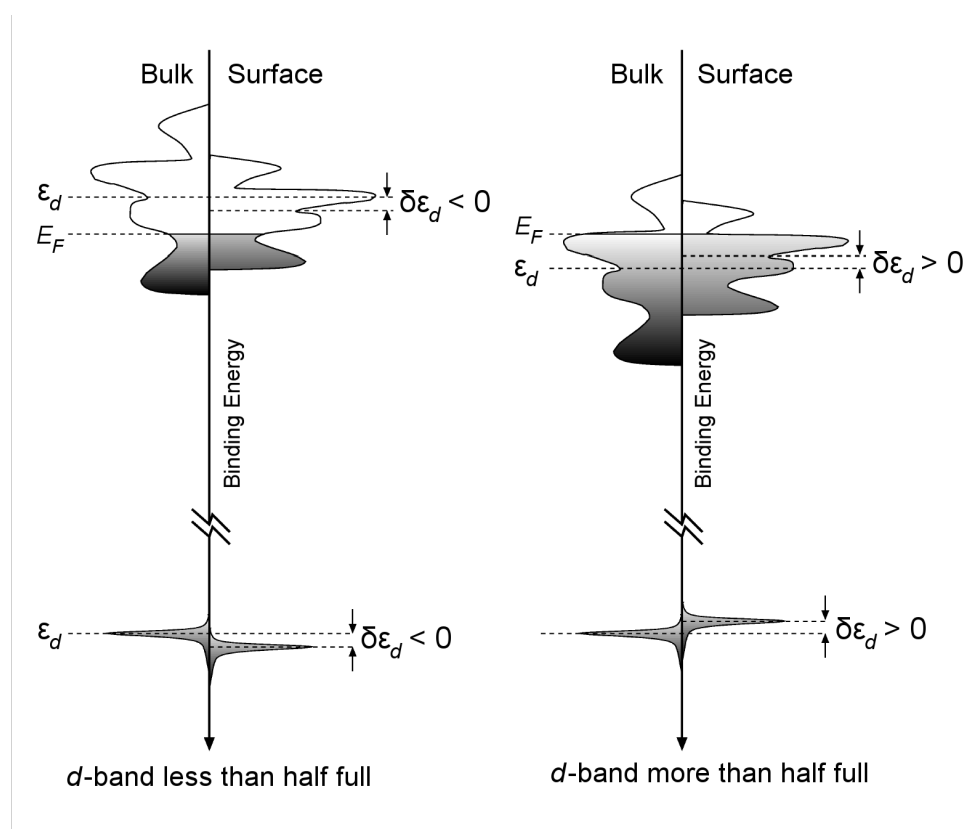


Figure 2.6: Schematic of the SCLS for transition metals. The reduced coordination of the surface atoms causes a narrowing of the valence d -band. To maintain charge neutrality, the center of the surface d -band moves towards higher (left) or lower (right) binding energy with respect to the bulk according to the occupancy of the d -band.

of the surface d -band due to the reduced degree of coordination of surface with respect to bulk atoms. In order to achieve charge neutrality and align the corresponding Fermi energies, electrons flow from the bulk to the surface, for a more than half filled band, or viceversa, if the band is less than half filled. The resulting electrostatic potential affects both the valence band and the deeper core levels of the surface atoms. This shift in energy changes according to the occupation of the band itself: the shift is towards higher (lower) binding energy for a band less (more) than half full.

Fig. 2.7 shows the experimental evidence of SCLS for the $3d_{5/2}$ core level from a clean Ru(0001) surface. The spectral deconvolution results in a bulk component (RuB), and two additional peaks stemming from the atoms in the first (RuS1) and second (RuS2) layers. Moreover, fig. 2.7 points out the high energy resolution needed to assess the SCLSs, which are usually of the order of hundreds of meV.

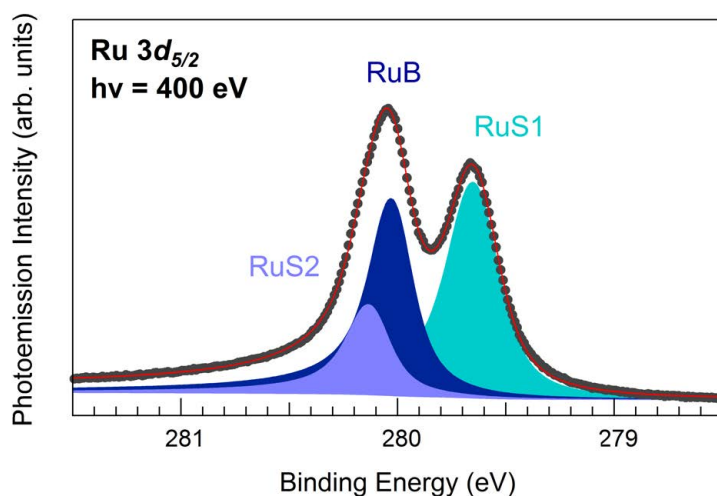


Figure 2.7: Ru $3d_{5/2}$ core level spectrum. A high-energy resolution is required in order to distinguish the fine structure due to the different surface core level shifted components.

2.3.2 Core Level Photoemission Line Shape

The capability to perform quantitative chemical analysis with XPS relies on the ability to correctly describe the photoemission spectrum with a theoretical model, that is, to perform a fit with a model curve calculated including the contributions of all chemically non-equivalent species (including their extrinsic and intrinsic losses) with proper line shapes.

Besides the instrumental contribution, the line shape of the photoemission peak is mainly determined by the core hole life-time and the vibrational broadening. First, one needs to consider the natural (intrinsic) linewidth due to the photoemission process itself, which is related to the finite core hole lifetime. The uncertainty in the energy of the core hole Γ is directly related to the core hole lifetime τ by the Heisenberg indetermination principle $\Gamma \geq \frac{\hbar}{\tau}$. For instance, $\tau \sim 10^{-15}$ s gives $\Gamma \sim 0.1$ eV. Once the hole has been created, the atom is in an excited state from which it can decay either by radiative or non-radiative process, namely, X-ray fluorescence and Auger emission, respectively. The higher is the decay probability of the core hole, the shorter is its lifetime, and the larger is the natural width of the corresponding peak. This broadening is described by a Lorentzian contribution

$$I_{Lor}(E_{kin}) = \frac{I_0}{\pi} \frac{\Gamma/2}{(E_{kin} - E_0)^2 + (\Gamma/2)^2}, \quad (2.22)$$

where Γ is the full width at half maximum (FWHM) and E_0 is the position of the adiabatic peak for the maximum intensity I_0 .

A further increase of the photoemission peak linewidth is given by the vibrational broadening. In molecules, the electronic transitions can be considered as occurring almost instantaneously on the time scale of the nuclear motion, meaning that the position and the momenta of the nuclei do not change during the photoemission process (Born-Oppenheimer or adiabatic approximation). This corresponds to a broadening of the photoemission peak due to a large range of energies of excited vibrational levels in the final state that can be reached from the ground state, with an intensity distribution governed by the Franck-Condon principle [5]. A similar effect occurs for lattice vibrations in solids, because of the electron-phonon coupling, which determines a line broadening that can be described by a Gaussian distribution [16].

Besides the contributions described above, which are intrinsic properties of the XPS line shape, the peak linewidth is affected also by experimental broadening. The latter includes the contribution of the finite experimental resolution of the monochromator and the electron energy analyzer. Finally, an inhomogeneous contribution, the so-called inhomogeneous broadening, can originate from the presence of unresolved chemical or structural shifted components in the spectrum. The vibrational, experimental and inhomogeneous broadening can be described by means of a Gaussian function:

$$I_{Gaus} = I_0 \exp\left(-\frac{(E_{kin} - E_0)^2}{2\sigma^2}\right), \quad (2.23)$$

where σ is the Full Width at Half Maximum (FWHM).

One of the most commonly used models for describing the line shape of photoemission peaks in metals is the Doniach-Šunjić function [17], which is the convolution between a δ distribution function

$$f(E) \propto \frac{1}{(E - E_0)^{1-\alpha}}, \quad (2.24)$$

which takes into account the inelastic tail due to excitation of electron-hole pairs at the Fermi level (see Section 2.2) through the asymmetry parameter α , and a Lorentzian contribution (eq. 2.22), thus

$$I_{DS}(E_{kin}) = I_0 \frac{\Gamma_E(1-\alpha)}{[(E_{kin} - E_0)^2 + (\Gamma/2)^2]^{(1-\alpha)/2}} \zeta(E_{kin}), \quad (2.25)$$

where

$$\zeta(E_{kin}) = \cos\left[\frac{\pi\alpha}{2} + (1-\alpha) \arctan\left(\frac{E_{kin} - E_0}{\Gamma/2}\right)\right], \quad (2.26)$$

and Γ_E is the gamma function

$$\Gamma_E(x) = \int_0^\infty t^{x-1} e^{-t} dt. \quad (2.27)$$

The analysis of all the photoemission spectra presented in this thesis was performed by using a Doniach-Šunjić function convoluted with a Gaussian, which takes into account the effects described above. In addition, a linear background was also included in the fit. The binding energies are referenced to the Fermi energy, which was measured together with the corresponding core level spectrum.

2.4 Structural Effects - Photoelectron Diffraction

After a photoelectron leaves the emitter, it might be elastically scattered by the surrounding atoms. The interference between the photoelectron primary wave, which propagates towards the electron analyzer along \mathbf{k} without suffering any scattering event, and the diffused waves, originating from the elastic scattering of the primary wave with the atoms close to the emitter, produces strong modulations of the photoemission intensity which depend on both the kinetic energy of the photoelectron and the propagation direction \mathbf{k} . This mechanism, which is schematically shown in fig. 2.8, is at the base of the X-ray Photoelectron Diffraction (XPD) technique, and can introduce intensity modulations as large as 70% of the overall photoemission signal. The modulation function is commonly defined as

$$\chi = \frac{I - I_0}{I_0}, \quad (2.28)$$

where I is the measured intensity whilst I_0 is the intensity of the primary wavefront.

The modulations contained in the XPD pattern provide a large amount of structural information about the local geometry around the emitting atom. This is primarily due to the rapid decrease of the photoelectron wave amplitude that allow to probe only emitter's coordination shell of nearest neighbours.⁴ Furthermore, the photoemission process guarantees another characteristic of the photoelectron diffraction, namely, its elemental sensitivity. XPD is thus a very effective tool to investigate the short-range order with chemical state specificity.

An important feature of XPD is the relation between the kinetic energy of the photoelectron and the scattering factor $f(\theta_j)$, where θ_j is the scattering angle, that is, the angle between the incident and scattered waves. The scattering factor $f(\theta_j)$ is defined as the ratio between the scattered (by the atom at \mathbf{r}_j) and incident wave amplitudes. The typical behaviour of $|f(\theta)|$ is shown in fig. 2.9.

⁴In a first approximation, the scattered wavefront is spherical, therefore its amplitude decreases as $\frac{1}{r}$.

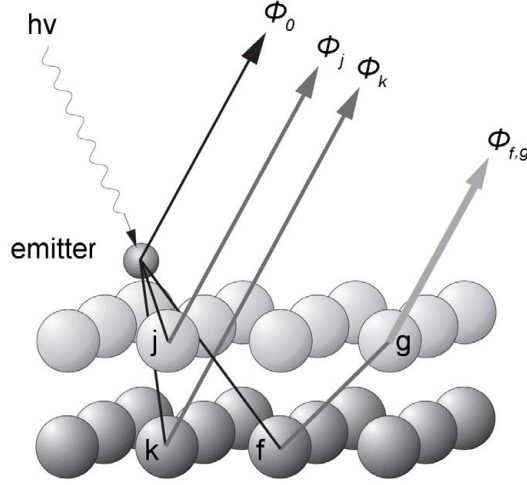


Figure 2.8: Schematic drawing of the processes involved in photoelectron diffraction process.

The simplest theoretical approach to describe the photoelectron diffraction process is to work within the single scattering approximation, so that

$$|\psi_f\rangle = \phi_0 + \sum_j \phi_j(\mathbf{r}_j \rightarrow \mathbf{k}) \quad (2.29)$$

where ϕ_0 is the emitted plane wave, while ϕ_j is the wave singly scattered at \mathbf{r}_j and emerging along the \mathbf{k} direction. The photoemission intensity can therefore be expressed as

$$I(\mathbf{k}) \propto \left| \hat{\mathbf{e}} \cdot \hat{\mathbf{k}} e^{-L/\Lambda_e} + \sum_j \frac{\hat{\mathbf{e}} \cdot \hat{\mathbf{r}}_j}{r_j} |f_j(\theta_j)| W_j e^{-L_j/\Lambda_e} e^{i[kr_j(1-\cos\theta_j) + \varphi_j(\theta_j)]} \right|^2 \quad (2.30)$$

The term $\hat{\mathbf{e}} \cdot \hat{\mathbf{k}}$ is associated with the directly emitted wave, whereas the sum is extended to all spherical waves that have been scattered by an atom located at \mathbf{r}_j with an amplitude given by $|f_j(\theta_j)|$. Inelastic scattering is taken into account by the exponential terms e^{-L/Λ_e} and e^{-L_j/Λ_e} , with L (L_j) being the total path length of the photoelectron. Vibrational effects, which can attenuate the interference patterns in XPD, are included through the Debye-Waller factor W_j . Finally, the phase shift of each spherical wave is determined by the scattering process, φ_j , and by the path difference $kr_j(1 - \cos\theta_j)$ between the incident and scattered waves.

From a practical point of view, eq. 2.30 states that the photoemission intensity depends both on the kinetic energy and the emission angles of

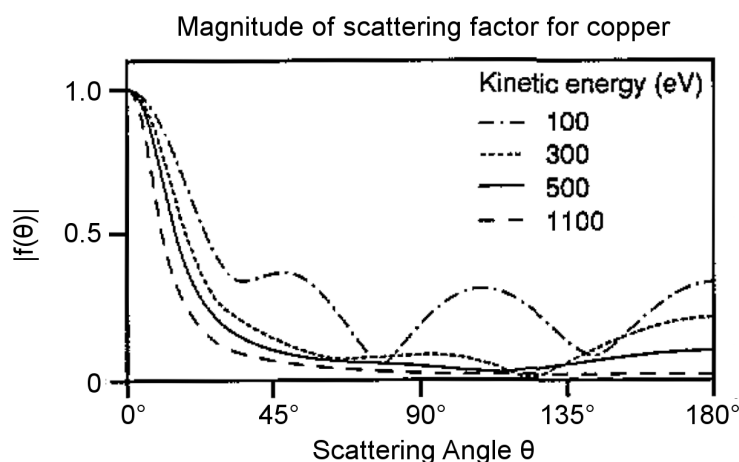


Figure 2.9: $f(\theta)$ of a copper atom as a function of the scattering angle and for different electron kinetic energies. Adapted from Ref. [18].

the electron. Therefore, XPD investigations can be performed in two different ways: by varying the azimuthal angle, the polar angle or both of them (angle-scanned XPD); or scanning the energy of the photoelectron by varying the energy of the photon source (energy-scanned XPD).

As can be seen from fig. 2.9, the scattering factor shows a maximum at $\theta = 0^\circ$, which becomes narrower with increasing kinetic energies. This is the so-called *forward scattering* effect, which becomes particularly intense when an atom is placed in line along the path between the emitter atom and the detector. It is noteworthy that in the forward focusing geometry, the intensity enhancement is not due to the rise of the scattering factor alone, but also to the vanishing phase shift, *i.e.*, there is no path length difference between the emitted and the scattered waves and the interference is constructive. As a consequence, the increase of the scattering angle introduces a path length difference which eventually leads to destructive interference. Thus, the forward scattering can be exploited for the determination of the interatomic directions in adsorbed molecules. This is clearly depicted in fig. 2.10, showing the forward scattering effect in the simple case of a CO molecule adsorbed on a surface. On the other hand, if the electron energy is sufficiently low, then also *backward scattering* at $\theta = 180^\circ$ becomes important. This peak is associated with photoelectrons that are elastically scattered by atoms behind the emitter.

A more accurate description of the diffraction process can be done by including multiple scattering effects. The advancement in computers performance allows the elaboration of complex theoretical models resulting in more and more realistic simulations of the diffraction patterns. In this regard, one of the most popular methods to perform multiple scattering

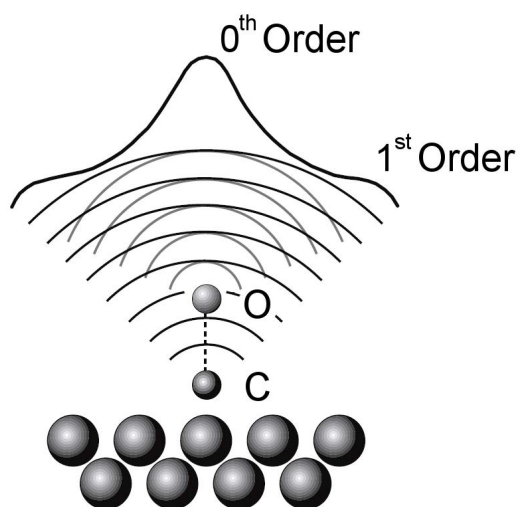


Figure 2.10: CO molecule adsorbed on a surface, in the on-top adsorption site. Interference pattern and diffraction orders originated by spherical waves from the C emitter and the O scatterer. At large polar angles the interference can be either constructive or destructive, depending on the phase shift variation induced by the length difference.

calculation is based on the separable representation of the Green's function matrix, first developed by Rehr and Albers [19]. As a result, reliable theoretical calculations can be performed, which can be compared to the measured interference patterns to extract a very detailed quantitative information on the short-range structure around the emitting atom. This approach has been successfully exploited to gain structural information on the *h*-BN/Ir(111) interface presented in Chapter 3. Theoretical simulations of the N $1s$, B $1s$ and Ir $4f_{7/2}$ diffraction patterns have been performed using the Electron Diffraction in Atomic Cluster (EDAC) package [20]. The working principle of this code is based on the implementation of an atomic cluster and the use of multiple scattering theory to model the XPD pattern at a specific electron kinetic energy.⁵ In a second step, the simulated patterns have been compared to the experimental XPD data in a qualitative trial-and-error procedure.

2.5 Absorption Spectroscopy

The range application of X-rays in surface science has been largely extended by the development of synchrotron radiation sources. Indeed, in

⁵For further details on the EDAC code the reader is referred to the reference manual which is available online at <http://nanophotonics.csic.es/static/widgets/edac/manual/edac.html>.

addition to techniques that have received great benefits from the use of synchrotron radiation, such as the previously discussed XPS and XPD, new experimental approaches have been developed which are based explicitly on the tunability of X-rays synchrotron radiation. The latter include the X-ray Absorption Spectroscopy (XAS).

In a XAS experiment the radiation absorbed by the sample is measured as a function of the photon energy. According to eq. 2.4, when the energy of the photon equals that of the core level, a strong enhancement of the absorption is measured due to the promotion of the electron to an unoccupied state in the conduction band or to a continuum state. Generally, the absorption spectrum is characterized by several peaks, corresponding to different excitations from the levels with quantum numbers $n = 1, 2, 3, \dots$ which are defined as K, L, M, \dots absorption thresholds, respectively. It is worth noting that the K threshold consists of a single edge, because it corresponds to excitation of $1s$ electrons, while higher absorption thresholds are a collection of edges. For instance, the L -edge ($n = 2$) is associated to excitations from $2s, 2p_{1/2}$ and $2p_{3/2}$ level resulting in L_1, L_2 and L_3 edges.

A typical XAS spectrum is shown in fig. 2.11. Two kinds of structures overlap in the absorption spectrum. The first of these, centered close to the absorption threshold, is called Near Edge Absorption Fine Structure (NEXAFS) or X-ray Absorption Fine Structure (XANES). In this region, extending up to about 50 eV beyond the threshold, the photoelectron backscattering amplitude is large so that multiple scattering events are dominant. For this reason, NEXAFS is very sensitive to the the coordination environment of the emitter atom. The second feature appearing in the spectrum in fig. 2.11 is the Extended X-ray Absorption Fine Structure (EXAFS), which extends from about 50 eV above the absorption threshold for hundreds of eV. In this case single scattering is predominant, therefore the amplitude modulation of the spherical wave gives access to important information on the interatomic distances. Further details on NEXAFS technique, which has been employed in the characterization of the bonding geometry of the borazine ($B_3N_3H_6$) molecule on Ir(111) presented in Chapter 3, are given in the following.

NEXAFS technique has been developed in the 80's to investigate the bonding and the structure of (mostly) organic molecules adsorbed on surfaces [22]. The NEXAFS spectrum of a molecule is dominated by intramolecular excitations, the so-called resonances, *i.e.*, electron transitions from the K shell to the bound states close to the vacuum level, but below the ionization energy of the molecule. Fig. 2.12 displays a typical K -edge absorption spectra, together with the energetic levels involved in this transition, for a simple (A,B) diatomic molecule. If the initial state is a $1s$ core level, the selection rules impose the final state to be a molecular orbital with a p atomic component, therefore an orbital of π or σ symmetry. A fundamental feature of molecular bonds is related to their strong directional

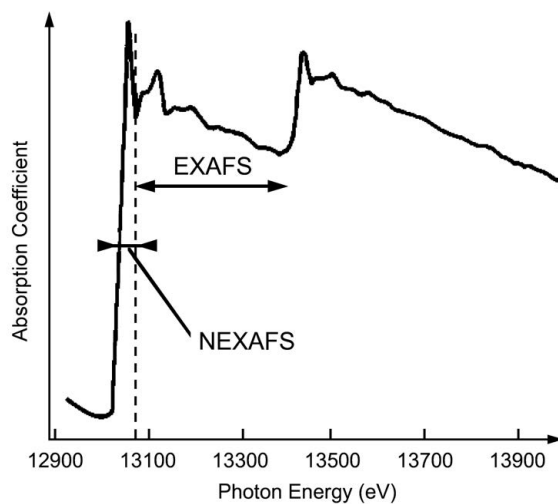


Figure 2.11: Schematic of a typical absorption spectrum. Specifically, this corresponds to the K -edge absorption spectrum for $\text{BaPb}_{1-x}\text{Bi}_x\text{O}_3$. Adapted from Ref. [21].

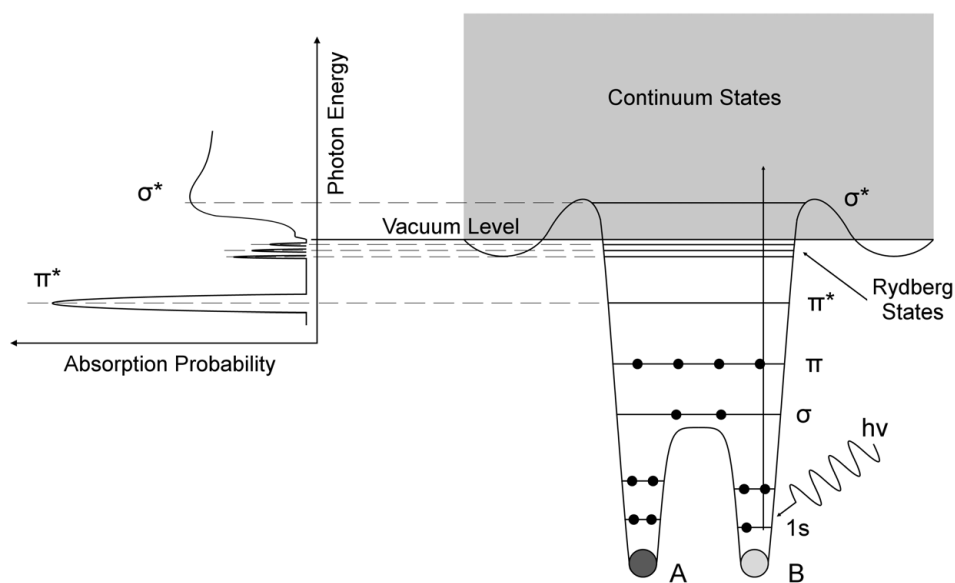


Figure 2.12: Schematic of the K -edge absorption spectrum (left) and potential (right) for a diatomic (A,B) molecule. π^* and σ^* resonances arise from the excitation of atomic $1s$ core level electrons to empty molecular orbital. The other resonances are due to transitions to Rydberg final states. Adapted from Ref. [22].

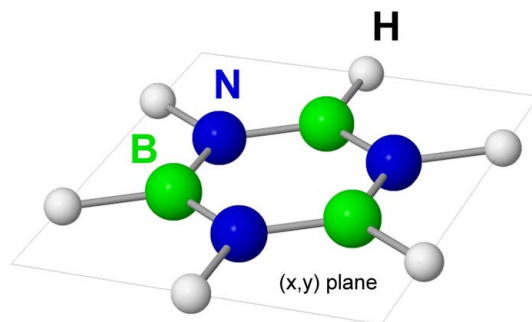


Figure 2.13: Sketch of the borazine molecule. The molecule ring is oriented parallel to the (x, y) plane.

character, so that there is a unique correlation between the spatial orbital orientation and the molecular geometry. In the K -edge absorption spectra of molecules with a well-defined orientation with respect to the polarization of the incident light, this property is reflected in a drastic polarization dependence of the π^* and σ^* resonance intensities, which can be qualitatively explained within the framework outlined in Ref. [22]. This peculiar characteristic of NEXAFS technique has been exploited to investigate the orientation of $B_3N_3H_6$ molecules adsorbed on the Ir surface, as illustrated in Section 3.3.1. In the electric dipole approximation, the intensity of the transition $I_{f,i}$ is given by eq. 2.20

$$I_{f,i} \propto |\langle \Psi_f | \epsilon \cdot \nabla | \Psi_i \rangle|^2, \quad (2.31)$$

where the radiation is linearly polarized along the direction ϵ . The initial state $|\Psi_i\rangle$ is spherically symmetric and corresponds to a $1s$ core level. The final state $|\Psi_f\rangle$, instead, can be represented as a linear combination of atomic orbitals (LCAO) of the excited atom.⁶ For elements belonging to the second period, such as boron and nitrogen which are the subject of interest in the case of borazine, the final state wave function can be thus written as a linear combination of $2s$ and $2p$ states on the excited atoms:

$$\begin{aligned} |\Psi_f\rangle &= a |2s\rangle + b |2p_x\rangle + c |2p_y\rangle + d |2p_z\rangle \\ &= aR_{2s}(r) + R_{2p}(r) (b \sin \theta \cos \phi + c \sin \theta \sin \phi + d \cos \theta), \end{aligned} \quad (2.32)$$

where $R_{2s}(r)$ and $R_{2p}(r)$ are the radial part of the atomic wave functions. Eq. 2.32 states that the amplitude of the final state is maximized along the direction Ω defined by the p orbitals ($\Omega = b\mathbf{e}_x + c\mathbf{e}_y + d\mathbf{e}_z$). Therefore, eq. 2.31 reduces to

$$I_{f,i} \propto |\langle \Psi_f | \epsilon \cdot \nabla | \Psi_i \rangle|^2 \propto |\epsilon \cdot \Omega|^2 \propto \cos^2 \delta \quad (2.33)$$

⁶These are the main components because the strong localization of the initial state dominates in the evaluation of the matrix element.

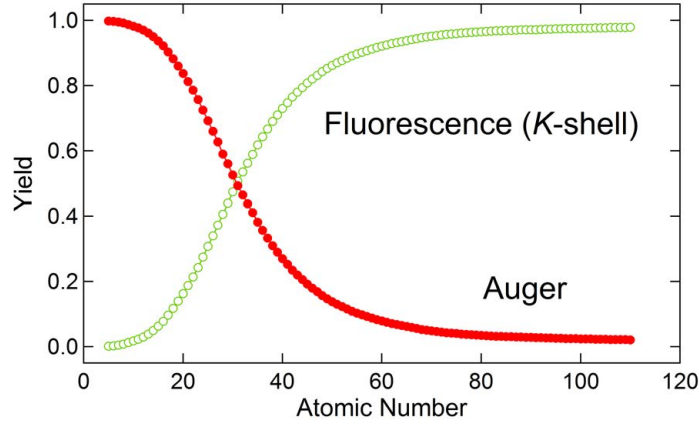


Figure 2.14: Fluorescence and Auger yields as a function of the atomic number. The data are based on the values listed in Table 4 and 5 of Ref. [23].

where δ is the angle between ϵ and Ω . Eq. 2.33 shows that the maximum of the intensity is along the direction given by the p component of the final state Ψ_f .

For instance, the borazine molecule is characterized by σ bonds in the molecular plane and, perpendicular to this, π bonds. Referring to fig. 2.13, if the molecule is oriented parallel to the (x, y) , the direction of the σ^* orbitals is given by the e_x and e_y unit vectors, while that of the π^* orbitals coincides with e_z . Therefore, the intensity of π^* and σ^* resonances of boron and nitrogen is given by

$$\begin{aligned}
 I_{1s \rightarrow \sigma^*} &\propto |\epsilon \cdot e_x|^2 + |\epsilon \cdot e_y|^2 \\
 &\propto \sin^2 \theta \cos^2 \phi + \sin^2 \theta \sin^2 \phi \propto \sin^2 \theta \\
 I_{1s \rightarrow \pi^*} &\propto |\epsilon \cdot e_z|^2 \\
 &\propto \cos^2 \theta
 \end{aligned} \tag{2.34}$$

From eq. 2.34 it is clear that the polarization dependence of π^* and σ^* resonances is opposite. When the electromagnetic field is in the (x, y) plane, the σ^* intensity is maximum, while $1s \rightarrow \pi^*$ transitions are inhibited. Viceversa, when the electromagnetic field is perpendicular to the (x, y) plane, only π^* resonances are measured.

The question arises as to how we could measure the NEXAFS signal. Since we want to probe the core excitation event, the detection of the photoemitted electrons is certainly not a good solution. Indeed, with this kind of measurement all the information contained in the bound state excitations below the ionization potential would be lost, as it can be immediately deduced from inspection of fig. 2.12. The right approach, instead, relies on the decay of the core-hole created by the X-ray absorption, that is, the

measurement of the de-excitation channels. As previously discussed, the de-excitation of the core-hole can be either radiative, by fluorescent emission, or non-radiative, by Auger emission. It has to be pointed out that both the fluorescent X-ray and the Auger peak are characteristic of the element, so that NEXAFS technique shows chemical sensitivity. Fig. 2.14 shows that the Auger decay is more probable for low Z elements, like boron and nitrogen. For this reason, the K -edge NEXAFS presented in Chapter 3 have been acquired by measuring the characteristic Auger peaks for boron and nitrogen (KLL emission at 177 and 380 eV, respectively), selecting an appropriate energy window with the electron analyzer. As the photon energy is scanned from below to above the absorption edge, an Auger electron is produced resulting from the filling of the core-hole. The Auger yield is thus proportional to the number of core-holes created and, therefore, to the X-ray absorption cross-section.

2.6 Experimental Setup

The development of synchrotron radiation sources have revolutionized the application of X-rays and UV radiation in surface studies. One of the major benefits arising from the use of synchrotron radiation with respect to conventional anode-based sources is the *energy tunability*. Indeed, conventional sources provide photons only at the fixed energies determined by the material of the anode, $h\nu = 1253.6$ eV for Mg and $h\nu = 1486.6$ eV for Al. The other great advantage offered by synchrotron light is the high *brilliance*, which is defined as the photon flux per unit solid angle and unit area at a given frequency.

Synchrotron radiation is produced by bunches of relativistic electrons orbiting in a storage ring. According to the theory first developed by Pomeranchuk in 1944 [24], and later on by Schwinger [25], when observed from the laboratory frame, a charge accelerated along an orbit emits radiation mainly in a characteristic narrow angular cone in a direction tangential to the electron orbit, as depicted in fig. 2.15.

In a synchrotron facility, the electrons are forced to follow a curvilinear trajectory by the application of a magnetic field of a device. In this regard, *bending magnets* have been the first and most simple devices used to keep the electrons travelling on a circular orbit. The bending magnet produces a broad band energy spectrum, ranging from the infrared to the hard X-ray region. Compared to bending magnets, *undulators* are much more brilliant radiation sources. The undulators, together with the *wigglers*, are periodic arrays of magnets which are placed along the straight sections of the storage ring. This is why they are also known as *insertion devices*. The undulator energy spectrum is not continuous as that of a bending magnet, but is characterized by peaks at well defined wavelengths, depending on the energy

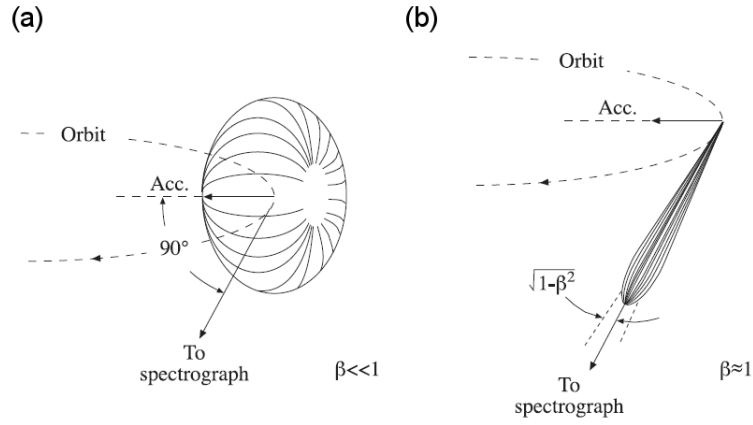


Figure 2.15: Radiation pattern for a) a slow electron and b) a relativistic electron moving in a circular path.

of the electrons, the period of the magnetic array (λ_u) and the magnetic field B . On the plane of the orbit, the wavelength is given by

$$\lambda = \frac{\lambda_u}{2\gamma^2} \left(1 + \frac{K^2}{2} \right), \quad (2.35)$$

where γ is the relativistic factor $(1 - \beta^2)^{-1/2}$ and K is the deflection parameter defined as

$$K = \frac{e}{2\pi m c} \lambda_u B. \quad (2.36)$$

Eq. 2.35 defines the fundamental frequency of the undulator, however, also the higher harmonics λ/n are produced, but only odd harmonics are emitted on the undulator axis. It is clear that in order to vary the photon wavelength, one has to change the magnetic field of the insertion device. As the undulators are usually made up by permanent magnets, the simplest way to change B , and therefore K , is to vary the vertical distance between the magnets, also known as the undulator gap. Typical values of K ranges from 1 to 5. At higher values the device is called wiggler: the deflection of the electrons is stronger and the energy spectrum resembles that of a bending magnet, although with higher brilliance and flux.

All the experiments presented in this thesis have been performed at the SuperESCA beamline of the Elettra-Sincrotrone storage ring in Trieste (Italy). Elettra is a third-generation synchrotron facility, which can operate at two different electron energies: 2.0 GeV and ~ 300 mA, which is particularly suitable for enhanced UV photoemission and spectroscopic applications, and 2.4 GeV and ~ 140 mA, especially suitable for X-ray emission and diffraction applications. Until December 2010, the insertion device of the SuperESCA beamline was a 56 mm-period undulator, formed by three sections with 81 periods each, covering a photon energy range of 85-1200

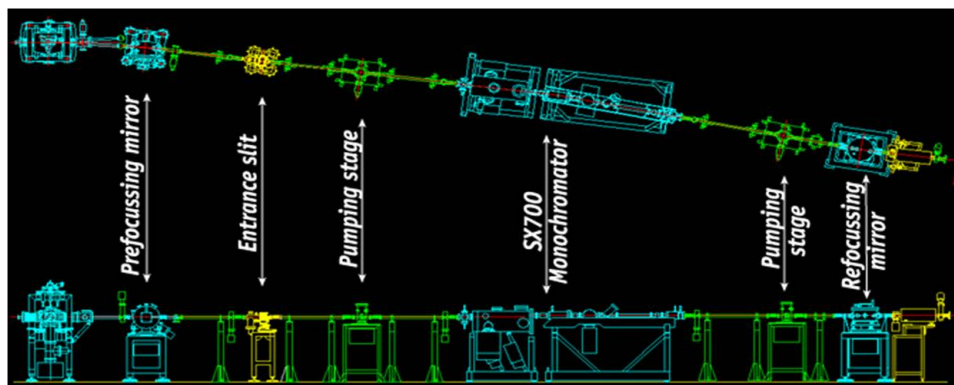


Figure 2.16: Schematic of the SuperESCA beamline at Elettra.

eV at 2.0 GeV ring energy, and 120-2000 eV at 2.4 GeV. A new undulator was installed afterwards. The characterization of the new insertion device and the re-alignment of the optical elements of the beamline have been also part of my PhD activity, and will be described in detail in Section 2.6.2.

2.6.1 The SuperESCA Beamline at Elettra

Photoelectron spectroscopy, and all the techniques based on the photoemission process, need to be performed in an ultra-high vacuum (UHV) environment. This requirement is first related to the IMFP of the electrons in the residual gas pressure, which should be large enough to allow them to reach the detector. Indeed, a high pressure results in an increased probability of inelastic scattering, leading to a marked attenuation of the electron signal. Furthermore, UHV is also required to keep clean the surface of the sample, preventing its degradation due to the adsorption of contaminants. The effect of the contaminants on the sample surface is given by the Hertz-Knudsen formula $\Phi = \frac{P}{\sqrt{2mk_B T}}$, where P is the gas pressure, m is the molecular mass, k_B is the Boltzmann constant and T is the sample temperature. If the molecule sticking probability is 1, at a partial pressure of $\sim 10^{-6}$ mbar, the surface would be covered in just few seconds. This is the reason why the background pressure should be kept in the range of $\sim 10^{-10}$, or even below.

SuperESCA, the first beamline operating at Elettra since 1993, is optimized for photoelectron spectroscopy measurements with soft X-rays. The radiation source is a two-sections 46 mm-period undulator with 98 periods, as best described in Section 2.6.2. A schematic of the key components of the SuperESCA beamline is shown in fig. 2.16. The light beam produced by the undulator is first pre-focused in the sagittal plane into the entrance slit, then monochromatized and, eventually, re-focused by an ellipsoidal mirror into the center of the experimental chamber.

The experimental station of SuperESCA consists of two UHV chambers separated by a gate valve, as depicted in fig. 2.17. The measurements are performed in the lower chamber, while the upper one is designed for sample preparation. The stainless steel top chamber is equipped with a sputter gun for sample cleaning, a plasma source and several feedthroughs for evaporators. It is also connected with a fast entry lock that allows to change the sample without breaking the UHV conditions, and with the gas line. Two different manipulators are available. The first is a modified CTPO manipulator with 5 degrees of freedom: 3 translational (x, y, z) and 2 rotational (θ, ϕ) axis. This manipulator is equipped with a liquid N₂ cryostat and an electron bombardment heating system which allows a sample temperature in the 120-1500 K range. Thanks to its fully motorized rotational movements, this manipulator is specifically designed for XPD investigations where the photoemission intensity is measured as a function of the emission angle, such as those presented in Section 3.3.3. The other manipulator is a liquid He cryostat with 4 degrees of freedom (x, y, z, θ) and an allowed sample temperature in the range of 20-1500 K. This manipulator allows to perform photoemission experiments where very low temperatures are needed. For instance, this manipulator was used for the investigation of the molecular adsorption of borazine presented in Section 3.3.1.

The manipulators allow to move the sample from the preparation to the experimental chamber. The latter is entirely made of μ -metal, a particular Ni-Fe alloy that shields the chamber from external magnetic fields, such as the Earth magnetic field, which could deflect the electrons trajectory. The experimental chamber is equipped with a Low Energy Electron Diffraction (LEED) apparatus, a monochromatized electron gun, a mass spectrometer and a gas inlet system.

The electrons photoemitted from the sample are collected with a system of 9 electrostatic lenses and brought to a PHOIBOS hemispherical analyzer from SPECS GmbH (150 mm mean radius), which is equipped with a delay line home-made detector. The latter is the key component of the SuperESCA beamline since it is specifically designed to allow fast XPS acquisition which, combined with the available high photon flux, give access to the dynamic evolution of the chemical processes occurring at surfaces. The next section is dedicated to a brief description of the principle of operation of the electron energy analyzer and the detector.

Instrumentation: Electron Energy Analyzer and Detector

As depicted in fig. 2.18, the hemispherical electron energy analyzer is made up by two concentric hemispheres electrodes of different radii among which a potential difference is applied. By means of this particular geometry, the photoelectrons are linearly dispersed according to their kinetic energy along the orbit from the entrance to the exit slit and, if they retain the same energy, first-order focused on the exit slit.

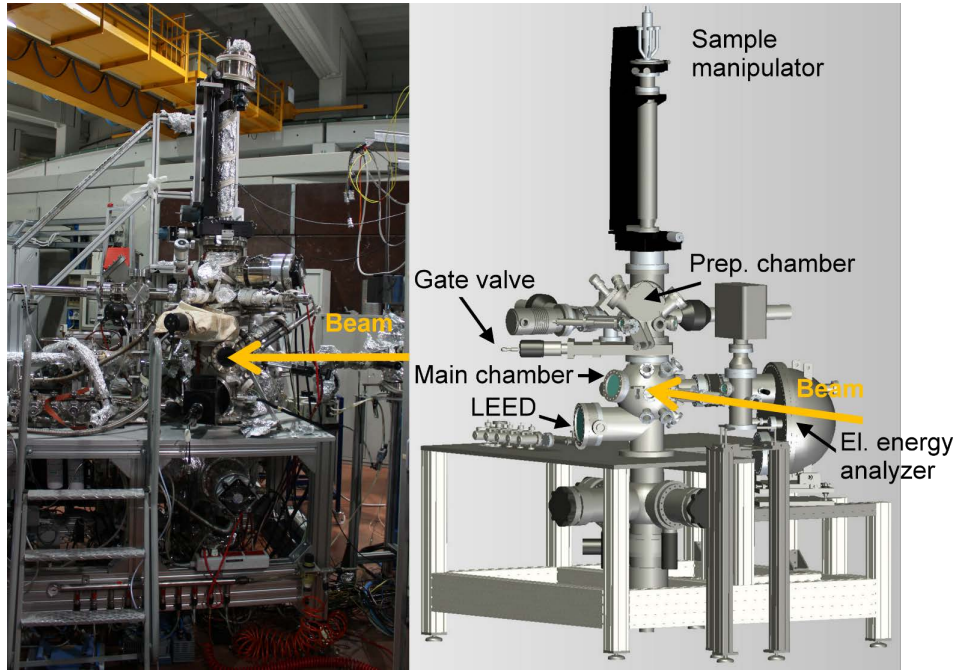


Figure 2.17: The experimental station at the SuperESCA beamline.

By applying the potentials V_1 and V_2 to the inner and outer hemispheres, respectively, the potential between the electrodes is given by

$$V(r) = -\frac{V_2 - V_1}{R_2 - R_1} \frac{R_1 R_2}{r} + const. \quad (2.37)$$

In order for the photoelectrons with kinetic energy E_0 to reach the exit slit travelling on the circular path defined by the radius $R_0 = (R_1 + R_2)/2$, the following relation has to be satisfied:

$$V_2 - V_1 = V_0 \left(\frac{R_2}{R_1} - \frac{R_1}{R_2} \right). \quad (2.38)$$

Eq. 2.38 determines the potentials that have to be applied in order to select electrons with kinetic energy E_0 , also known as *pass energy*, where $E_0 = eV_0$.

Taking into account the eventual divergence of the electron beam, represented by an angular offset α with respect to the direction normal to the entrance slit plane, the total energy resolution is given by

$$\Delta E = E_0 \left(\frac{w_{en} + w_{ex}}{4R_0} + \frac{\alpha^2}{4} \right), \quad (2.39)$$

where w_{en} and w_{ex} are the respective widths of the entrance and exit slits. From eq. 2.39, it is clear that the energy resolution can be improved either by increasing R_0 or by decreasing E_0 . The first option is, obviously,

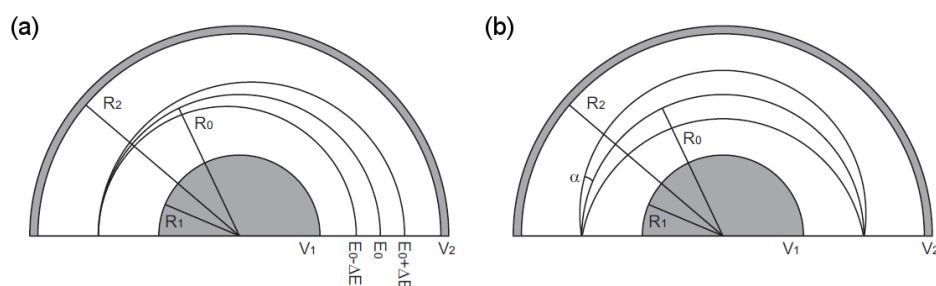


Figure 2.18: Energy dispersion properties (a) and focusing properties (b) of a hemispherical analyzer.

‘technically’ limited by the overall maximum dimensions of the analyzer. On the other hand, the electron transmission is damped at low values of E_0 . Therefore, a compromise between a high energy resolution and good signal-to-noise ratio has to be made. In order to measure a photoemission spectrum with a constant resolution throughout the whole energy range, the entire photoemission spectrum is recorded at a fixed value of the pass energy. This is possible thanks to the system of electrostatic lenses placed before the entrance slit which absolves a double function: (i) to collect the electrons from a solid angle as large as possible and focalize them into the entrance slit; (ii) to decelerate the electrons to the required kinetic energy E_0 .

The photoelectron detector, placed at the exit slit of the analyzer, has been developed at the Elettra-Sincrotrone Trieste. The first stage of the detection consists of an electron multiplier – formed by two microchannel plates (MCPs) in chevron configuration – that amplifies the charge of the impinging electrons, and transmits it to the proper system of acquisition. The latter is a home-made delay line detector [26], as shown in fig. 2.19. The electron cloud coming from the MCP stage impinges the delay line and generates two signals that travel in opposite directions towards the two ends of the delay line. The outputs are amplified, discriminated and then processed by a time to digital converter, which measures the delay time between the two signals and converts it to a spatial information on the position of the incident electron cloud, giving access to the energetic distribution along the analyzer dispersive direction.

The analyzer can work in two configurations: *scanning (sweep)* mode or *fixed (snapshot)* mode. In the scanning mode, for a given energy range, the voltage applied to the electrostatic lenses is swept, with E_0 kept fixed, so that each channel counts electrons with the selected kinetic energy for an interval equal to the selected time window. The acquisition time can be drastically reduced working in fixed mode. This procedure exploits the relation between the energy of the electron and its position on the detector

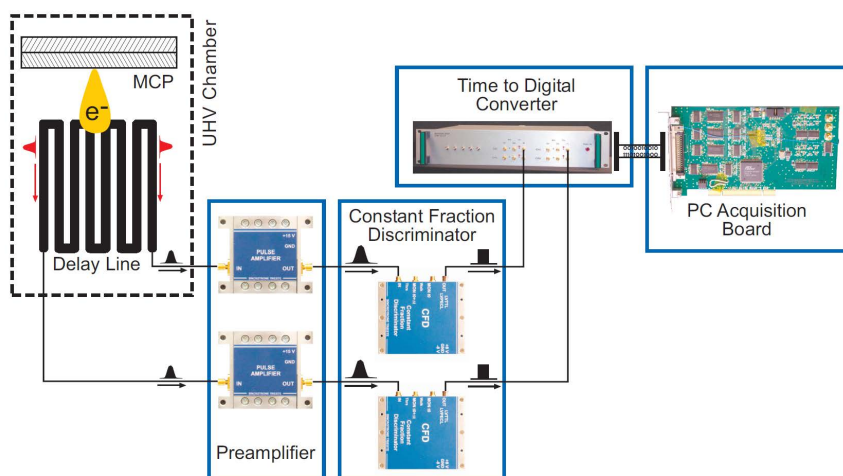


Figure 2.19: Encoding scheme of the delay line detector. The time delay between the two signals originated by the delay line are converted in a spatial position of the impinging electron beam, and so in the energetic distribution inside the single energy channel.

(see fig. 2.18a). If the energy range covered by the detector is wide enough and if the number of available channels is sufficiently high to clearly discriminate the photoemission features, it is possible to acquire a detector image and obtain the photoemission spectrum in one single shot.

It is important to highlight that to speed up the acquisition time allows not only monitoring in real-time chemical reactions occurring at surfaces, such as the Si intercalation process below graphene and the subsequent silicide formation presented in Section 5.3, but also to prevent sample contamination due to residual gas during time-consuming measurements that require the acquisition of thousands spectra, as in the case of the XPD investigations of the *h*-BN/Ir(111) interface (Section 3.3.3) and the N-doped graphene layer (Section 6.3).

2.6.2 Commissioning of the New Insertion Device

The optical layout of the SuperESCA beamline is shown in fig. 2.16. The new radiation source is a 46 mm-period undulator with 98 periods installed on a straight section of the Elettra storage ring. The undulator is composed by two equal modules and is capable to produce horizontally polarized light only. By setting the gap value from a minimum of 13.5 mm up to 40 mm the photon energy can be varied in the range 90-1800 eV working with 1st, 3rd and 5th harmonics. The monochromator is a modified version of the standard SX700 monochromator working in stigmatic configuration. Inside the monochromator the light is directed towards the plane grating

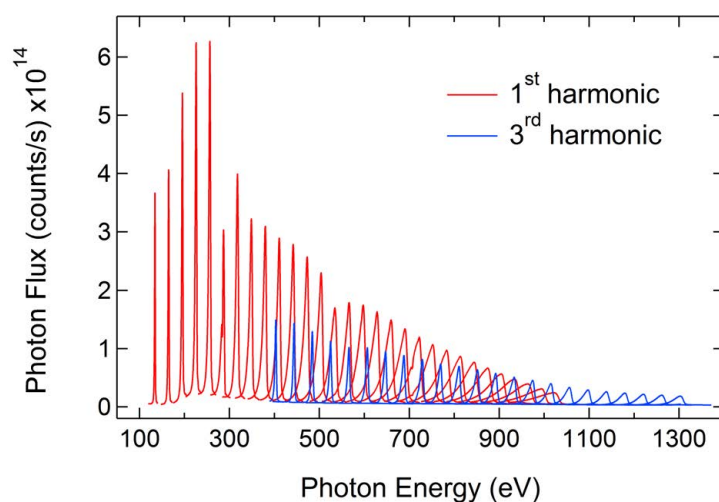


Figure 2.20: Undulator energy spectrum measured at the SuperESCA beamline.

by a plane mirror with variable angle of incidence. The diffracted beam is then focused at the exit slit, which defines the vertical size of the spot on the sample. A tapering of ~ 1 mm allows a controlled broadening of the spectrum of the harmonics. The possibility to taper the undulator gap, that is, to introduce a linear gap gradient along the length of the undulator, is of particular importance for NEXAFS measurements where the quick scan of the photon energy is required. In order to do this, the ideal approach would be to tune the undulator gap and synchronize the movement of the monochromator. However, this approach can pose technical problems for the mechanical motion of the undulator gap and the electron beam stability in the ring. The alternative method is to broaden the undulator harmonic by introducing a taper: in this way is possible to get a broader spectrum at a particular photon energy, but at the cost of peak flux.

Undulator spectra. As explained above, the undulator spectrum is not continuous, but peaked at well defined wavelengths defined by the value of the undulator gap. This is clearly illustrated in fig. 2.20, showing the undulator spectrum measured (at different gap values) by means of a photodiode placed after the exit slit. The latter has been set to $10 \mu\text{m}$, meaning that the bandwidth varies with the photon energy, while the aperture of the double slit was fixed to $1 \times 1 \text{ mm}^2$.

The photon flux at the sample, normalized at 100 mA ring current, is shown in fig. 2.21. The maximum flux is about 2×10^{12} ph/s/100 mA at 130 eV, while it progressively decreases at higher photon energies. The minimum located at ~ 300 eV is close to the C K -edge threshold and, indeed, is caused by a carbon contamination of the mirrors surfaces.

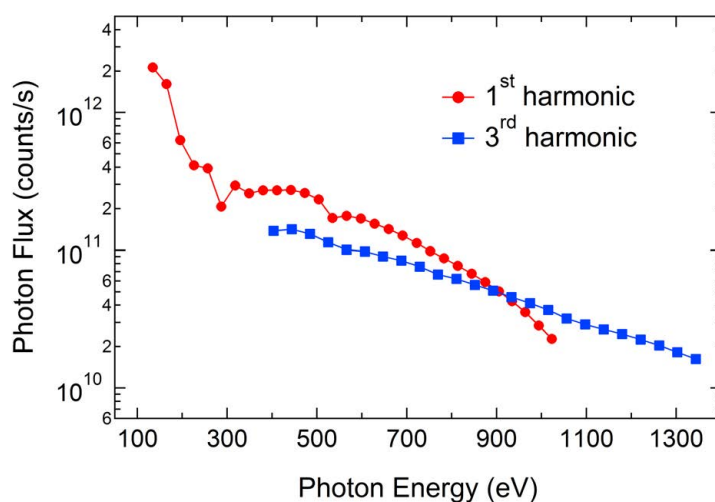


Figure 2.21: Experimental photon flux measured with the ring operating at 2.4 GeV.

Fig. 2.22 shows the improvements achieved by the new insertion device in terms of photon flux. With the storage ring operating at 2.0 GeV, the actual photon flux is about 2-3 times the older one up to 700 eV, and further increases at higher photon energies (solid red curve). These findings are even better than those expected from the simulations (dashed curve), since the latter obviously do not account for the re-alignment of the optical axes along the beamline, which, in turn, results in a maximization of the photon flux. A closer inspection to the experimental ratio curve in fig. 2.22 reveals two little bumps at about 300 and 600 eV photon energy. The drop at 300 eV is related to the aforementioned carbon contamination of the optical elements. The second bump, instead, is due to a flux lowering of the previous device in this energy range which corresponds to the switch from the 1st to 3rd harmonic. The gain is more regular with the ring operating at 2.4 GeV, the flux being approximately 3 times the older one. The broad peak at 800 eV corresponds to the shift from the 1st to the 3rd harmonic of the old undulator.

It is important to stress that the increased photon flux is of fundamental importance for the XPD measurements, where the flux gain at high photon energy allows to perform diffraction experiments working in forward scattering regime, thus giving a direct insight into the surface symmetry and bond orientations (see Section 2.4). Moreover, with a higher photon flux is possible to overcome the transmission damping experienced at low pass energy values and, eventually, to increase the energy resolution and the signal-to-noise ratio in the XPS spectra (see Section 2.6.1). This is an essential requirement to determine the CLSs of 4*d* and 5*d* transition metals which shows relatively small variations of the core-level binding energy

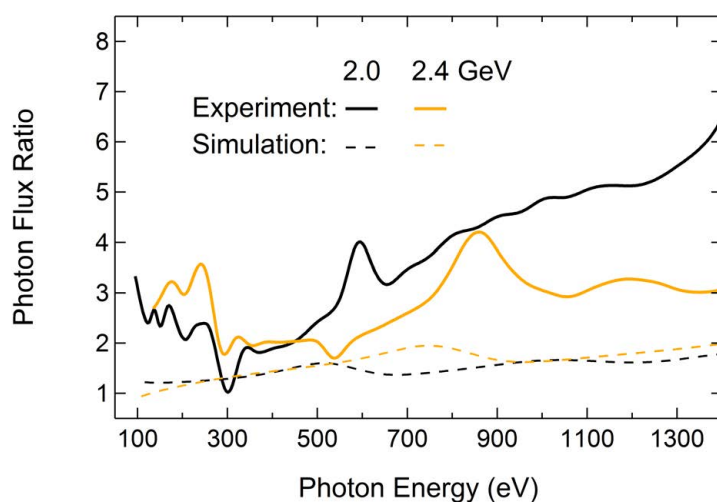


Figure 2.22: Flux comparison between the old and new insertion device.

due to adsorption of atomic/molecular species or because of the interaction with graphene. For instance, this advantage was greatly exploited in order to understand the growth mechanism of the *h*-BN single layer (Chapter 3), or the oxygen intercalation process (Chapter 4) and the formation of an oxide layer (Chapter 5) below graphene.

Monochromator energy resolution. Most of the time, the evaluation of the energy resolution for a soft X-ray monochromator is done by measuring the core level photoabsorption from noble gases. This is primarily due to the fact that this method does not involve any complicated detector, such as an electron energy analyzer, which would add extra broadening to the experimental data. The lifetime of the core hole excited states is, in the ideal case, long enough so that their natural linewidth (Γ) should be much smaller than the value of the monochromator resolution. Because of the high resolutions achieved, however, only very few atomic or molecular states fulfill such a requirement.

In order to determine the energy resolution, we measured the absorption thresholds of some selected gases, namely, argon, nitrogen and neon, with a small gas ionization cell placed behind the sample. Fig. 2.23 depicts the two-plate ionization chamber used for the photoionization measurements. The absorption spectra are measured by recording the ion current passing through the electrodes kept at different potentials. The ionization cell is connected to the gas inlet system, which allows a rapid gas exchange. The measurements were performed with the exit slit aperture set at $10 \mu\text{m}$ and with the monochromator operating in first order harmonic for Ar and

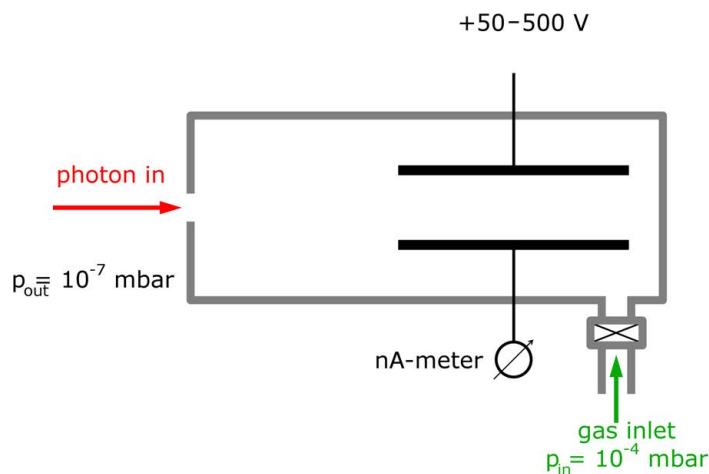


Figure 2.23: Sketch of the ionization cell employed for measuring the photoabsorption spectra of the noble gases.

N_2 , and in second order harmonic for Ne. The horizontal position of the exit slit depends on the angles of incidence, α , and diffraction, β , at the plane grating through the focus constant $C_f = \cos \beta / \cos \alpha$. The most commonly used value is $C_f = 2.25$. However, in order to search for the best resolution, this parameter can be modified: larger (lower) values of C_f give better (worse) resolution and worse (better) 2^{nd} order suppression. The spectra shown in fig. 2.24 have been recorded using this approach.

Fig. 2.24(a) shows a portion of the $L_{2,3}$ absorption spectra of argon, obtained with 4.5×10^{-7} mbar Ar pressure in the gas cell and +200 eV bias potential. The peak at 243.8 eV corresponds to the transition $2p \rightarrow 4s$, which is commonly used to probe the spectral resolving power $E/\Delta E$ of soft X-rays beamlines. In order to get a quantitative information on the monochromator resolution this excitation has been fitted with a Voigt function (dashed curve). The superposition of Lorentzian and Gaussian profiles accounts for lifetime and experimental broadening, respectively. Assuming a natural linewidth of 121 meV, in accordance with the literature [27], the Gaussian width is found to be 16 meV, which corresponds to a resolving power of about 15000. The core level vibrational structure of the $1s \rightarrow \pi^*$ transition of gaseous N_2 is shown in fig. 2.24(b). This spectrum has been measured at 2.3×10^{-7} mbar N_2 pressure. This excitation is widely used to determine the resolution in the 400 eV photon energy range [28]. In particular, the ratio of the first valley (399.8 eV) to the third peak from the left (400.1 eV) is very sensitive to the spectral resolution. Here we found a ratio of 0.8 in first order diffraction, while the best reported value is 0.7 for a measurement in the second order [29]. Assuming a Lorentzian natural linewidth of 128 meV [30], the separation of adjacent vibrational peaks

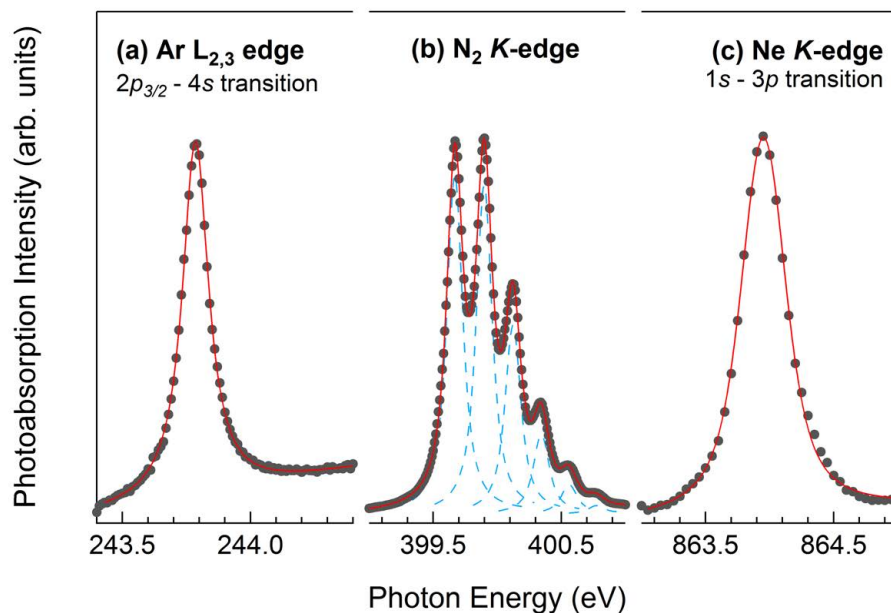


Figure 2.24: Photoabsorption spectrum of Ar (a), N_2 (b) and Ne (c) in gas phase.

ranges from 212 to 230 meV. The corresponding Gaussian width is 55 meV, which results in a resolving power of about 7000. Finally, the $1s \rightarrow 3p$ transition at about 864 eV of the Ne K -edge is used to characterize the spectral resolution at higher photon energy (fig. 2.24c). In this case, we assumed a natural linewidth of 265 meV [31] and found Gaussian width of 251 meV, indicating a resolving power of about 3500.

Bibliography

1. Siegbahn, K. M. in *Nobel Lectures in Physics 1981-1990* (ed Ekspong, G.) (World Scientific Publishing Company, Singapore, 1993).
2. Fadley, C. S., Hagstrom, S. B. M., Klein, M. P. & Shirley, D. A. Chemical effects on core-electron binding energies in iodine and europium. *The Journal of Chemical Physics* **48**, 3779 (1968).
3. Mårtensson, N. & Nilsson, A. On the origin of core-level binding energy shifts. *Journal of Electron Spectroscopy and Related Phenomena* **75**, 209 (1995).
4. Woodruff, D. P. & Delchar, T. A. *Modern techniques of surface science, 2nd edition* (Cambridge University Press, 1994).
5. Bransden, B. H. & Joachin, C. J. *Physics of atoms and molecules, 2nd edition* (Prentice Hall, 2003).
6. Bersuker, I. B. *Electronic structure and properties of transition metal compounds: Introduction to the theory, 2nd edition* (John Wiley & Sons, 2010).
7. Hüfner, S. & Wertheim, G. K. Core-line asymmetries in the x-ray photoemission spectra of metals. *Physical Review B* **11**, 678 (1975).
8. Nordling, C., Sokolowski, E. & Siegbahn, K. Precision method for obtaining absolute values of atomic binding energies. *Physical Review* **105**, 1676 (1957).
9. Sokolowski, E., Nordling, C. & Siegbahn, K. Chemical shift effect in inner electronic levels of Cu due to oxidation. *Physical Review* **110**, 776 (1958).
10. Nordling, C., Hagström, S. & Siegbahn, K. Application of electron spectroscopy to chemical analysis. *Zeitschrift für Physik* **178**, 433 (1964).
11. Citrin, P. H., Wertheim, G. K. & Baer, Y. Core-level binding energy and density of states from the surface atoms of gold. *Physical Review Letters* **41**, 1425 (1978).
12. Wertheim, G. K. & Citrin, P. H. Surface-atom core-level shifts of W(111). *Physical Review B* **38**, 7820 (1988).

13. Van der Veen, J. F., Himpsel, F. J. & Eastman, D. E. Structure-dependent 4f-core-level binding energies for surface atoms on Ir(111), Ir(100)-(5 × 1), and metastable Ir(100)-(1 × 1). *Physical Review Letters* **44**, 189 (1980).
14. Puglia, C. *et al.* Physisorbed, chemisorbed and dissociated O₂ on Pt(111) studied by different core level spectroscopy methods. *Surface Science* **342**, 119 (1995).
15. Citrin, P. H. & Wertheim, G. K. Photoemission from surface-atom core levels, surface densities of states, and metal-atom clusters: a unified picture. *Physical Review B* **27**, 3176 (1983).
16. Citrin, P. H., Wertheim, G. K. & Baer, Y. Many-body processes in x-ray photoemission line shapes from Li, Na, Mg, and Al metals. *Physical Review B* **16**, 4256 (1977).
17. Doniach, S. & Šunjić, M. Many-electron singularity in x-ray photoemission and x-ray line spectra from metals. *Journal of Physics C: Solid State Physics* **3**, 285 (1970).
18. Woodruff, D. P. & Bradshaw, A. M. Adsorbate structure determination on surfaces using photoelectron diffraction. *Reports on Progress in Physics* **57**, 1029 (1994).
19. Rehr, J. J. & Albers, R. C. Scattering-matrix formulation of curved-wave multiple-scattering theory: Application to x-ray-absorption fine structure. *Physical Review B* **41**, 8139 (1990).
20. García de Abajo, F. J., Van Hove, M. A. & Fadley, C. S. Multiple scattering of electrons in solids and molecules: A cluster-model approach. *Physical Review B* **63**, 075404 (2001).
21. Vickerman, J. C. & Gilmore, I. S. *Surface analysis – The principal techniques, 1st edition* (John Wiley & Sons, 2009).
22. Stöhr, J. *NEXAFS spectroscopy* (Springer, 1992).
23. Krause, M. O. Atomic radiative and radiationless yields for K and L shells. *Journal of Physical and Chemical Reference Data* **8**, 307 (1979).
24. Iwanenko, D. & Pomeranchuk, I. On the maximal energy attainable in a betatron. *Physical Review* **65**, 343 (1944).
25. Schwinger, J. On the classical radiation of accelerated electrons. *Physical Review* **75**, 1912 (1949).
26. Cautero, G. *et al.* A two-dimensional detector for pump-and-probe and time resolved experiments. *Nuclear Instruments and Methods in Physics Research Section A* **595**, 447 (2008).

27. King, G. C., Tronc., M., Read, F. H. & Bradford, R. C. An investigation of the structure near the $L_{2,3}$ edges of argon, the $M_{4,5}$ edges of krypton and the $N_{4,5}$ edges of xenon, using electron impact with high resolution. *Journal of Physics B: Atomic and Molecular Physics* **10**, 2479 (1977).
28. Chen, C. T. & Sette, F. Performance of the Dragon soft x-ray beamline. *Review of Scientific Instruments* **60**, 1616 (1989).
29. C. U. S. Larsson and A. Beutler and O. Björneholm and F. Federmann and U. Hahn and A. Rieck and S. Verbin and T. Möller. First results from the high resolution XUV undulator beamline BW3 at HASYLAB. *Nuclear Instruments and Methods in Physics Research Section A* **337**, 603 (1994).
30. Domke, M. *et al.* Performance of the high-resolution SX700/II monochromator. *Review of Scientific Instruments* **63**, 80 (1992).
31. Coreno, M. *et al.* Measurement and ab initio calculation of the Ne photoabsorption spectrum in the region of the K edge. *Physical Review A* **59**, 2494 (1999).

Chapter 3

Growth and Characterization of Hexagonal Boron Nitride on Ir(111)

3.1 Introduction

As already pointed out in the introductory Chapter to this thesis, prompted by the popularity of graphene technologies, in the last years researchers have started to explore other layered systems. In this regard, *h*-BN is attracting great interest because, due to its intrinsic insulation and structural similarity to graphene, is the natural candidate as a substrate for graphene-based electronic devices. Indeed, transport measurements of graphene devices on *h*-BN substrate show largely improved charge carrier mobility compared to those on SiO₂ platforms [1]. Furthermore, it was shown that *h*-BN can be used as template for arranging molecules in a controlled, ordered fashion, [2, 3] thus paving the way for the development of novel nanodevices [4]. In this respect, *h*-BN is considered a promising candidate, especially after the discovery by Corso *et al.* [5] of the formation of a self-assembled nanostructure, the so-called nanomesh, on the Rh(111) surface.

Among the several methods to synthesize *h*-BN single layers, one of the most commonly employed to obtain high-quality films is by CVD of benzene-like B₃N₃H₆ at transition metal surfaces. Many of these studies concern the growth on substrates with the same C_{3v} symmetry as *h*-BN, namely, (111) and (0001) hexagonal surfaces of face-centered cubic (*fcc*) and hexagonal closed-packed (*hcp*) crystals, respectively. Illuminating examples are Ni(111) [6–9], Rh(111) [10], Pt(111) [10, 11] and Ru(0001) [12, 13]. In addition, there are few investigations of *h*-BN growth on top of more open surfaces, such as Ni(110) [14], Cr(110) [15], Pd(110) [16] and Mo(110) [17].

So far, most of the research has been focused on the characterization of the morphology and electronic structure of the single layer, but little

is known on the processes that lead chemisorbed borazine molecules to form an extended and long-range ordered *h*-BN film. Only a few investigations report on the adsorption and interaction of borazine with metallic surfaces¹ [19–22]. Borazine has been found to bound with the molecule ring either perpendicular, on Pt(111) [19, 20], or parallel to the surface, as in the case of Au(111) [20] and Ru(0001) [21] substrates. This behaviour resembles that of benzene (C₆H₆) adsorption on metallic supports, although the C₆H₆ molecules adsorb prevalently in flat geometry [23, 24]. An exhaustive picture of the chemisorption properties of borazine on transition metals is therefore still missing.

In this context, it has to be stressed that the adsorption and nucleation mechanisms greatly influence the final quality of the *h*-BN layer. Therefore, addressing these fundamental issues is an important preliminary study to shed light on the assembly of *h*-BN single layers with outstanding crystalline perfection. A strategy to improve the quality of the *h*-BN film is to apply low precursor pressure combined with high substrate temperature [25], or to simultaneously expose the metal surface to borazine and hydrogen [26]. Nevertheless, it is challenging to obtain large single crystalline domains because of the formation of rotated phases that give rise to grain boundaries and other 1D defects [27]. For instance, the nucleation of rotational domains has been reported for systems characterized by a weak interfacial bonding, like Pd(111) [28], Cu(111) [29] and Ag(111) [30]. Moreover, the formation of misoriented domains has been observed also in the case of strongly chemisorbed *h*-BN monolayers, such as on Ni(111) [31] and Rh(111) [25]. The origin of the rotational domains has been traced back to factors like commensurability, symmetry, interaction with the substrate, and also chemistry of the precursor [28, 32, 33]. To date, however, the control of the relative abundance of these structures is far from being achieved: much effort is still needed in order to achieve the highest quality for *h*-BN films on metal surfaces.

The critical issues of *h*-BN growth on metal supports outlined above, that is, early stage borazine adsorption and optimization of the CVD method, are the subject of the comprehensive study presented in this Chapter. Using in situ high-energy resolution XPS, in combination with complementary experimental techniques (see Chapter 2), we first show that borazine adsorbs molecularly on Ir(111) at 170 K, with the molecule ring oriented parallel to the substrate. Molecular dissociation occurs near room temperature, with dehydrogenation accompanied by partial cracking of the borazine ring, a process which precedes the formation of the *h*-BN lattice. Furthermore, we demonstrate a CVD strategy to foster the growth of *h*-BN layers with single orientation on a weakly interacting substrate such

¹For the sake of completeness, it is noteworthy mentioning the study of the reaction of borazine with the semiconducting Si(100) surface [18].

as the Ir(111) surface by properly controlling the synthesis conditions. We adopted two different growth procedures and subsequently characterized the geometry of the resulting *h*-BN layers by means of electron and photoelectron diffraction techniques. We find that, while the ordinary high-temperature borazine deposition gives rise to the nucleation of opposite-oriented *h*-BN domains, a monolayer with a single orientation can be synthesized by room temperature borazine exposure followed by annealing.

3.2 Experimental Details

The Ir(111) surface was prepared by repeated cycles of Ar⁺ sputtering, oxygen treatment between 600 and 1000 K to remove carbon atoms eventually segregated from the bulk crystal, and hydrogen exposure to 800 K to remove oxygen atoms adsorbed on the crystal surface. After this cleaning procedure, the LEED pattern appears sharp and exhibits a low intensity background. Borazine was synthesized following the procedure described by Wideman *et al.* [34], and stored below 250 K to avoid its degradation. Prior to each exposure, borazine was regularly purified by repeated freeze-thaw cycles. In order to enhance the surface signal, during the TPD experiments the sample was placed in front of the mass spectrometer equipped with a Feulner cup [35].

The high-energy resolution XPS Ir 4 $f_{7/2}$, B 1 s and N 1 s core-level spectra were collected using photon energies of 130, 284 and 500 eV, respectively, with an overall energy resolution (electron energy analyzer and X-ray monochromator) ranging from 40 to 100 meV. The XPD measurements were performed with photon energies corresponding to electron kinetic energies of 115, 120 and 315 eV. At each of these energies 1140 spectra were measured, corresponding to different polar (θ) and azimuthal (ϕ) angles. Each XPD pattern was measured over a wide azimuthal sector, ranging from 120° to 140°, from normal ($\theta = 0^\circ$) to grazing emission ($\theta = 80^\circ$). The reported modulation functions were obtained for each polar emission angle θ from the peak intensity $I(\theta, \phi)$ as $(I(\theta, \phi) - I_0(\theta))/I_0(\theta)$, where $I_0(\theta)$ is the average intensity for each azimuthal scan. The theoretical XPD patterns were calculated with the Electron Diffraction in Atomic Cluster (EDAC) simulation code [36].

3.3 Results and Discussion

3.3.1 Low Temperature Borazine Adsorption

Fig. 3.1a reports the temporal evolution of the B 1 s spectra during B₃N₃H₆ uptake on the Ir(111) substrate at 170 K. At low exposure, a single component grows at a binding energy of 189.7 eV (B_{mol}). This component reaches

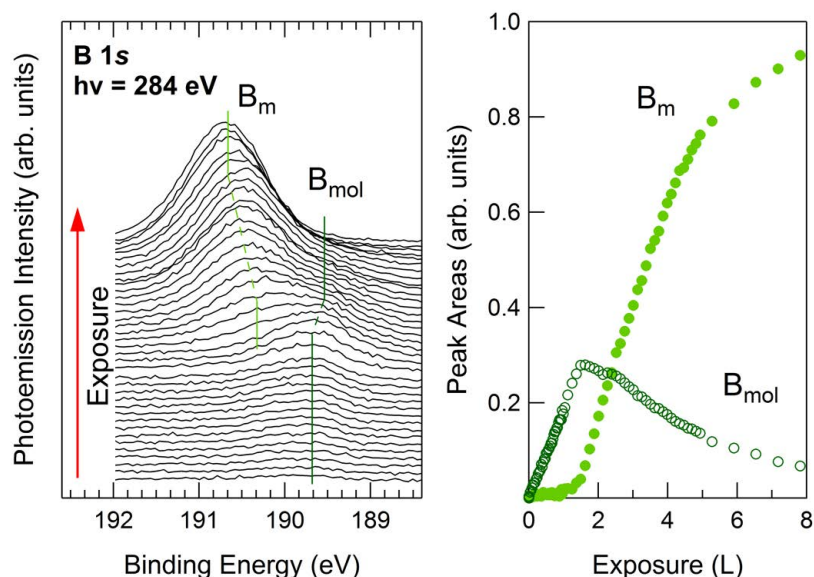


Figure 3.1: (a) Selected B 1s core level spectrum measured during $B_3N_3H_6$ exposure on Ir(111) at 170 K, together with the fitting components B_{mol} and B_m associated with the low coverage population of borazine molecules and the multilayer system, respectively. (b) Evolution of the intensity (normalized to the saturation value) of the spectral components as a function of the borazine exposure.

saturation at ~ 1 L ($1 \text{ L} = 1 \times 10^7 \text{ Torr}\cdot\text{s}$), while a new peak emerges at 190.3 eV (B_m). The new B_m feature grows with increasing borazine exposure and did not saturate, as depicted in fig. 3.1b, which shows the evolution of the B 1s components as a function of the $B_3N_3H_6$ exposure. This behaviour suggests the formation of a multilayer structure associated with the B_m component, in analogy with the results previously reported for benzene adsorption on the Pd(111) surface [37]. The progressive shift of B_m by about 600 meV towards higher binding energy is most likely due to final state effects [38, 39]. Indeed, it is well known that the relaxation and screening of the core-hole can significantly modify the measured binding energy. The intensity of these effects varies depending on the boundary conditions, in terms of charge relaxation of the emitter atom. In this case, compared to the first-layer chemisorbed molecules, the core-hole screening by the metal surface becomes less efficient as the thickness of the multilayer film increases. Obviously, the contribution of initial state effects cannot be neglected.

Fig. 3.2 displays the B and N K-edge NEXAFS spectra measured for 1.1 and 3.3 L borazine exposure. At 1.1 L exposure, four peaks can be distinguished in the N K-edge spectra: A_1 , A_2 , A_3 and A_4 at 398.2, 399.3, 400.7 and 402.0 eV photon energy, respectively (fig. 3.2 (a)). By comparison with

the borazine electronic structure in the gas phase [40], these resonances are assigned to transitions from the N $1s$ core level towards molecular orbitals with π character. However, borazine shows only two unoccupied π orbitals, namely, $\pi^*(e'')$ and $\pi^*(a_2'')$, while in this case we observe four resonances. Most likely, the additional resonances are the result of non-equivalent adsorption configurations of borazine molecules on the Ir(111) surface. The pronounced angle dependence of A_1 and A_3 , which are clearly visible in the spectra measured at grazing incidence (black curve, $\theta_{ph} = 70^\circ$) and almost vanished at normal incidence (red curve, $\theta_{ph} = 0^\circ$), is consistent with the presence of molecules adsorbed with the plane of the hexagonal ring parallel to the surface. On the other hand, A_2 and A_4 are measured at both incidence angles, and therefore their intensity do not depend on the polarization of the incoming photon beam. These features are thus related to molecules that are tilted away from the iridium surface. The shift of about 3 eV between $\pi^*(e'')$ and $\pi^*(a_2'')$ resonances, which is quite close to 3.3 eV shift measured in gas phase borazine [40], further supports our assignments. The broad features observed above 405 eV, instead, are associated with σ -related orbitals. The interpretation of the B K-edge NEXAFS is in line with the above analysis. However, the resonances are quite broad, rendering the identification of their exact position difficult, except for A_2 and A_3 resonances at 190.5 and 191.5 eV, respectively. It is noteworthy that around 1 L the low coverage adsorption state saturates, while the multilayer state only starts to be populated (fig. 3.1). Therefore, we assign the intense A_1 and A_3 resonances of flat-lying borazine to the B_{mol} photoemission component, and we associate A_2 and A_4 , corresponding to the tilted bonding geometry, with the B_m component.

In going from 1.1 to 3.3 L, the intensity of A_2 increases and its polarization dependence is lost, this resonance being visible at both incidence angles. This suggests the preferential growth of the tilted borazine population, in accordance with the development of the multilayer structure. Furthermore, we do observe a close similarity between the gas phase borazine EELS reported in Ref. [40] and the NEXAFS measured for the multilayer phase that can be explained by considering that the disorder of the multilayer structure is analogous to the random molecular orientation in the gas phase. This finding further supports our assignment of the two π^* transitions to different adsorption geometries.

Taken together, the XPS and NEXAFS data state that the adsorption configuration depends on the degree of borazine coverage which, in turn, is determined by the size of the molecule. Hence, the ready availability of free surface plays a fundamental role in the borazine adsorption mechanism on Ir(111). In order to evaluate the amount of borazine deposited during the evaporation, we compared the total B $1s$ (or N $1s$) intensity of the corresponding spectra with that of the h -BN single layer. The full substrate coverage of h -BN is 2.34 ML (see section 3.3.3) and corresponds to a boron

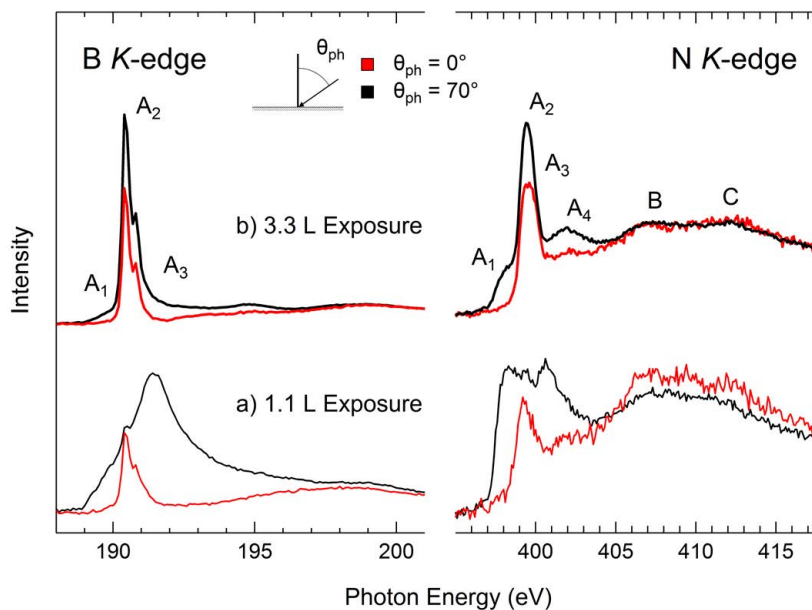


Figure 3.2: N and B K-edge NEXAFS for (a) 1.1 and (b) 3.3 L borazine exposure on Ir(111) at 170 K. Red (black) spectra are recorded with the angle between the surface normal and the direction of photon polarization $\theta_{ph} = 0^\circ$ (70°).

(nitrogen) coverage of 1.17 ML, where 1 ML is the surface atomic density of the Ir(111) surface. Using this value, we calculated a boron (nitrogen) coverage of 0.6 ML at the saturation of B_{mol} (after exposure to ~ 1 L borazine), which corresponds to a molecular coverage of 0.2 ML, since there are three boron atoms per borazine molecule. A single borazine molecule adsorbed with the plane of the ring parallel to the Ir(111) covers an area of 32.7 \AA^2 .² The lattice constant of the Ir(111) surface is 2.715 \AA , corresponding to an area of 6.4 \AA^2 per unit cell. Therefore, assuming a close-packed configuration, the theoretical saturation coverage of borazine on Ir(111) turns out to be 0.19 ML. This value has to be considered only a crude approximation of the maximum packing since it does not take into account photoelectron diffraction effects, that could modify the photoemission intensity, nor the adsorbate-substrate registry. Nevertheless, the good agreement between the ‘experimental’ and ‘theoretical’ coverage suggests that the 1.1 L exposed Ir(111) surface is completely saturated. Furthermore, this result could also be taken as an indication that the saturation coverage is driven by borazine lateral interactions.

²This value is calculated by assuming the following interatomic distances: B–N=1.4 Å, B–H=1.2 Å, N–H=1.0 Å [41]. The van der Waals radius of the aromatic hydrogen atom is 1.0 Å [42].

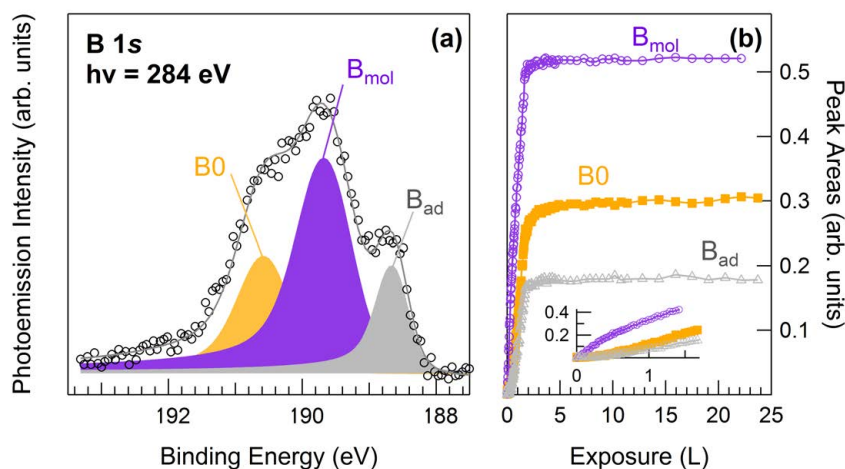


Figure 3.3: (a) B $1s$ core level of the $B_3N_3H_6$ saturated (25 L exposure) surface at 330 K, the spectral components are shown superimposed (see text for details). (b) Intensity evolution (normalized to the saturation value) as obtained by fitting the B $1s$ spectra measured during the $B_3N_3H_6$ uptake.

In summary, up to coverages of about 0.20 ML, borazine is π bonded to the Ir substrate with its plane oriented parallel to surface. Subsequent surface crowding, above 0.20 ML, forces the molecules to bind in a tilted configuration, eventually forming a multilayer structure on top of the first chemisorbed layer. It is noteworthy that borazine has been proposed to lie flat on Ru(0001) [21] and Re(0001) [22], with room temperature saturation coverages of 0.15 and 0.23 ML, respectively, as determined from attenuation of the substrate Auger electron spectroscopy (AES) signal. Also on the Au(111) surface, a binding geometry with the plane of the borazine ring parallel to the substrate has been reported, in contrast to the vertical geometry proposed for borazine adsorption on Pt(111) [20].

3.3.2 From Undissociated Borazine to h -BN

While the low-temperature adsorption does not show any indication of borazine dissociation, the situation becomes quite different at higher temperature. Fig. 3.3a displays the B $1s$ spectrum measured after exposure to 25 L of borazine at a sample temperature of 330 K. Several spectral contributions can be distinguished: B0, B_{mol} and B_{ad} , at binding energies of 190.5, 189.6, and 188.6 eV, respectively. The intensity evolution of the different components as a function of the borazine exposure is shown in fig. 3.3b. The line shape of the three peaks was fixed during the fitting analysis of the whole sequence. At the beginning of the borazine uptake, only B_{mol}

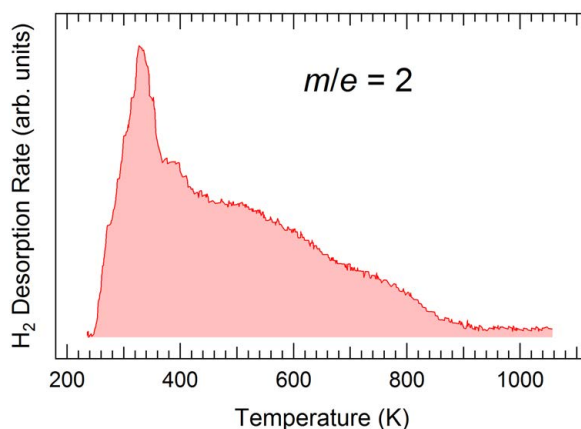


Figure 3.4: Thermal desorption spectra obtained during annealing (3 K s^{-1}) of the borazine saturated surface (11 L exposure at 170 K). H_2 desorbs between 250 and 900 K, with a maximum desorption rate at 330 K.

is observed, while the other two components rise at slightly higher exposures (above 0.3 L). The binding energy of the B_{mol} component is close to the value reported in the previous section for the low-temperature borazine adsorption. This contribution is therefore assigned to borazine molecules which adsorb intact on Ir(111). It is noteworthy that B_0 and B_{ad} grow almost simultaneously, although with different rates, thus suggesting a common origin of the two components. At saturation, above 2 L exposure, the relative populations of these species are 52% (B_0) and 32% (B_{ad}) with respect to B_{mol} . The attribution of B_0 and B_{ad} to non-equivalent B atoms within the borazine molecule appears unlikely, because the ratio B_0/B_{ad} is not constant during the uptake. From the XPS and LEED characterization of the clean surface we could expect a low density of surface defects. For this reason, also due to the high intensity of B_0 and B_{ad} , we can rule out the possibility of preferential adsorption at defective sites. Furthermore, induced photodissociation can be excluded since the photoemission spectra do not undergo any modification with time when the surface is exposed to the photon beam. Hence, it is most probable that borazine molecules dissociate on Ir(111) at 330 K, giving rise to the B_0 and B_{ads} components. The binding energy position of B_{ad} is close to the value of 188.4 eV reported for diluted boron in Rh(111) [43]. Therefore, it is realistic to assign the B_{ad} component to boron adatoms and B_0 to borazine fragments.

In order to prove that $\text{B}_3\text{N}_3\text{H}_6$ dissociation occurs on the Ir(111) surface exposed at room temperature, we performed a TPD experiment. Fig. 3.4 shows the H_2 thermal desorption spectra ($m/e = 2$) from the iridium surface exposed to 11 L of borazine at 170 K. As can be seen from the hydrogen desorption curve, the dehydrogenation starts already at 250 K and

continues over a broad temperature range up to 900 K, with a maximum desorption rate at about 330 K. These findings resemble those obtained on $B_3N_3H_6/Pt(111)$ by Simonson *et al.* [20], reporting a broad H_2 desorption peak with a maximum at 285 K. The desorption maxima falls within the temperature range of H_2 desorption from the Ir(111) surface exposed to hydrogen, which lies between 290 and 370 K, depending on the initial coverage [44]. Therefore, our data are also compatible with a borazine dehydrogenation process followed by a second-order recombinative H_2 desorption. To deepen the understanding on the interaction of borazine fragments with the iridium substrate prior to the formation of the *h*-BN layer, we monitored the evolution of the B $1s$ and Ir $4f_{7/2}$ spectra after annealing up to different increasing temperatures, ranging from 470 to 1370 K. The sequence of spectra is reported in fig. 3.5. As can be seen, the B0 component grows with increasing temperature and moves towards lower binding energies, while the intensity of both B_{mol} and B_{ad} gets reduced. Upon annealing to 620 K, a new component at 190.8 eV (B1) has to be included in the analysis to achieve a low residual modulation. The intensity of this component increases progressively up to 1120 K. Between 1120 and 1370 K, a complete suppression of B_{mol} and B_{ad} is observed, while B0 and B1 shift by about 0.3 eV towards lower binding energy. The B0 and B1 peak positions and line shapes are quite close to those characteristics of the extended *h*-BN monolayer (see Section 3.3.3).

The Ir $4f_{7/2}$ core level spectrum of the clean substrate exhibits the bulk component at 60.83 eV, IrB, and the surface component, IrS, at 60.28 eV. The line shape parameters and the measured SCLS of -540 meV are in good agreement with previous determinations [45] and theoretical calculations [46]. Upon borazine exposure, a new broad feature (IrS2) at 60.61 eV grows between the surface and the bulk component. This is paralleled by a drop of the IrS peak intensity and a slight reduction of its SCLS to -505 meV. The same parameters of the clean surface component were used to describe the line shape of the adsorbate-induced IrS2 peak. Upon increasing the annealing temperature, IrS2 continuously decreases, while IrS almost recovers the intensity of the clean surface and shifts towards lower binding energy, eventually reaching a SCLS of about -535 meV, which is very close to the value measured on clean Ir(111). At the same time, as expected, the binding energy position of the bulk peak remains fixed.

The XPS results clearly indicate that the $B_3N_3H_6$ molecule undergoes dissociation on Ir(111) close to room temperature. However, the photoemission peaks corresponding to molecular fragments and boron adatoms can be detected only for exposures larger than 0.3 L, when the slope of the B_{mol} intensity curve decreases (see inset in fig. 3.3). These findings suggest that borazine dissociation does not occur in the initial stage of the adsorption: the first adsorbed molecules keep their benzene-like ring intact, giving rise to the B_{mol} spectral component.

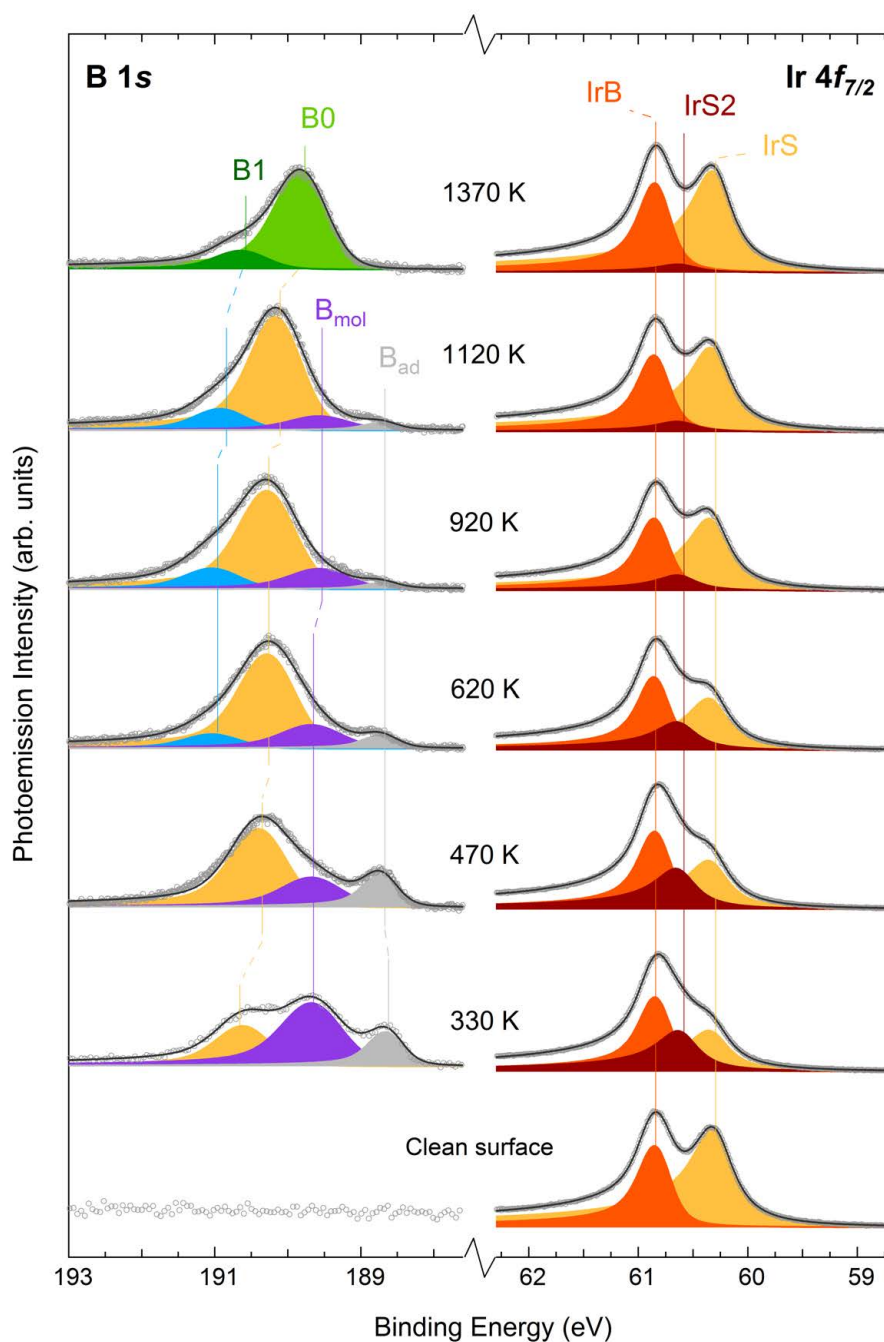


Figure 3.5: High-energy resolution B 1s and Ir 4f_{7/2} core level spectra for the clean substrate (bottom), the B₃N₃H₆ saturated (25 L exposure at 330 K) Ir surface and after fast annealing to the listed temperatures, together with the different spectral contributions. All curves are plotted after linear background removal.

Molecular decomposition takes place only above 0.3 L, leaving dehydrogenated molecules and molecular fragments (B0), and boron adatoms (B_{ad}) on the surface. A temperature as high as 930 K was suggested for the B-N bond breaking process taking place on Rh(111) [25]. Here, instead, the presence of atomic boron indicates that the borazine ring cracks already at 330 K. This value compares to the detection of atomic B and N species by Auger electron spectroscopy on the Re(0001) surface exposed to borazine and annealed to 570 K [22]. Further molecular dissociation is observed at higher temperature, as depicted by the intensity drop of B_{mol} and by the increase of B0 components (see fig. 3.5).

At the same time, B_{ad} loses intensity, suggesting a depletion of boron adatoms. It is interesting to note that (i) after exposure at room temperature the intensity of B_{ad} is approximately 17% of the total B 1s signal and that (ii) subsequent annealing of the system results in a decrease of the photoemission intensity by almost the same amount, the drop being of about 15%. The total intensity of the N 1s core level (not shown here) diminishes by about the same quantity ($\sim 20\%$). Therefore, although the contribution due to photoelectron diffraction effects cannot be excluded, this reduction is likely due to a partial depletion of the B and N species on the iridium surface. In this respect, the diffusion of atomic boron into the bulk – a similar behaviour was previously observed for boron adsorbed on Pd(111) [47] and Ni(100) [48] – and/or desorption of NH_x or N_2 species seem to be the most plausible processes [49].

This trend in the intensity evolution of B0, B_{mol} and B_{ad} , continues above 620 K, paralleled by the appearance of a new feature (B1). Our findings can be explained by comparison with the *h*-BN growth process on Rh(111) [25]. Dong *et al.* evidenced a first reorganization into nanometer-scale clusters at 690 K, with the *h*-BN structure emerging already below 900 K. In agreement with the proposed mechanism, we interpret the observed changes in our XPS spectra as due to the earliest rearrangement of dehydrogenated molecules and fragments to form islands with *h*-BN morphology; this means that the islands are already characterized by strongly and weakly bonded regions, associated with B1, N1 and B0, N0 components, respectively (see next section). As the temperature is further increased, B0 and B1 shift towards lower binding energy, while B_{mol} and B_{ad} disappear. The evolution, in terms of binding energy and intensity of the boron spectral components, reflects the coalescence of the dehydrogenated BN rings and molecular fragments, a process which ends up with the completion of the *h*-BN layer. The proposed mechanism is confirmed also by the behaviour of the hydrogen desorption curve shown in fig. 3.4. Beyond the main desorption feature close to room temperature, dehydrogenation extends over a wide temperature range, up to 900 K, due to the dehydrogenation of both intact-ring molecules and molecular fragments adsorbed on the surface. It has to be stressed that the *h*-BN film obtained in this way

covers an area which is about 60% that of a full BN monolayer. Indeed, at room temperature, part of the hydrogen atoms are still bonded to the borazine molecules, which therefore occupy a greater area than the hexagons in the final *h*-BN configuration. In order to increase the coverage it is either possible (i) to repeat the cycles of room temperature borazine exposure followed by annealing until saturation of the surface or (ii) to expose the Ir substrate directly at high temperature in order to promote the prompt desorption of hydrogen. These growth procedures are described in detail in the next section.

The variations of the adsorbate chemical composition and structure lead to large changes also in the Ir $4f_{7/2}$ spectra. The SCLS of clean Ir(111) is due to the narrowing of the surface *d*-band that gives rise to a shift of the surface component IrS to lower binding energies (Section 2.3.1). In this respect, it is well-known that atomic and molecular adsorption on transition metal surfaces typically induces a broadening of the substrate *d*-band, together with a lowering of the density of states at the Fermi level. As a result, for transition metals with a more than half-filled *d*-band, a shift towards higher binding energy of the *d*-band of the surface atoms interacting with the adsorbate with respect to that of the clean atoms is observed. This effect applies also to the adsorbate-induced IrS2 [50] component, which indeed shows an upward binding energy shift compared to IrS. The intensity gain of IrS at the expense of IrS2 upon annealing, clearly reflects the reorganization of the adsorbates from a disordered structure, composed of several chemical species strongly interacting with the Ir surface, into an ordered *h*-BN lattice, when the interaction with the substrate is strongly reduced. Similar findings have been reported for graphene growth on Ir(111) [46, 51], where the interaction with the substrate is strongly reduced (further details on the graphene/Ir(111) interface are given in Chapter 4). Indeed, ethylene adsorption at room temperature followed by annealing [46], gives rise to a third photoemission feature between surface and bulk components due to the first-layer Ir atoms interacting with the chemisorbed C_xH_y species. Moreover, as in our case, increasing the substrate temperature results in a continuous intensity reduction of the adsorbate-induced peak, paralleled by the growth of the clean surface component. This behaviour has been explained in terms of the evolution from strongly chemisorbed ethylene molecules to graphene, which is very weakly interacting with Ir(111) [46]. These same considerations can be therefore applied also to the *h*-BN growth on Ir(111).

3.3.3 *h*-BN Single Layer

Two different procedures have been followed to grow an extended *h*-BN single layer. The first method consisted in the exposure of the Ir(111) surface at 1070 K to $p = 5 \times 10^{-8}$ mbar of borazine (Growth 1). The second ap-

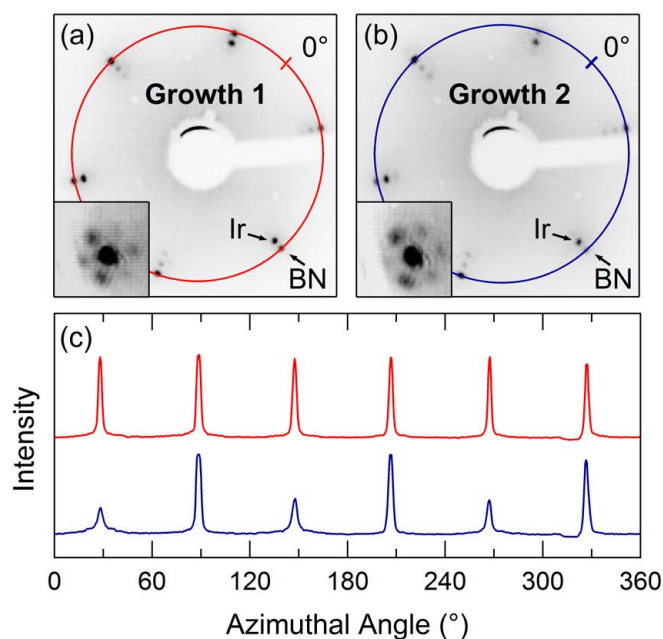


Figure 3.6: LEED patterns measured at 83 eV for *h*-BN synthesized according to (a) Growth 1 and (b) Growth 2 procedures. Insets: zoom-in of the principal spots measured at 55 eV. (c) The six- and three-fold symmetry of the patterns is clearly shown by the line profile analysis along the colored rings containing the BN spots in (a) and (b) with red and blue lines, respectively.

proach, instead, consisted in repeated cycles of borazine exposure at room temperature at pressure $p \sim 1 \times 10^{-8}$ mbar until saturation of the surface, followed by annealing to 1270 K, with a 4 K s^{-1} heating rate (Growth 2).

Fig. 3.6a,b shows the LEED patterns from the *h*-BN layers synthesized as described above. The images prove the quality and long range order of the *h*-BN layers for both growth procedures (see also zoom-in in the insets). The first-order substrate diffraction spots are surrounded by a six-fold arrangement of sharp moiré satellites, due to the formation of a coincidence lattice between the *h*-BN layer and the Ir(111) substrate. The line profile analysis reveals a superstructure with a periodicity of (13×13) BN units ($a = 2.50 \text{ \AA}$) on top of (12×12) Ir unit cells ($a = 2.72 \text{ \AA}$). This result, together with the absence of additional diffraction features that are rotated with respect to the first-order Ir-induced spots indicates that, for both synthesis procedures, the *h*-BN unit cell is aligned parallel to the $\langle \bar{1}01 \rangle$, $\langle 01\bar{1} \rangle$ or $\langle \bar{1}\bar{1}0 \rangle$ crystallographic directions. However, a comparison of the LEED intensities reveals a major difference for the two growth methods. While the Ir-induced spots always show the expected three-fold symmetry, the pattern from the *h*-BN layer grown at high temperature (fig. 3.6a) exhibits

moiré-spots with six-fold symmetry, as shown by the red intensity distribution plot in fig. 3.6c. On the other hand, for the second growth procedure, also the BN-related spots are three-fold symmetric (blue curve in fig. 3.6c). Notably, this behaviour has not been observed so far. Indeed, the LEED patterns reported in literature for lattice-mismatched *h*-BN/transition metal interfaces always show moiré intensities with six-fold symmetry [10, 28, 52, 53]. Only for the lattice-matched Cu surface a three-fold symmetric pattern has been measured, but in this case is not possible to disentangle the contributions from the substrate and the *h*-BN layer because of the overlap of the corresponding LEED spots [54].

To gain further insight into the structural properties of the *h*-BN/Ir(111) interface, XPS and XPD techniques were employed to characterize the chemical composition and structure of the system. Fig. 3.7 shows the high-resolution B 1s, N 1s and Ir 4f_{7/2} core level of the *h*-BN layer synthesized using the first method. The photoemission spectra do not show any significant difference for the two preparations. The Ir 4f_{7/2} spectrum displays the same three components described in the previous section, that is, IrB, IrS and IrS2. The double-peak structure in the B 1s and N 1s core levels is rather similar to that published in Ref. [55], where the formation of the *h*-BN layer was investigated on several transition metal surfaces. The main peaks B0 and N0 at 189.84 and 397.52 eV, respectively, are thus associated with *h*-BN regions weakly interacting with the Ir atoms, while the minor contributions B1 and N1 at 190.61 and 398.62 eV, respectively, stem from the strongly chemisorbed *h*-BN regions.

A quantitative interpretation of the overlayer morphology cannot be directly extracted from the XPS spectra since diffraction effects might affect the photoemission intensity. Therefore, in order to properly evaluate the intensity ratios N1/N0 and B1/B0, we measured the photoemission spectra at different photon energies [55], corresponding to a kinetic energy range of 40-200 eV. The average value of the N1/N0 and B1/B0 ratios calculated in this way is 0.17. This value nicely compares to the relative weight of the adsorbate-induced Ir 4f_{7/2} feature with respect to the total surface signal, IrS2/(IrS2+IrS)= 0.16. This result further confirms the overall assignment of the spectral components: N0, B0 and IrS, stem from the weakly interacting atoms, while N1, B1 and IrS2 are associated with the atoms residing in the regions where the *h*-BN layer is strongly bonded to the Ir surface.

As can be expected for an extended, long-range ordered *h*-BN layer lying flat on the substrate, the NEXAFS spectra show a marked angular dependence (fig. 3.8). Three π^* (A , A' and A'') and two σ^* (B and C) resonances can be distinguished in the N K-edge spectra. The A' and A'' resonances occur due to the orbital mixing between the Ir d orbitals and the *h*-BN π states [55], and therefore arise from the *h*-BN regions strongly interacting with the Ir atoms. In particular, A' is assigned to excitations to adsorption-induced *h*-BN gap states [56], while A'' is associated with the

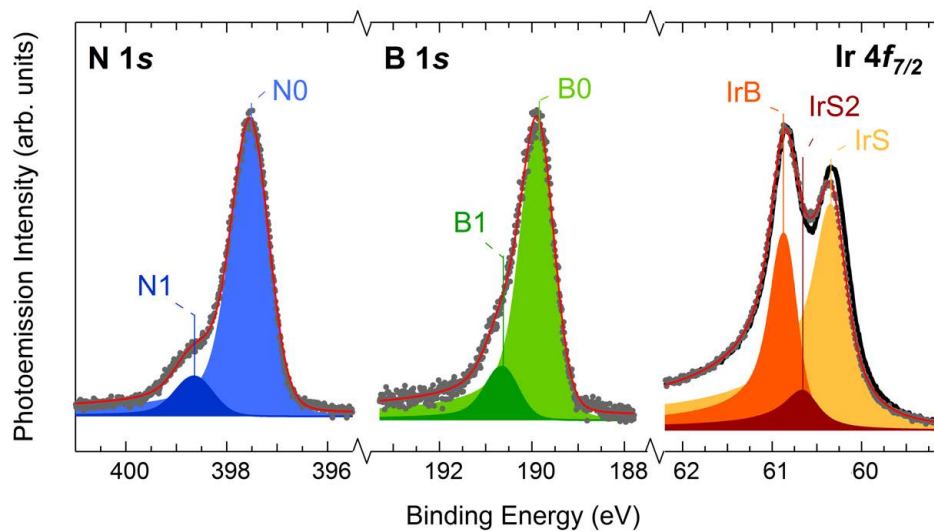


Figure 3.7: High-energy resolution Ir $4f_{7/2}$, B $1s$ and N $1s$ core level spectra measured from *h*-BN/Ir(111). The dots represent the experimental points, while the line is the result of the fit. The components used in the fit are also added. The Ir $4f_{7/2}$ spectrum from the clean surface (black, thick curve) is also shown superimposed for comparison.

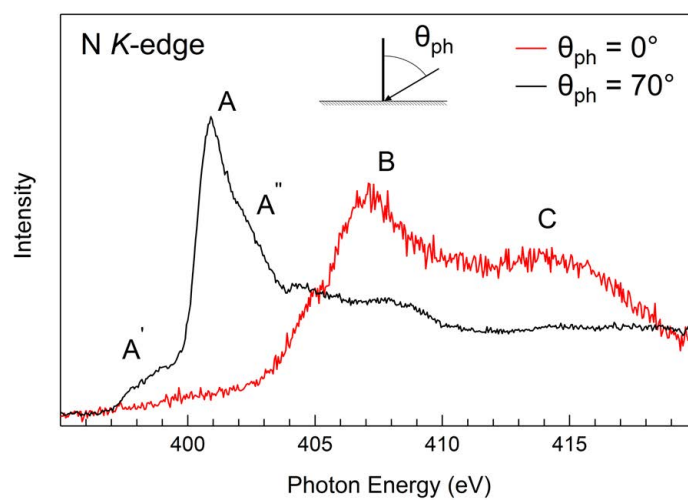


Figure 3.8: *h*-BN/Ir(111). N K-edge NEXAFS.

excitations to interlayer conduction-band states [7]. On the other hand, the π resonance *A* is measured also in the bulk *h*-BN NEXAFS spectra [7, 55] and is thus related to the lattice sites weakly bound to the metal substrate.

Fig. 3.9 depicts selected B 1*s* and N 1*s* XPD patterns for the two preparations (colored sectors), together with their multiple scattering simulations (grey regions), for two different photon energies, corresponding to photoelectron kinetic energies (E_k) of 115 and 315 eV. The modulation functions in fig. 3.9 were obtained for each polar emission angle θ from the peak intensity $I(\theta, \phi)$ as $(I(\theta, \phi) - I_0(\theta))/I_0(\theta)$, where $I_0(\theta)$ is the average value of each azimuthal scan (see also Section 2.4). The simulations have been performed with the EDAC package for a free-standing, flat *h*-BN layer. No symmetry was imposed to the experimental data. Let us consider the XPD patterns corresponding to the first preparation. Both B 1*s* and N 1*s* data exhibit similar diffraction features, with intensity maxima that are clearly visible close to grazing emission angles (fig. 3.9 a,c,e,g). These patterns present six-fold symmetry, consistent with the presence of two *h*-BN domains with opposite orientation. This point can be better understood by looking at the geometry of the *h*-BN layer on the Ir substrate, as depicted in fig. 3.10, showing the two possible orientations for a $(13 \times 13)/(12 \times 12)$ superstructure keeping the same azimuthal alignment as that of the underlying (111) surface, in agreement with the LEED findings. The domains are rotated by 180° relative to each other. Indeed, the B and N atoms positions are inverted in the corresponding unit cells. If both structures grow on the surface with the same probability and spatial distribution, then we expect the resulting diffraction pattern to be six-fold symmetric, as those obtained by the first growth procedure. In sharp contrast, the second preparation gives rise to diffraction patterns with three-fold symmetry (fig. 3.9 b,d,f,h), indicating the predominance of only one *h*-BN domain. A close comparison of the B 1*s* and N 1*s* XPD patterns shows not only their 180° misorientation, related to the non-equivalent positions of boron and nitrogen atoms in the unit cell, but also appreciable differences in the diffraction features due to different scatterers in the same structural configuration (see also fig. 3.11a and b). These results clearly indicate that the synthesis conditions affect the orientation of the *h*-BN layer. Our interpretation is further supported by the very good agreement with the simulated photoemission intensities, which have been performed considering both *h*-BN domains in fig. 3.10 (Growth 1), or just one of these (Growth 2).

So far, the emergence and coexistence of multiple *h*-BN domains has been reported on several metal surfaces. As mentioned in the introduction to this Chapter, domains without preferential orientation develop on weakly interacting substrates such as Pd [28], Cu [29] and Ag [30]. For the strongly bonded *h*-BN/Rh(111) interface, instead, the symmetry of the domains is the same as that of the substrate, although 180° misoriented islands have been reported [25]. Two antiparallel domains form on Ni(111),

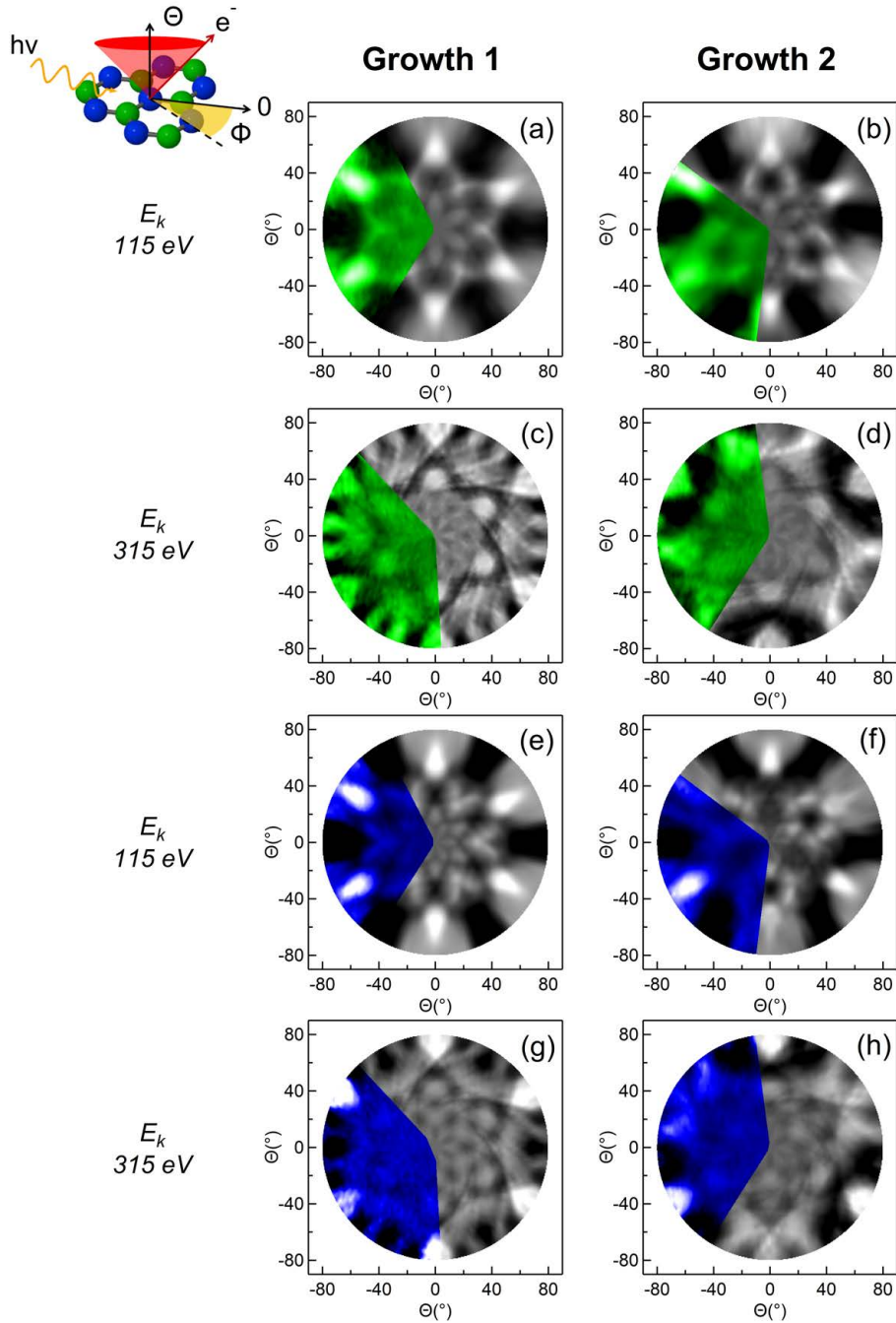


Figure 3.9: Stereographic projection of the integrated photoemission intensity modulation $I(\theta, \phi)$ as a function of emission angles (see text for details) for (a-d) the B $1s$ and (e-h) the N $1s$ core levels measured at the indicated photoelectron kinetic energies. The colored sector is the experimental data, while the grey region is the calculation for a flat, free-standing h -BN layer.

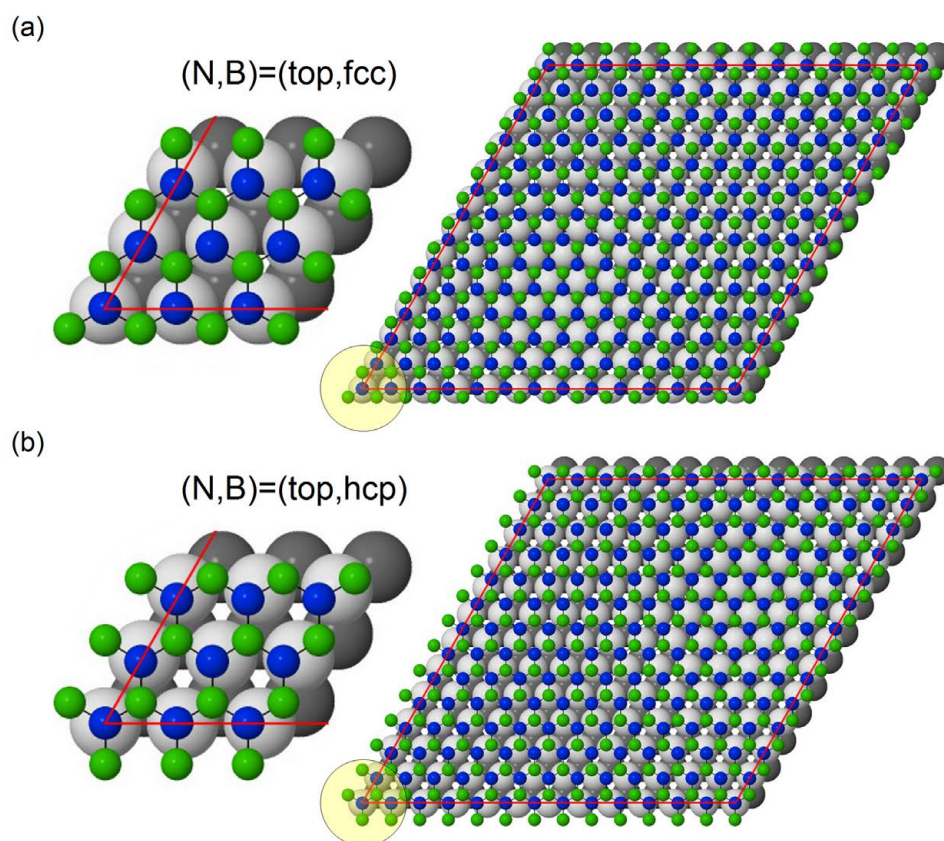


Figure 3.10: Possible $(13 \times 13)/(12 \times 12)$ configurations for *h*-BN/Ir(111). The insets on the left show a zoom-in on bonding regions of the (a) *fcc* and (b) *hcp* adsorption configuration (see text for details).

corresponding to a unit cell with N on top of Ni atoms and B on *fcc* or *hcp* sites, that is, $(N_{\text{top}}, B_{\text{fcc}})$ or $(N_{\text{top}}, B_{\text{hcp}})$ configurations, respectively [31, 57]. It has been suggested that small amounts of carbon contamination may control the ratio between these domains [31]. It is noteworthy that previous experimental findings [52, 55] and theoretical predictions [58] suggest the *h*-BN monolayer to be rather weakly chemisorbed on Ir(111). Hence, we could expect that the *h*-BN layer is not forced to adopt a preferential orientation.

The absence of carbon or other impurities was carefully checked by XPS (detection limit of 1% of a monolayer), thus, in our case, we can safely rule out the possibility proposed in Ref. [31]. What is therefore the factor that sets limits on the formation of one or both domains? A plausible scenario is that nuclei with a well-defined alignment are already established at the first stages of the growth, and that these seeds expand while keeping their initial orientation. Theoretical calculations show that for the commensu-

rate h -BN/Ni(111) interface the bonding configurations are (N_{top}, B_{hcp}) and (N_{top}, B_{fcc}) , the latter being energetically favored [9]. The situation is only slightly different for lattice-mismatched interfaces, where periodic repetitions of different coordination sites give rise to a moiré pattern. Nonetheless, the (N_{top}, B_{fcc}) configuration is predicted to be stable also for these systems, meaning that the regions where the BN network is closer to the substrate develop around this configuration [59, 60]. Accordingly, it is plausible to assume the (N_{top}, B_{fcc}) to be a bonding configuration also for the initial stages of h -BN growth on Ir(111).

Based on these considerations, we thus propose the following growth mechanism. When the surface is exposed to borazine at room temperature and then annealed, the nucleation starts in the lowest energy configuration: the small BN islands adopt a single orientation relative to the substrate, which very likely corresponds to a fcc domain. Notably, we have previously pointed out that borazine dehydrogenation is observed above 250 K (see fig. 3.5). This could therefore indicate that boron and nitrogen atoms are potentially able to couple and interact with the Ir surface atoms already at room temperature. As the growth proceeds, the islands expand without changing orientation, this process being energetically unfavorable even at 1270 K, as can be inferred from the experimental data. The one domain structure resulting from this preparation is thus a direct fingerprint of the presence, in the early stages of the precursor deposition, of nucleation seeds with the same orientation with respect to the Ir substrate. Note that, for the case of graphene, the energy barriers for islands rotation rise as the size of the islands increases [61], indeed the bonding interaction of graphene nanoislands with the Ir substrate is proportional to the ratio between the number of C atoms at the periphery and the total number of atoms in the cluster [46]. Therefore, a similar behaviour can be expected for h -BN growth. For the synthesis performed directly at high temperature, on the other hand, the thermal energy is sufficient to exceed the energy difference between the fcc and hcp adsorption configurations in the initial stages of the CVD process, especially when the islands are small. As a result, both nucleation seeds form, and two antiparallel h -BN domains develop. It is worth noting that our interpretation well compares to recent STM measurements on the h -BN/Ru(0001) nanomesh [13] – showing a parallel alignment of the islands growing within the same terrace –, although the interaction between h -BN and Ir(111) is far less strong than that on Ru(0001) [58].

In order to provide a compelling evidence that the single domain structure obtained by the second preparation has a fcc orientation, we extended the XPD measurements to the Ir $4f_{7/2}$ core level. Indeed, by exploiting the three-fold symmetry of the substrate and by comparison with the simulated intensities, these data allow to determine the orientation of the h -BN layer with respect to the Ir(111) surface. Fig. 3.11 shows the diffraction patterns for the B $1s$ (a) and N $1s$ (b) core levels (same patterns displayed in

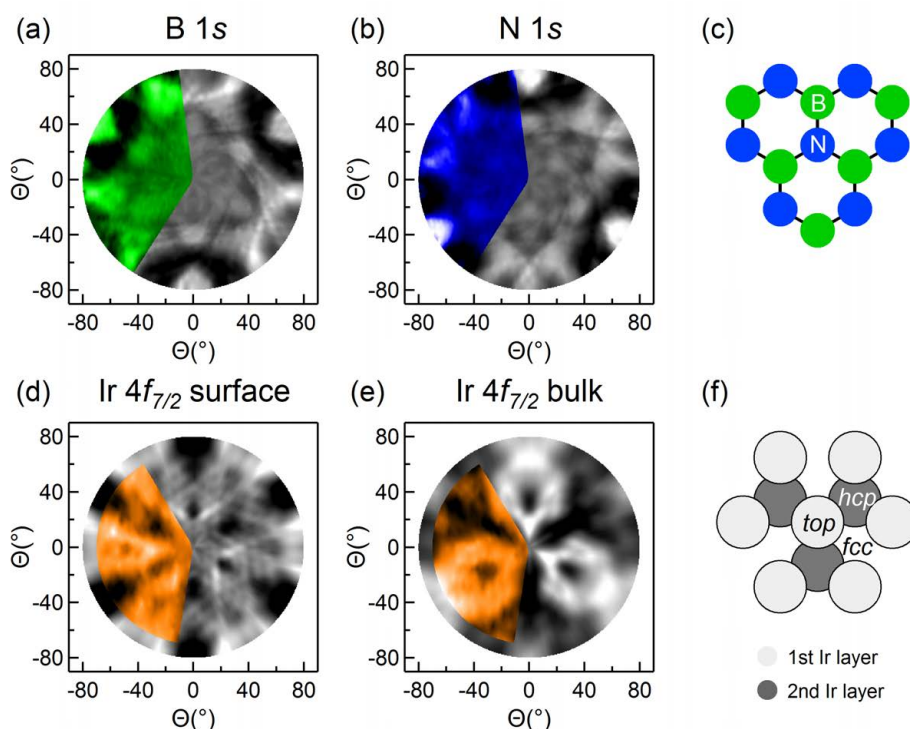


Figure 3.11: XPD patterns for B $1s$ (a) and N $1s$ (b) core levels ($E_k = 315$ eV), and Ir $4f_{7/2}$ from surface (d) and bulk (e) atoms ($E_k = 120$ eV). The geometric structures used to simulated these patterns are shown in (c) and (f) for the *h*-BN layer and the Ir(111) substrate, respectively. The simulations of the Ir patterns have been performed for the clean surface.

fig. 3.9f, h), and for the Ir $4f_{7/2}$ core level from surface (d) and bulk (e) atoms measured on the clean substrate, *i.e.* before the growth of the *h*-BN monolayer. The azimuthal orientation of the simulations is aligned correspondingly to the geometric structure shown in fig. 3.11c and f for the *h*-BN and Ir(111) lattices, respectively. Accordingly, this finding definitely proves that the absolute orientation of the B-N direction corresponds to the *fcc* configuration shown in fig. 3.10a.

In summary, in this Chapter we have presented a study of the interaction of borazine with Ir(111), from low-temperature adsorption to dissociation and synthesis of an extended *h*-BN single layer. The choice of a multi-technique approach proved to be a powerful strategy for a thorough analysis of the *h*-BN growth mechanism on Ir(111).

We exploited the high degree of directionality of π and σ bonds to show, by means of NEXAFS spectroscopy, that borazine adsorbs molecularly at

170 K with the molecule plane oriented parallel to the substrate (up to a coverage of about 0.20 ML). As shown by the TPD experiment, the annealing of the borazine-covered surface results in a continuous dehydrogenation over a wide temperature range, from 250 up to 900 K, with a maximum desorption rate at 330 K. The several components observed in the boron XPS spectra indicate that the B-N bonds crack at this temperature, leading to the formation of molecular fragments and atomic species.

The investigation of the early stages preceding the formation of the BN network allowed to shed light on the growth process, thus representing the starting point for the development of a CVD strategy alternative to the standard high temperature deposition. The XPD data presented in the last section prove that an extended *h*-BN layer with single orientation can be grown on the Ir(111) substrate by a proper control of the temperature in the first stages of the growth. Indeed, we have demonstrated that, while borazine deposition at 1070 K always lead to the formation of *fcc* and *hcp* 180° misoriented domains, cyclic borazine exposures at room temperature followed by annealing at 1270 K give rise only to the *fcc* phase. Therefore, this approach could be further exploited on other transition metal surfaces in order to improve the quality of the resulting *h*-BN films.

Bibliography

1. Dean, C. R. *et al.* Boron nitride substrates for high-quality graphene electronics. *Nature Nanotechnology* **5**, 722 (2010).
2. Dil, H. *et al.* Surface trapping of atoms and molecules with dipole rings. *Science* **319**, 1824 (2008).
3. Berner, S. *et al.* Boron nitride nanomesh: Functionality from a corrugated monolayer. *Angewandte Chemie* **119**, 5207 (2007).
4. Barth, J. V., Costantini, G. & Kern, K. Engineering atomic and molecular nanostructures at surfaces. *Nature* **437**, 671 (2005).
5. Corso, M. *et al.* Boron nitride nanomesh. *Science* **303**, 217 (2004).
6. Nagashima, A., Tejima, N., Gamou, Y., Kawai, T. & Oshima, C. Electronic structure of monolayer hexagonal boron nitride physisorbed on metal surfaces. *Physical Review Letters* **75**, 3918 (1995).
7. Preobrajenski, A., Vinogradov, A. & Mårtensson, N. Ni $3d$ -BN π hybridization at the h -BN/Ni(111) interface observed with core-level spectroscopies. *Physical Review B* **70**, 165404 (2004).
8. Auwärter, W., Kreuzt, T., Greber, T. & Osterwalder, J. XPD and STM investigation of hexagonal boron nitride on Ni(111). *Surface Science* **429**, 229 (1999).
9. Grad, G. B., Blaha, P., Schwarz, K., Auwärter, W. & Greber, T. Density functional theory investigation of the geometric and spintronic structure of h -BN/Ni(111) in view of photoemission and STM experiments. *Physical Review B* **68**, 085404 (2003).
10. Preobrajenski, A. B. *et al.* Influence of chemical interaction at the lattice-mismatched h -BN/Rh(111) and h -BN/Pt(111) interfaces on the overlayer morphology. *Physical Review B* **75**, 245412 (2007).
11. Čavar, E. *et al.* A single h -BN layer on Pt(111). *Surface Science* **602**, 1722 (2008).
12. Goriachko, A. *et al.* Self-assembly of a hexagonal boron nitride nanomesh on Ru(0001). *Langmuir* **23**, 2928 (2007).

13. Lu, J. *et al.* Step flow versus mosaic film growth in hexagonal boron nitride. *Journal of the American Chemical Society* **135**, 2368 (2013).
14. Greber, T., Brandenberger, L., Corso, M., Tamai, A. & Osterwalder, J. Single layer hexagonal boron nitride films on Ni(110). *e-Journal of Surface Science and Nanotechnology* **4**, 410 (2006).
15. Müller, F., Hübner, S. & Sachdev, H. One-dimensional structure of boron nitride on chromium (110) - a study of the growth of boron nitride by chemical vapour deposition of borazine. *Surface Science* **602**, 3467 (2008).
16. Corso, M., Greber, T. & Osterwalder, J. h-BN on Pd(110): a tunable system for self-assembled nanostructures? *Surface Science* **577**, L78 (2005).
17. Allan, M., Berner, S., Corso, M., Greber, T. & Osterwalder, J. Tunable self-assembly of one-dimensional nanostructures with orthogonal directions. *Nanoscale Research Letters* **2**, 94 (2007).
18. Chiang, C.-M., Gates, S. M. & Beach, D. B. Low-temperature adsorption and decomposition of borazine on the Si(100)-(2×1) surface. *Surface Science* **261**, 88 (1992).
19. Simonson, R. & Trenary, M. An infrared study of the adsorption of borazine, (BHNH)₃, on the Pt(111) surface. *Journal of Electron Spectroscopy and Related Phenomena* **54-55**, 717 (1990).
20. Simonson, R., Paffett, M., Jones, M. & Koel, B. A vibrational study of borazine adsorbed on Pt(111) and Au(111) surfaces. *Surface Science* **254**, 29 (1991).
21. Paffett, M., Simonson, R., Papin, P. & Paine, R. Borazine adsorption and decomposition at Pt(111) and Ru(001) surfaces. *Surface Science* **232**, 286 (1990).
22. He, J.-W. & Goodman, D. Interaction of borazine with a Re(0001) surface, studied by LEED, TDS, AES and ELS. *Surface Science* **232**, 138 (1990).
23. Jakob, P. & Menzel, D. Benzene multilayers: A model for their anisotropic growth from vibrational spectroscopy and thermal desorption. *Surface Science* **220**, 70 (1989).
24. Koel, B. E., Crowell, J. E., Mate, C. M. & Somorjai, G. A. A high-resolution electron energy loss spectroscopy study of the surface structure of benzene adsorbed on the rhodium(111) crystal face. *The Journal of Physical Chemistry* **88**, 1988 (1984).
25. Dong, G., Fourré, E. B., Tabak, F. C. & Frenken, J. W. M. How boron nitride forms a regular nanomesh on Rh(111). *Physical Review Letters* **104**, 096102 (2010).

26. Sutter, P., Lahiri, J., Albrecht, P. & Sutter, E. Chemical vapor deposition and etching of high-quality monolayer hexagonal boron nitride films. *ACS Nano* **5**, 7303 (2011).
27. Gibb, A. L. *et al.* Atomic resolution imaging of grain boundary defects in monolayer chemical vapor deposition-grown hexagonal boron nitride. *Journal of the American Chemical Society* **135**, 6758 (2013).
28. Morscher, M., Corso, M., Greber, T. & Osterwalder, J. Formation of single layer h-BN on Pd(111). *Surface Science* **600**, 3280 (2006).
29. Joshi, S. *et al.* Boron nitride on Cu(111): an electronically corrugated monolayer. *Nano Letters* **12**, 5821 (2012).
30. Müller, F. *et al.* Epitaxial growth of hexagonal boron nitride on Ag(111). *Physical Review B* **82**, 113406 (2010).
31. Auwärter, W., Muntwiler, M., Osterwalder, J. & Greber, T. Defect lines and two-domain structure of hexagonal boron nitride films on Ni(111). *Surface Science* **545**, L735 (2003).
32. Müller, F., Stöwe, K. & Sachdev, H. Symmetry versus commensurability: Epitaxial growth of hexagonal boron nitride on Pt(111) from B-trichloroborazine (CIBNH)₃. *Chemistry of Materials* **3**, 3464 (2005).
33. Auwärter, W., Suter, H. U., Sachdev, H. & Greber, T. Synthesis of one monolayer of hexagonal boron nitride on Ni(111) from B-trichloroborazine (CIBNH)₃. *Chemistry of Materials* **2**, 343 (2004).
34. Wideman, T. & Sneddon, L. G. Convenient procedures for the laboratory preparation of borazine. *Inorganic Chemistry* **34**, 1002 (1995).
35. Feulner, P. & Menzel, D. Simple ways to improve "flash desorption" measurements from single crystal surfaces. *Journal of Vacuum Science & Technology* **17**, 662 (1980).
36. García de Abajo, F. J., Van Hove, M. A. & Fadley, C. S. Multiple scattering of electrons in solids and molecules: A cluster-model approach. *Physical Review B* **63**, 075404 (2001).
37. Lee, A. F., Lambert, R. M., Goldoni, A., Baraldi, A. & Paolucci, G. On the coverage-dependent adsorption geometry of benzene adsorbed on Pd(111): a study by fast XPS and NEXAFS. *The Journal of Physical Chemistry B* **104**, 11729 (2000).
38. Chiang, T.-C., Kaindl, G. & Mandel, T. Layer-resolved shifts of photoemission and Auger spectra from physisorbed rare-gas multilayers. *Physical Review B* **33**, 695 (1986).
39. Tillborg, H., Nilsson, A., Hernnäs, B., Mårtensson, N. & Palmer, R. E. X-ray and UV photoemission studies of mono-, bi- and multilayers of physisorbed molecules: O₂ and N₂ on graphite. *Surface Science* **295**, 1 (1993).

40. Doering, J. P. *et al.* Electronic excitation and π -electron interaction in borazine. *Journal of the American Chemical Society* **108**, 3602 (1986).
41. Shen, W., Li, M., Li, Y. & Wang, S. Theoretical study of borazine and its derivatives. *Inorganica Chimica Acta* **360**, 619 (2007).
42. Bondi, A. Van der Waals volumes and radii. *The Journal of Physical Chemistry* **68**, 441 (1964).
43. Müller, F., Hüfner, S., Sachdev, H., Gsell, S. & Schreck, M. Epitaxial growth of hexagonal boron nitride monolayers by a three-step boration-oxidation-nitration process. *Physical Review B* **82**, 075405 (2010).
44. Engstrom, J. R., Tsai, W. & Weinberg, W. H. The chemisorption of hydrogen on the (111) and (110)-(1 \times 2) surfaces of iridium and platinum. *The Journal of Chemical Physics* **87**, 3104 (1987).
45. Bianchi, M. *et al.* Surface core level shifts of clean and oxygen covered Ir(111). *New Journal of Physics* **11**, 063002 (2009).
46. Lacovig, P. *et al.* Growth of dome-shaped carbon nanoislands on Ir(111): the intermediate between carbidic clusters and quasi-free-standing graphene. *Physical Review Letters* **103**, 166101 (2009).
47. Krawczyk, M. Decomposition of diborane on Pd(111): thermal and chemical behaviour of surface boron. *Applied Surface Science* **135**, 209 (1998).
48. Desrosiers, R. M., Greve, D. W. & Gellman, A. J. Decomposition of B₂H₆ on Ni(100). *Journal of Vacuum Science & Technology A* **15**, 2181 (1997).
49. Weststrate, C., Bakker, J., Gluhoi, A., Ludwig, W. & Nieuwenhuys, B. Ammonia oxidation on Ir(111): why Ir is more selective to N₂ than Pt. *Catalysis Today* **154**, 46 (2010).
50. Baraldi, A. Structure and chemical reactivity of transition metal surfaces as probed by synchrotron radiation core level photoelectron spectroscopy. *Journal of Physics: Condensed Matter* **20**, 093001 (2008).
51. Lizzit, S. & Baraldi, A. High-resolution fast X-ray photoelectron spectroscopy study of ethylene interaction with Ir(111): from chemisorption to dissociation and graphene formation. *Catalysis Today* **154**, 68 (2010).
52. Usachov, D. *et al.* Experimental and computational insight into the properties of the lattice-mismatched structures: monolayers of h-BN and graphene on Ir(111). *Physical Review B* **86**, 155151 (2012).
53. Martoccia, D. *et al.* H-BN/Ru(0001) nanomesh: A 14-on-13 superstructure with 3.5 nm periodicity. *Surface Science* **604**, L16 (2010).

54. Roth, S., Matsui, F., Greber, T. & Osterwalder, J. Chemical vapor deposition and characterization of aligned and incommensurate graphene/hexagonal boron nitride heterostack on Cu(111). *Nano Letters* **13**, 2668 (2013).
55. Preobrajenski, A. B., Nesterov, M. A., Ng, M. L., Vinogradov, A. S. & Mårtensson, N. Monolayer h-BN on lattice-mismatched metal surfaces: On the formation of the nanomesh. *Chemical Physics Letters* **446**, 119 (2007).
56. Preobrajenski, A. B. *et al.* Adsorption-induced gap states of h-BN on metal surfaces. *Physical Review B* **77**, 085421 (2008).
57. Muntwiler, M. *et al.* Determining adsorbate structures from substrate emission X-ray photoelectron diffraction. *Surface Science* **472**, 125 (2001).
58. Laskowski, R., Blaha, P. & Schwarz, K. Bonding of hexagonal BN to transition metal surfaces: An *ab initio* density functional theory study. *Physical Review B* **78**, 045409 (2008).
59. Laskowski, R., Blaha, P., Gallauner, T. & Schwarz, K. Single-layer model of the hexagonal boron nitride nanomesh on the Rh(111) surface. *Physical Review Letters* **98**, 106802 (2007).
60. Laskowski, R. & Blaha, P. *Ab initio* study of h-BN nanomeshes on Ru(001), Rh(111), and Pt(111). *Physical Review B* **81**, 075418 (2010).
61. Zhang, X., Xu, Z., Hui, L., Xin, J. & Ding, F. How the orientation of graphene is determined during chemical vapor deposition growth. *The Journal of Physical Chemistry Letters* **3**, 2822 (2012).

Chapter 4

Oxygen Intercalation Under Epitaxial Graphene on Transition Metal Surfaces

4.1 Introduction

In the last years, epitaxial growth of graphene on metallic surfaces has been actively pursued as an efficient way to synthesize graphene single-crystals with excellent quality [1, 2]. As outlined in the introduction, epitaxial graphene offers certain advantages over exfoliated graphene, especially when it comes to device fabrication, such as high-frequency and logic transistors [3], where the large area is a key requirement. Moreover, graphene single layers on metal substrates are relatively easy to prepare compared to SiC-grown monolayers which are accompanied by the growth of additional second and third carbon layers at the step edges [4]. The CVD growth of graphene has been extensively studied on a variety of metals and there are several reviews on this topic [5–7].

The interaction with the substrate is, however, a critical aspect for GR-metal interfaces. When the coupling is strong, a pronounced modification of the π -band electronic structure of graphene is observed which usually leads to a n -doped graphene and opening of a band gap. This is certainly the case for graphene on Ni(111), where the hybridization between the π -band of graphene and the d -band of the metal leads to the suppression of the Dirac cone [8, 9]. Remarkably, for GR on Cu(111), which is also a lattice-matched interface, the situation is just the opposite. Indeed, graphene-Cu(111) is a typical example of weakly interacting system [10, 11]. The different bonding of GR with Cu and Ni can be related to the filling of the corresponding d shells, resulting in a decrease of the energetic and spatial overlap (hybridization) between the metal $3d$ and graphene π states.

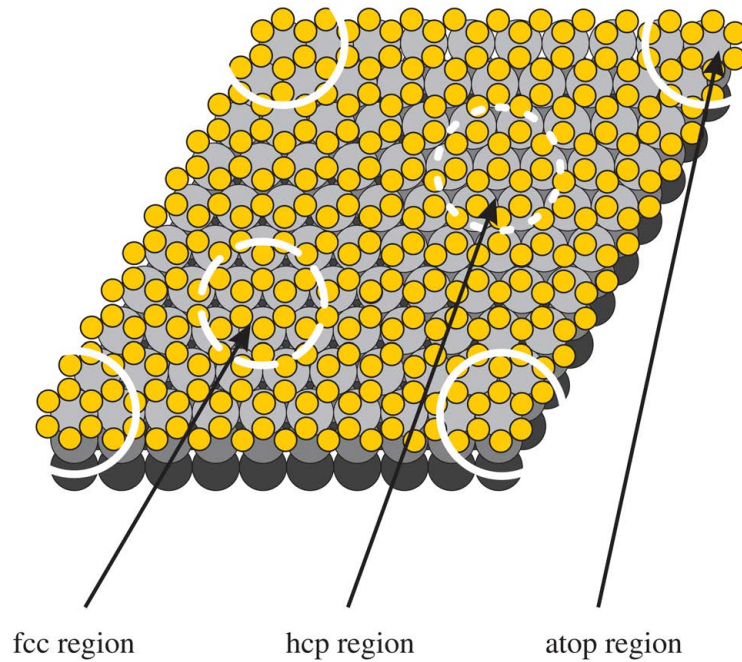


Figure 4.1: Illustration of the high-symmetry stacking configurations of the moiré unit cell formed by the superposition between the graphene lattice (yellow balls) and a *fcc*(111) surface. This particular example refers to the GR/Ir(111) interface, which shows a $10 \times 10/9 \times 9$ periodicity. Second and third Ir layers are represented by darker shades of grey. In the atop regions, indicated by the arcs in the corners of the cell, the graphene honeycomb is centered on an Ir atom of the topmost layer and the carbon atoms cover the threefold coordinated hollow sites. Dashed and dotted circles identify threefold coordinated hollow sites centered under the carbon ring: either an *fcc* or an *hcp* site, respectively. Every second carbon atom is located at the other hollow site and every second above an Ir surface atom. Adapted from Ref. [12].

The situation is slightly more complex for lattice-mismatched interfaces, where the carbon atoms are forced to occupy different adsorption sites within the moiré unit cell, and a corrugation of the graphene layer is usually observed. Indeed, the superposition between graphene and metal lattices, which usually show the same C_{3v} symmetry of the sp^2 honeycomb carbon lattice, results in the formation of either commensurate structures or incommensurate structures with large unit cells. The latter give rise to periodic repetitions of certain adsorption structures which are reminiscent of a moiré texture, and for this reason are also known as moiré structures. A typical example of incommensurate lattice, namely, GR on Ir(111), is depicted in fig. 4.1. Different high-symmetry GR-metal stacking positions can be identified. In particular, the atop region, that is, the region where

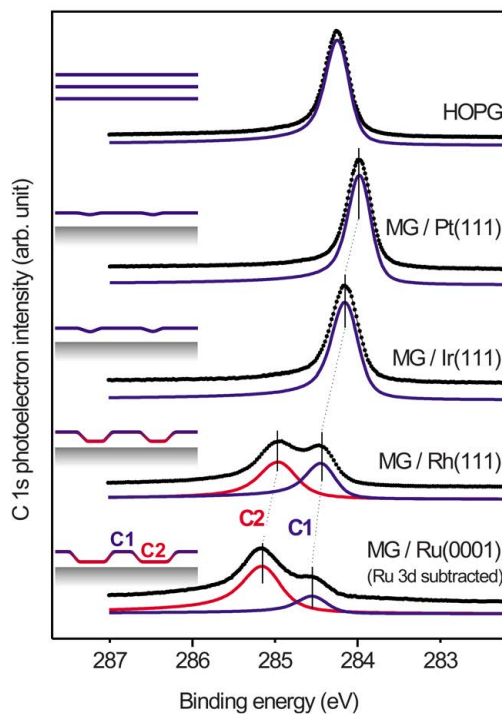


Figure 4.2: C $1s$ core level spectra of graphene on different metal surfaces measured at 400 eV photon energy. For GR/Ru(0001) the contribution of the spin-orbit splitted Ru $3d_{3/2}$ component is subtracted. The reference XPS spectrum for highly oriented pyrolytic graphite (HOPG) is also shown for comparison. Adapted from Ref. [16].

a graphene honeycomb ring is centered on a surface metal atom, shows the weakest interaction for all GR-TM interfaces. This configuration corresponds also to the largest GR-TM separation, ranging from 3.6 to 3.8 Å for Re [13], Ru [14] and Rh [15].

The different stacking geometry of the regions depicted in fig. 4.1 influences the bonding between carbon and metal atoms, giving rise to variations in the electronic structure and, therefore, to chemical shifts in the C $1s$ peak. This is the situation for graphene grown on Ru(0001) and Rh(111), where different components appear in the XPS spectra because of the strongly interacting moiré structure. This is depicted in fig. 4.2, which illustrates the results of an XPS investigation from Preobrajenski *et al.* [16] showing how the GR-TM coupling changes from weak to strong bonding in the series Pt-Ir-Rh-Ru. The increasing GR-TM interaction is reflected by a shift of the C $1s$ peak towards high binding energy and, eventually, by the development of two components [16]. A similar double-peak line shape has been observed also for the graphene/Re(0001) interface [13].

On the other hand, for weakly interacting GR-metal interfaces, graphene electronic properties are measured, with almost linearly dispersing π -band and low p - or n -doping of the graphene layer. However, for certain substrates, like Pt(111) [17], Pd(111) [18] or even Cu(111) [10], the coupling with epitaxial graphene is so weak that leads to the formation of graphene domains with different orientations and domain boundaries. It thus appears difficult to achieve a weak interaction with high structural quality at the same time.

A possible solution to this issue is the epitaxial growth of graphene on a metal substrate with a sufficiently strong interaction with graphene and the subsequent decoupling by the intercalation of metals [8, 9, 19] or silicon [20]. In this regard, the Ir(111) surface is of particular interest because it is a weakly interacting substrate – although the coupling is still sufficient to give rise to replica bands and minigaps near the Fermi level – on which high-quality graphene layers can be grown [21].

In the last years, the intercalation of atomic or molecular species through graphene has become a hot topic. This process, indeed, offers the unique opportunity to tailor the graphene-metal coupling. For graphene grown on SiC, it has been demonstrated that also atoms such as fluorine [22] or hydrogen [23] efficiently intercalate through the graphene layer. In this way, the linear π -band dispersion can be restored, at least partly, and new phenomena could be observed because of the quasi-free standing electronic structure achieved by the decoupling with hydrogen [24]. Molecular oxygen intercalation promises to play a similar role for graphene on transition metal surfaces, but so far it has been shown only for incomplete monolayers or islands [25–27].

In this Chapter we demonstrate that oxygen intercalation is possible also for a complete graphene layer, leading to an intact but quasi-free standing layer. This mechanism has been proved for epitaxial graphene grown both on a weakly, Ir(111), and a strongly, Ru(0001), interacting substrate. Moreover, we have shown that it is possible to reversibly deintercalate the oxygen. This process restores the original electronic properties of graphene on Ir(111), but it is accompanied by a moderate etching of the graphene lattice, making further intercalation processes possible at lower temperature and pressure.

4.2 Experimental Details

The Ir(111) and Ru(0001) substrates were cleaned by repeated cycles of Ar⁺ sputtering and annealings in O₂ atmosphere between 600 and 1000 K. The residual oxygen was removed by hydrogen exposure at 800 K on Ir, and by a flash final annealing up to 1500 K on Ru.

The graphene monolayer was grown on Ir(111) by doing more than 10 cycles of temperature-programmed growth, consisting in dosing ethylene at 520 K then annealing to 1470 K, followed by a prolonged annealing at high temperature with a base ethylene pressure of 1×10^{-7} mbar. This procedure ensures the growth of a complete layer of graphene that does not leave bare Ir regions [28, 29]. The completeness of the graphene layer was proved by the ratio between the intensities of the C $1s$ and Ir $4f_{7/2}$ spectra taken at normal emission at a photon energy of 400 eV, which reached saturation and did not change by prolonging the growth time. This method detects variations of the C coverage as low as 1-2%.

On the Ru(0001) surface, a graphene single layer was grown by thermal decomposition of ethylene at 1100 K. The precursor pressure was initially set at 5×10^{-9} mbar and successively increased in steps up to 5×10^{-8} mbar to ensure surface saturation. The resulting graphene layer showed the typical LEED pattern with sharp moiré spots [30].

Oxygen intercalation was achieved by placing the sample in front of a custom-made O₂ doser and maintaining the background pressure at 5×10^{-4} mbar. The doser is a molybdenum tube of 6 mm diameter, placed at less than half millimeter from the sample surface. With this setup we estimate that the pressure at the sample surface is enhanced by about one order of magnitude compared to the background pressure. The high-energy resolution XPS spectra of Ir $4f_{7/2}$, Ru $3d$ and C $1s$, and O $1s$ core levels were measured using photon energy of 130, 400, and 650 eV, respectively, with an overall energy resolution ranging from 40 to 100 meV. As described in Section 2.3.2, the core level spectra were best fitted with Doniach-Šunjić functions [31] convoluted with a Gaussian distribution, and a linear background. A Shirley background [32] was subtracted from the Ru spectra before fitting. The ARPES experiments were performed at the SGM-3 beamline of the synchrotron radiation source ASTRID (Aarhus, Denmark) with the sample temperature kept at 70 K. The photon energy was 47 eV, with a total energy and k resolution of 18 meV and 0.01 \AA^{-1} , respectively. The Dirac point was linearly extrapolated from the peak positions of Momentum Distribution Curves (MDCs) corresponding to the left and right branches of the π -band in the energy range from 0.3 to 0.6 eV below the Fermi level. This energy range was chosen to improve experimental uncertainties and to avoid fitting errors due to the minigaps and the kinks in the dispersion [33], this latter arising from electron-phonon coupling.

4.3 Graphene/Ir(111): Results and Discussion

Fig. 4.3a shows the Ir $4f_{7/2}$ spectrum of the graphene/Ir(111) interface, which is very similar to that of the clean Ir surface [34], and the C $1s$

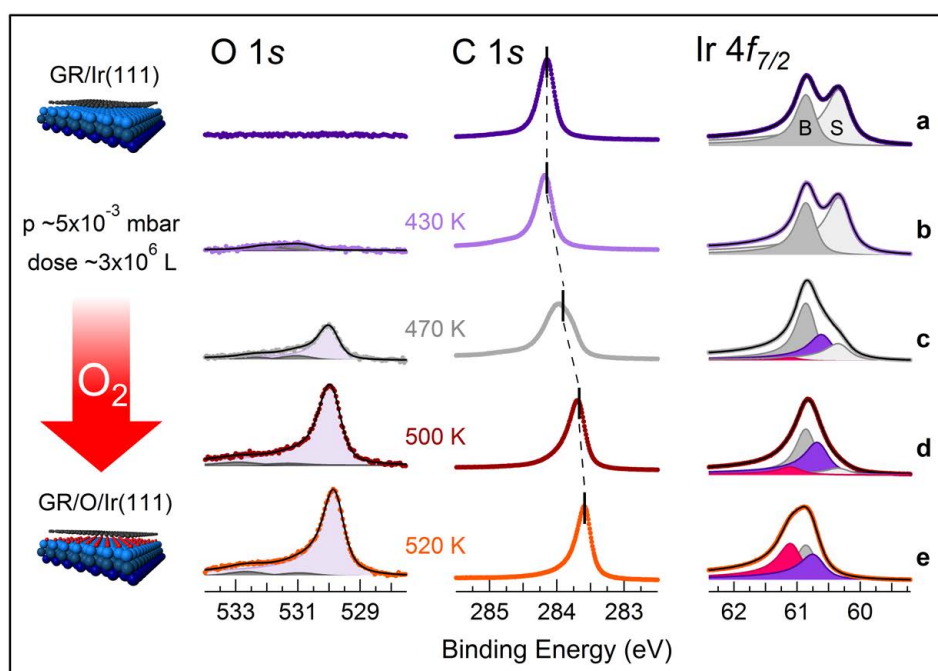


Figure 4.3: O $1s$, C $1s$ and Ir $4f_{7/2}$ core level spectra for different intercalation steps of oxygen under graphene/Ir(111). Oxygen exposures were performed with a doser at a pressure of 5×10^{-3} mbar for 10 min and at a sample temperature ranging from 430 to 520 K.

core level spectrum. Besides the bulk and surface components, no other adsorbate-induced features appear in the Ir $4f_{7/2}$ spectrum. This finding is a fingerprint of the weak GR-Ir interaction, since any small modification in the electronic structure (due to charge transfer, hybridization, *etc.*) is expected to induce a measurable SCLS [35] (see Section 2.3.1). Remarkably, this situation is quite different from the case of *h*-BN growth on Ir(111) illustrated in Chapter 3, where a new spectral component related to regions of the *h*-BN lattice strongly interacting with the Ir substrate is observed (see Section 3.3.3 for more details). The C $1s$ spectrum shows a narrow single component at 284.14 eV. In order to establish the conditions for oxygen intercalation under the graphene layer, the C $1s$, O $1s$ and Ir $4f_{7/2}$ core level spectra were measured after exposure to molecular oxygen at different substrate temperatures. Molecular oxygen exposure at room temperature did not lead to measurable changes in the core levels, thus confirming the completeness of the graphene layer.

Oxygen intercalation was achieved only by combining high sample temperature and high local pressure (achieved by using a doser, as explained in the experimental section). After an O₂ exposure of $\sim 5 \times 10^{-3}$ mbar at 430 K for 10 min, weak and broad features appear between 284.4 and 285.2 eV

in the C $1s$ spectrum and between 530.5 and 533.0 eV in the O $1s$ spectrum (fig. 4.3b). These components are related to the formation of C-O bonds in GR/Ir [36].

The lowest temperature at which some O₂ molecules effectively intercalate below graphene is 470 K (fig. 4.3c), as witnessed by the O $1s$ peak at 529.9 eV which indicates dissociative chemisorption of molecular oxygen on the Ir(111) surface [34]. The broadening of the C $1s$ peak due to the inhomogeneous perturbation of the C-Ir interaction induced by the chemisorbed oxygen, correlates with the appearance of the Ir1 component at 60.6 eV, which stems from the Ir surface atoms bound to one oxygen atom [34], and the decrease of the S component.

An efficient intercalation starts for a substrate temperature of 500 K (fig. 4.3d), while the complete decoupling of the graphene layer is achieved only at 520 K (fig. 4.3e). At this point an intense peak is measured in the O $1s$ core level at 529.8 eV, while the C $1s$ spectrum shows a narrow component at 283.6 eV, shifted by 0.54 eV with respect to the initial binding energy. The Ir $4f_{7/2}$ line shape has completely lost the S component and exhibits a new Ir2 feature at 61.08 eV, due to Ir atoms bound to two oxygen atoms [34].

It is noteworthy that molecular oxygen exposure does not lead to a variation of the intensity of the C $1s$ spectrum, that is, the graphene layer is not etched. Moreover, as illustrated in fig. 4.4a and b, we find a remarkable similarity between the Ir $4f_{7/2}$ and O $1s$ spectra measured after intercalation and those acquired on O/Ir(111), that is, in the absence of graphene. This suggests that the oxygen chemisorption occurs in a rather similar way as on the pristine Ir(111) surface, with the O atoms adsorbed predominantly in the 3-fold *fcc* hollow sites [37].

It is possible to extract quantitative information about the amount of intercalated oxygen by comparing the Ir $4f_{7/2}$ and O $1s$ spectra with those measured after the oxygen uptake on the clean Ir(111) surface at room temperature, showing a saturation coverage $\Theta = 0.38$ ML [34]. The calculated oxygen coverage is $\Theta = 0.6$ ML. This estimation is based on the finding that, as already pointed out, also in the presence of graphene the O atoms adsorb in the *fcc* sites. The larger coverage might be related to the higher oxygen pressure [37] used in this experiment as compared to 1×10^{-7} mbar of Ref. [34] or to the presence of graphene locking the O atoms close to the metal surface.

Fig. 4.4c shows the C $1s$ binding energy shift as a function of the intercalated oxygen coverage. Each experimental point was measured on a newly grown GR/Ir interface exposed to molecular oxygen at a sample temperature in the range 500-520 K for an exposure time ranging from 5 to 10 min. The curve shows that most of the C $1s$ binding energy shift is induced in the first part of the intercalation: up to $\Theta \sim 0.4$ ML, the C $1s$ shifts by 0.44 eV towards lower BE, while the subsequent increase to ~ 0.6 ML deter-

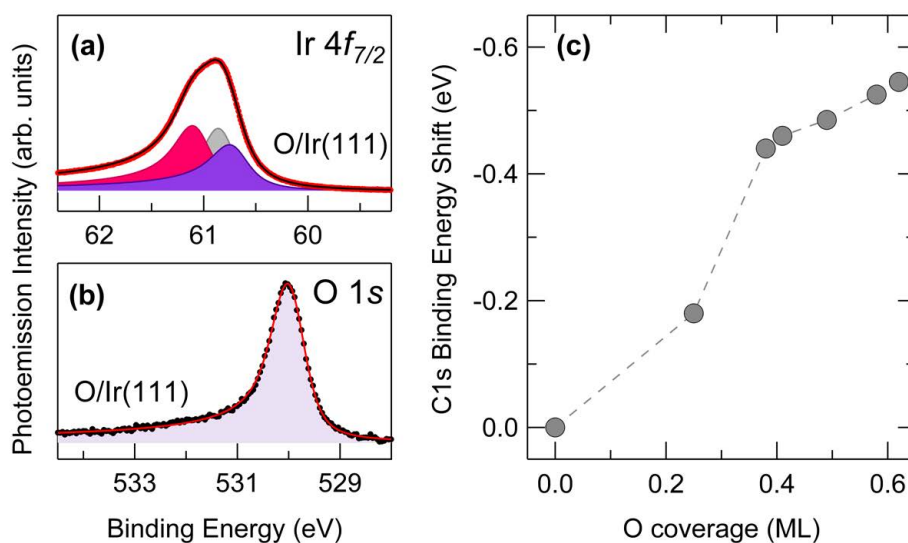


Figure 4.4: (a) Ir $4f_{7/2}$ and (b) O $1s$ spectra of the Ir(111) surface saturated with oxygen. The estimated coverage is $\theta = 0.38$ ML. (c) Binding energy shift of the C $1s$ peak maximum as a function of the oxygen coverage.

mines only an additional shift of 0.1 eV. The C $1s$ binding energy shift can be ascribed to the charge transfer from graphene to the oxygen-covered Ir surface, leading to *p*-doped graphene layer.

Most probably, the intercalation is possible only through pre-existing defective sites, such as the domain boundaries of the graphene lattice [38]. A similar mechanism has been proposed for the intercalation of Si [39] and ferromagnetic metal atoms [19] below graphene. Interestingly, the intercalation of graphene grown on SiC with Li atoms is found to deteriorate the quality of the carbon network, with the creation of cracks and vacancies [40]. We cannot exclude that also in the present case the oxygen exposure induces the formation of vacancies. This is likely to take place close to defects or wrinkles, which form in graphene/Ir(111) during cooling after the CVD growth. However, the eventual C loss during oxygen intercalation through a complete graphene layer at 520 K is below the XPS detection limit (1-2%).

Oxygen deintercalation is observed after annealing of the GR/O/Ir(111) interface to high temperature. Fig. 4.5 shows the evolution of the C $1s$ core level upon annealing from 320 to 690 K, with a heating rate of 0.5 K/s, together with the high energy resolution XPS spectra measured before and after the annealing, in the top and bottom part, respectively. The C $1s$ peak is quite stable up to 570 K and suddenly undergoes a binding energy shift, eventually recovering the binding energy position and line shape characteristic of the pristine graphene/Ir(111) interface. After the annealing, the

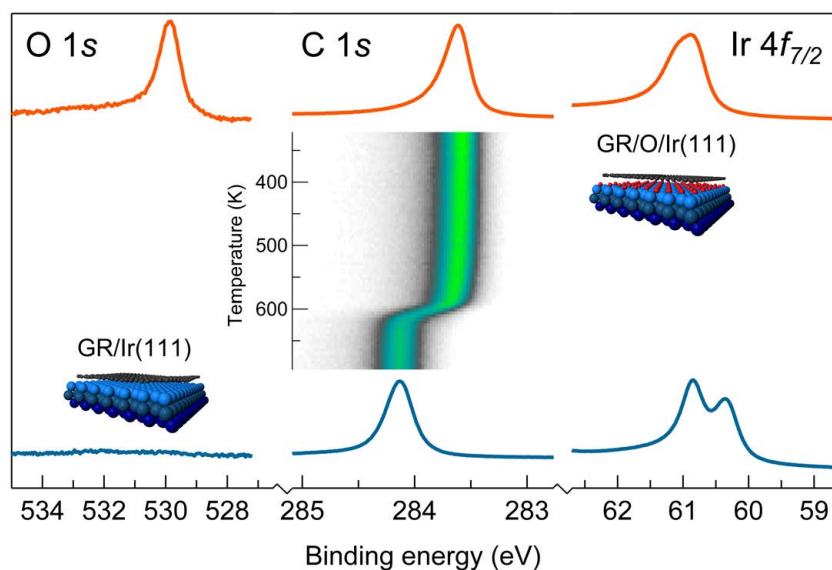


Figure 4.5: Thermal evolution of the O $1s$, C $1s$ and Ir $4f_{7/2}$ spectra measured on graphene/O/Ir(111) while ramping the temperature from 320 to 690 K at a rate of 0.5 K/s. The top and bottom spectra were measured before and after the annealing, respectively, while the central panel represents the C $1s$ intensity plot during sample heating.

Ir $4f_{7/2}$ spectrum displays the line shape typical of the graphene/Ir(111) interface, while the O $1s$ peak intensity vanishes. These findings indicate that upon annealing at about 700 K, oxygen desorbs from the Ir substrate, and the GR-Ir interaction is re-established. Oxygen deintercalation, however, leads to a decrease of the C $1s$ intensity by $\sim 18\%$, implying that such an amount of carbon is lost during the process.

The binding energy shift of the C $1s$ peak is shown in fig. 4.6 as a function of the annealing temperature. The upward shift by ~ 70 meV observed up to ~ 570 K, can be related to a decrease of the oxygen coverage from ~ 0.6 ML to ~ 0.45 ML in accordance with the results presented in fig. 4.4c. Then, at around 600 K and within ~ 50 K, the C $1s$ peak rapidly reaches the BE position typical for graphene/Ir(111), as indicated by the derivative $d(\text{BE})/dT$, revealing that a sudden oxygen deintercalation has taken place.

It is worth noting that the desorption of oxygen chemisorbed on Ir(111) takes place above 800 K [41, 42]. Consequently, the measured oxygen slow-loss below 650 K cannot be due to the recombination of adsorbed oxygen on the metal surface into O_2 . This low-rate loss is possibly due to subsurface diffusion of the chemisorbed oxygen, in accordance with early XPS studies [43, 44]. However, the simultaneous decrease of the C $1s$ intensity by a few percent might also suggest that the first 0.15 ML of oxygen is partly removed through low-rate etching events. Our interpretation about

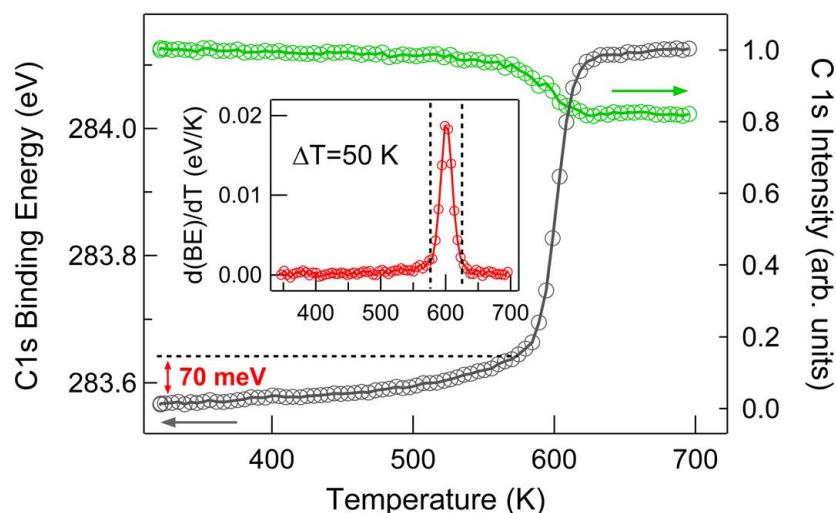


Figure 4.6: C 1s intensity (green line) and binding energy shift (grey line) *vs* temperature as determined from the evolution of the C 1s core level shown in fig. 4.5. The inset shows the first derivative of the binding energy.

the deintercalation mechanism is as follows: when the oxygen coverage reaches ~ 0.45 ML, it is no longer sufficient to keep the graphene layer detached from the Ir surface, and the interaction between graphene and Ir is locally restored in the presence of chemisorbed oxygen. At ~ 600 K, this results in the fast etching of the carbon lattice, with the eventual production of CO [27] or CO₂ which, however, are not detected by XPS because of their short lifetime on Ir(111) at 600 K [45, 46]. In the case of CO formation, the residual O amount of 0.45 ML would consume only $\sim 18\%$ of the initial C amount of ~ 2.5 ML. Moreover, the parallel production of CO₂ would further reduce the amount of carbon lost. However, the good agreement with the 18% decrease in the C 1s photoemission intensity upon O deintercalation, as shown by the green curve in fig. 4.6, points towards the predominant formation of CO.

The abrupt deintercalation suggests that the adsorbed oxygen undergoes a fast reaction from the whole surface, since the oxidation of graphene edges would proceed at a much slower rate [27, 47]. Similar fast etching processes have been observed for incomplete monolayer graphene on Ru(0001) [26, 27]. Finally, we highlight that O₂ desorption from GR/O/Ru(0001) has been reported for temperatures at which the O atoms remain bound on the pristine Ru substrate. This has been rationalized in terms of a weaker O-metal coupling induced by the presence of graphene [26]. Although the correspondence between the amount of intercalated O and C loss suggests that the oxygen consumption through formation of CO is the most likely process, the possibility that O₂ desorption is

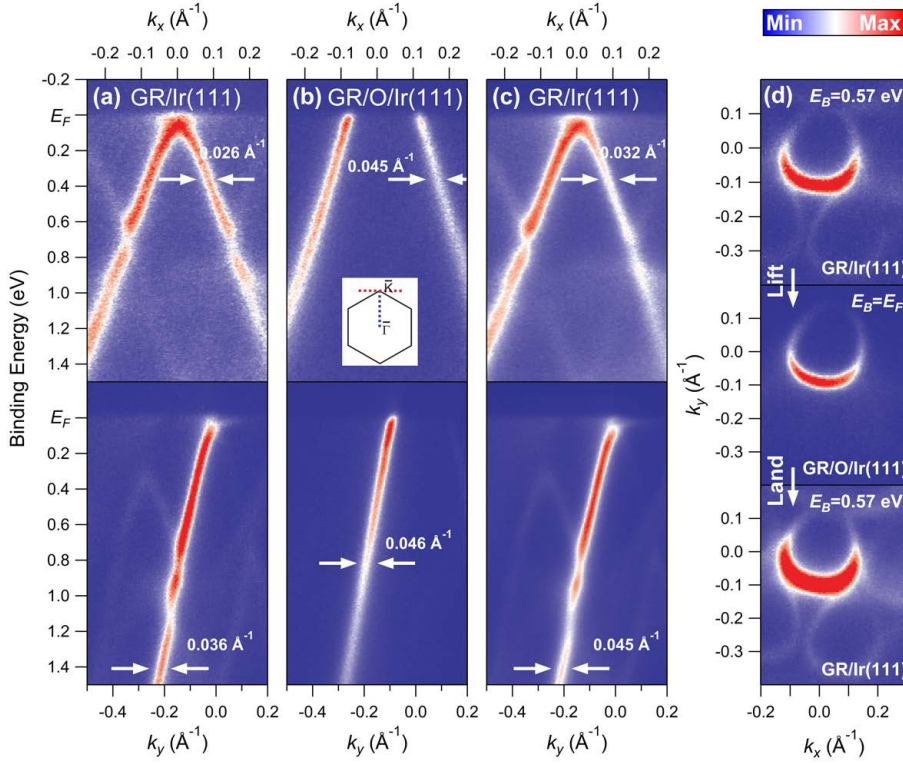


Figure 4.7: ARPES intensity maps for pristine, lifted and landed graphene on Ir(111). The spectra were acquired along a line orthogonal to the $\bar{\Gamma}K$ direction ((a–c) top panels) and along the $\bar{\Gamma}K$ direction ((a–c) bottom panels) in the Brillouin zone (see inset in (b)). The wavevector components $\mathbf{k} = (k_x, k_y)$ are measured relative to the K -point. (a) Dispersion of as-grown graphene/Ir(111), (b) lifted graphene due to O-intercalation and (c) landed graphene following O-deintercalation. (d) Constant binding energy cuts at -0.64 eV from the Dirac point for pristine, lifted, and landed graphene.

also taking place, due to the modified chemistry under the graphene cover, could be definitely ruled out only by performing thermal desorption experiments.

Angle resolved photoemission (ARPES) measurements were performed close to the K point of the graphene Brillouin zone, along a line perpendicular to the $\bar{\Gamma}K$ direction and along the $\bar{\Gamma}K$ direction (see fig. 4.7). The band structure of the pristine graphene/Ir(111) shows the narrow linearly dispersing π -band, forming the Dirac cone (fig. 4.7a). Despite the weak GR-Ir interaction, the band structure is characterized by Dirac cone replicas and minigaps resulting from the periodicity of the moiré. The typical MDC linewidth determined 0.38 eV below the Fermi level is 0.026 \AA^{-1} . The Dirac

point (E_D), *i.e.*, the crossing point between the π -band branches measured orthogonal to the $\overline{\Gamma K}$ direction, is calculated to be 0.067 eV above the Fermi energy. This means that the graphene on Ir(111) is only slightly p -doped. All these findings are consistent with previous investigations of the same system [28, 29].

A huge change of the band structure is observed directly after oxygen intercalation, fig. 4.7b. The cone replicas and the minigaps are no longer present in the π -band structure [48], which now resembles that of the hydrogen-intercalated quasi-free standing graphene on SiC [23, 49]. Moreover, oxygen intercalation results in a shift of the Dirac point to about 0.64 eV above the Fermi level, corresponding to a shift of 0.57 eV to lower binding energies compared to E_D of the as-grown graphene. This shift is interpreted as a doping effect caused by an electron transfer to the oxygen-covered Ir surface, and its magnitude is almost equal to the observed shift in the C $1s$ spectrum upon oxygen intercalation (see fig. 4.4c).

The ARPES intensity maps (fig. 4.7b) as well as the Fermi surface of the lifted graphene (fig. 4.7d central panel) show a single Dirac cone without the replica bands observed on the pristine GR/Ir(111) (fig. 4.7a and fig. 4.7d top panel). The asymmetry of the constant energy surfaces is regarded as the effect of a two-source interference phenomenon between the two graphene sublattices [50].

It can be observed that the MDC linewidth of the Dirac cone for lifted graphene measured orthogonal to the $\overline{\Gamma K}$ direction (0.045 \AA^{-1}) is larger than for the pristine graphene/Ir (0.026 \AA^{-1}) and for the hydrogen-intercalated graphene on SiC ($\approx 0.02 \text{ \AA}^{-1}$) [49] within a similar range of binding energies.

These differences can be partly ascribed to the shift towards lower binding energy of the π -band dispersion caused by the large p -doping, so that the analysis is carried out on a deeper part of the cone where the phase space for scattering is larger. Also, the structural quality of the graphene layer on Ir(111) could be poor if compared to that of graphene on SiC, thus giving rise to a shorter photohole lifetime. However, the width difference between the O-lifted GR/Ir and the H-intercalated interface on SiC could also be related to the different role of imperfectly doped areas in the two cases: on SiC, areas without H-intercalation would show the electronic structure of just the interface graphene layer on SiC. Since this interface layer does not show a Dirac cone, [51] these areas would not contribute to the observed π -band or its linewidth.

On the other hand, for the O-intercalated graphene on Ir(111), the non-uniform doped regions would still give rise to Dirac cones, but at slightly different binding energies, thus leading to an inhomogeneous broadening of its linewidth. In this picture, the different linewidth between GR/O/Ir(111) and H-intercalated GR on SiC would be related to the different role of the local doping variations and not to structural imperfections.

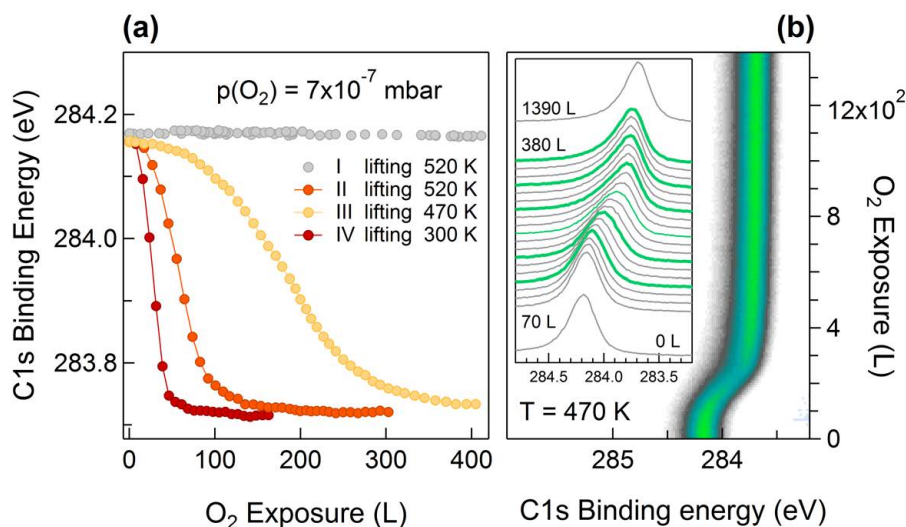


Figure 4.8: (a) C 1s binding energy measured during oxygen exposure at 7×10^{-7} mbar and different sample temperatures on the as-grown graphene/Ir(111) (I lifting) and for the graphene layer defected through previous intercalation/deintercalation cycles (II, III, and IV lifting); (b) C 1s intensity plot measured during the III lifting of defective graphene at $T = 470$ K. The inset shows the line shape evolution of the C 1s spectra.

After oxygen deintercalation, as depicted in fig. 4.7c and d (bottom panel), the band structure of the pristine GR/Ir is recovered: the replica cones and the minigaps are re-established, together with the slight p -doping. These findings are in accordance with the XPS results, and indicate that graphene is landed on the Ir substrate following oxygen removal. The only difference between the band structures of pristine and landed graphene is a small increase of the MDC linewidth. The latter reflects the increased number of defects in the carbon network, consistently with the C loss of about 18%, and the consequent reduction of the photohole lifetime.

Fig. 4.8 shows the effects of repeated intercalation/deintercalation cycles. The experimental curves correspond to the binding energy of the C 1s peak measured during the exposure to O₂ at a pressure of 7×10^{-7} mbar at the indicated sample temperatures. For the as-grown graphene no intercalation takes place, as depicted by the flat curve measured at 520 K. However, after a first intercalation at higher O₂ pressure followed by deintercalation, the second lifting performed at 520 K occurs very rapidly owing to the defects induced in the carbon network that facilitate the access of oxygen below graphene. The curve corresponding to the third lifting, performed at 470 K, highlights the effect of the temperature on the intercalation process. Indeed, despite the increased number of defects in the

graphene lattice compared to the second lifting, a lower intercalation rate is observed, which could be attributed to the reduced mobility of the oxygen atoms on Ir(111) at this temperature.

Fig. 4.8b displays the C 1s intensity plot and some selected C 1s spectra acquired during the third lifting. Beside the marked modification of the C 1s line shape, the C 1s intensity is constant throughout the O₂ exposure, indicating that the defective carbon network is not etched by oxygen. This behaviour resembles that observed during the lifting at high O₂ pressure of the as-grown graphene illustrated in fig. 4.3. The C loss in the first, second, and third landing was estimated to be around 18%, 23%, and 27% of the initial coverage of each cycle, respectively. This means that prior to the fourth lifting the initial C coverage of ~2.5 ML is reduced by more than 50% and that the graphene lattice is strongly defective. Accordingly, this lifting can be performed even at room temperature, as shown by the red curve in fig. 4.8a. It is noteworthy that while the first lifting of fig. 4.3 shows a C 1s shift of -0.54 eV, the binding energy shift for the curves in fig. 4.8a is lower, ranging from -0.44 to -0.47 eV. This result is in agreement with the lower O coverage on the Ir(111) surface reached by dosing oxygen at a pressure in the 10⁻⁷ mbar range.

Our studies show that repeated lifting and landing of the graphene by additional O intercalation/deintercalation cycles severely damage the lattice, as the C vacancies formed after each deintercalation expose more defect sites readily available and highly reactive for further etching. Moreover the C loss of about 18% in the first intercalation/deintercalation cycle is compatible with the presence of bare Ir regions, where O₂ molecules can dissociatively chemisorb and diffuse below graphene through edges and cracked defect lines, similarly to the mechanism proposed in Refs. [25] and [26] for incomplete graphene.

4.4 Graphene/Ru(0001): Results and Discussion

4.4.1 Graphene Growth

The XPS spectrum of the clean surface in the Ru 3d core level region is shown in fig. 4.9 (bottom). The Ru 3d spectrum shows the two spin-orbit splitted 3d_{5/2} and 3d_{3/2} components. As already explained in Section 2.3.1, three main contributions can be clearly distinguished in the Ru 3d_{5/2} spectrum, namely, RuB, RuS1 and RuS2, which belong to the bulk, first layer and second layer atoms, respectively. These contributions are present also in the higher binding energy Ru 3d_{3/2} peak, but they are rather broad due to a substantially shorter core-hole lifetime compared to that of the 3d_{5/2} components [52]. Also, the C 1s spectrum overlaps with that of the Ru 3d_{3/2} core level. For these reasons, a careful data analysis procedure was

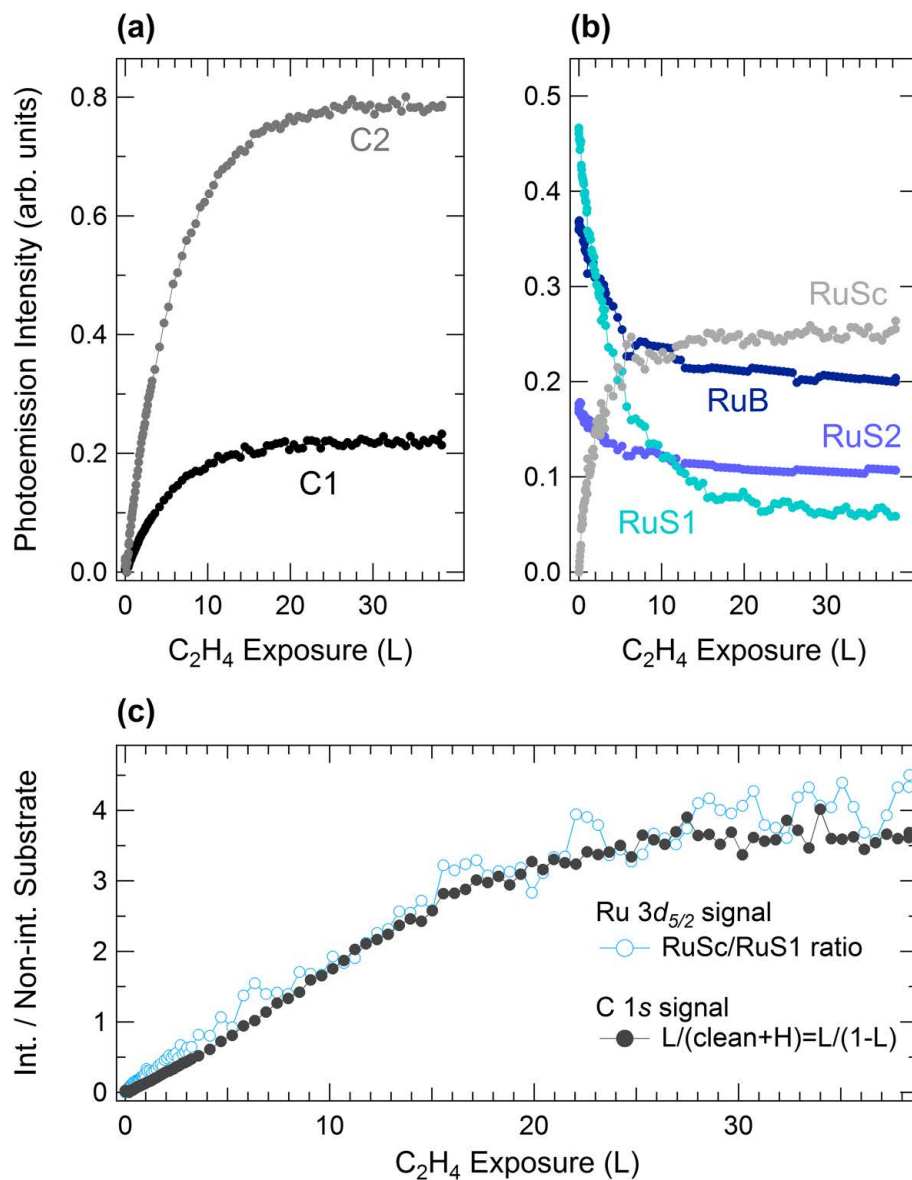


Figure 4.9: Selection of fast-XPS C $1s$ and Ru $3d$ spectra measured during graphene growth at 1100 K. Bottom and top spectra were acquired at room temperature on the clean and graphene-covered Ru surface, respectively. For these spectra the deconvolution of the spectral components obtained from the fitting procedure is also shown (see text for details).

adopted in order to fit the Ru $3d_{3/2}$ core level during graphene growth. The Ru $3d_{5/2}$ peak was first fitted with the above described spectral contributions RuS1, RuS2 and RuB, plus the additional component RuSc stemming from the Ru surface atoms interacting with graphene, as it will be discussed in the following. The intensities of the Ru $3d_{3/2}$ components were then calculated by applying the expected branching ratio of 1.5 between the areas of the spin-orbit splitted core levels Ru $3d_{5/2}/3d_{3/2}$ (see Section 2.2).

Fig. 4.9 (central spectra) displays the evolution of the C $1s$ state and the Ru $3d$ core levels during ethylene exposure at 1100 K. Initially the pressure has been kept in the 10^{-9} mbar range [53], then it has been increased in order to achieve a complete graphene layer. The high-energy resolution spectra measured at room temperature before and after graphene growth are shown in the bottom and top part of fig. 4.9, respectively.

Two components appear in the C $1s$ spectrum, C1 and C2 at 284.48 and 285.11 eV, respectively. This double-peak structure is associated to a significant corrugation of graphene [16], in accordance with previous investigations [14, 54]. The C1 spectral component is related to the high regions (H) of the moiré nanomesh [16]. Indeed, its binding energy is close the value measured for the C $1s$ peak of the weakly interacting interfaces GR/Ir(111) (284.1 eV) and GR/Pt(111) (283.9 eV), and in graphite (284.4 eV), thus suggesting a rather weak coupling with the Ru substrate. On the other hand, the high binding energy C2 peak stems from the strongly bonded parts of the GR nanomesh, which are closer to the substrate (L region) [16]. It is important to note that the outlined picture is, however, only an approximate description of graphene chemisorption. This has been recently pointed out by Alfé and co-workers, who have shown that the peculiar shape of the C $1s$ spectrum arises from a continuous distribution of non-equivalent C atomic configurations [55], leading to a broad distribution of binding energies within the moiré unit cell, rather than from two discrete regions of the graphene layer. Similar results, achieved with the same combination of XPS characterization and DFT calculations, were found for the graphene/Re(0001) interface [13].

The evolution of the photoemission intensities of C1 and C2 as a function of the ethylene exposure is illustrated in fig. 4.10a. The two components grow together with a constant ratio of 3.5 ± 0.1 throughout the whole process. This finding is in agreement with the already proposed carpet-like growth, according to which the graphene islands are expected to grow in the down-direction of the staircase of the Ru substrate steps [30, 56]. Interestingly, more recent STM measurements on graphene growth at low ethylene pressure, or high substrate temperature, highlighted a qualitatively different mechanism in which the graphene layer grows together with the underlying Ru terrace, in such a way that the graphene does not traverse the atomic step and keeps growing on the same Ru atomic plane [53]. This mechanism, which implies the transport of ruthenium to increase the ter-

race size in the downhill direction, was observed also in the uphill direction, where it consists in the etching of the step [53].

A detailed information on the interaction between the graphene layer and the substrate can be inferred from the changes observed in Ru $3d_{5/2}$ spectral components. As the ethylene exposure increases, the intensity of RuS1 is strongly reduced, whereas a new component, RuSc, grows with a CLS of -200 meV; it is straightforward to assign this spectral feature to Ru surface atoms interacting with the graphene layer. In parallel, the RuS2 component shifts by ~ 70 meV towards higher binding energy.

Remarkably, the intensity of RuS1, even though decreased, does not vanish, as illustrated in fig. 4.10b. Because RuS1 is related to the clean Ru surface, this behaviour would indicate that, although saturation is reached, the graphene layer is not complete.¹ However, this interpretation could be ruled out. Indeed, if there was bare Ru substrate, upon oxygen exposure at room temperature the uncovered areas would be immediately passivated by chemisorbed oxygen, leading to a measurable O $1s$ signal. Actually, this is not the case since no oxygen-related spectral features are detected even after O exposure up to $\sim 10^5$ L at room temperature, which definitely excludes the presence of uncovered Ru(0001) regions.

Most likely, the residual intensity of the RuS1 component corresponds to the surface atoms which are found below the elevated parts of the nanomesh, where the GR-Ru interaction is weak. Therefore, these surface regions give rise to a core level shifted component very close to that of the clean surface, similarly to what has been previously shown for the GR/Ir(111) interface (see Section 4.3). For the latter case, however, there are no H and L regions, but the whole graphene layer is weakly interacting with the substrate. According to this interpretation, we developed the following picture: the H moiré regions present a C $1s$ component at low binding energy and the corresponding Ru $3d$ peak is quite unaffected by the overlying graphene layer; in the L regions, however, the GR-Ru distance is smaller, the interaction is stronger and the C $1s$ and Ru $3d$ surface components are shifted towards higher binding energy.

Starting from this model, we tried to correlate the intensity of the surface Ru $3d$ with the C $1s$ signals during the ethylene exposure. According to the above assumption, the fraction of unperturbed Ru surface atoms consists of the sum of graphene-free areas and H regions, the L regions being the only portions of the substrate interacting with graphene. The evolution of the ratio between interacting and non-interacting regions can be expressed using the intensity of either the C $1s$ or Ru $3d_{5/2}$ surface features which, in principle, should present the same behaviour. The curves calculated following the above considerations are depicted in fig. 4.10c. More

¹Surface saturation is verified by monitoring the C $1s$ intensity in real time during C₂H₄ exposure.

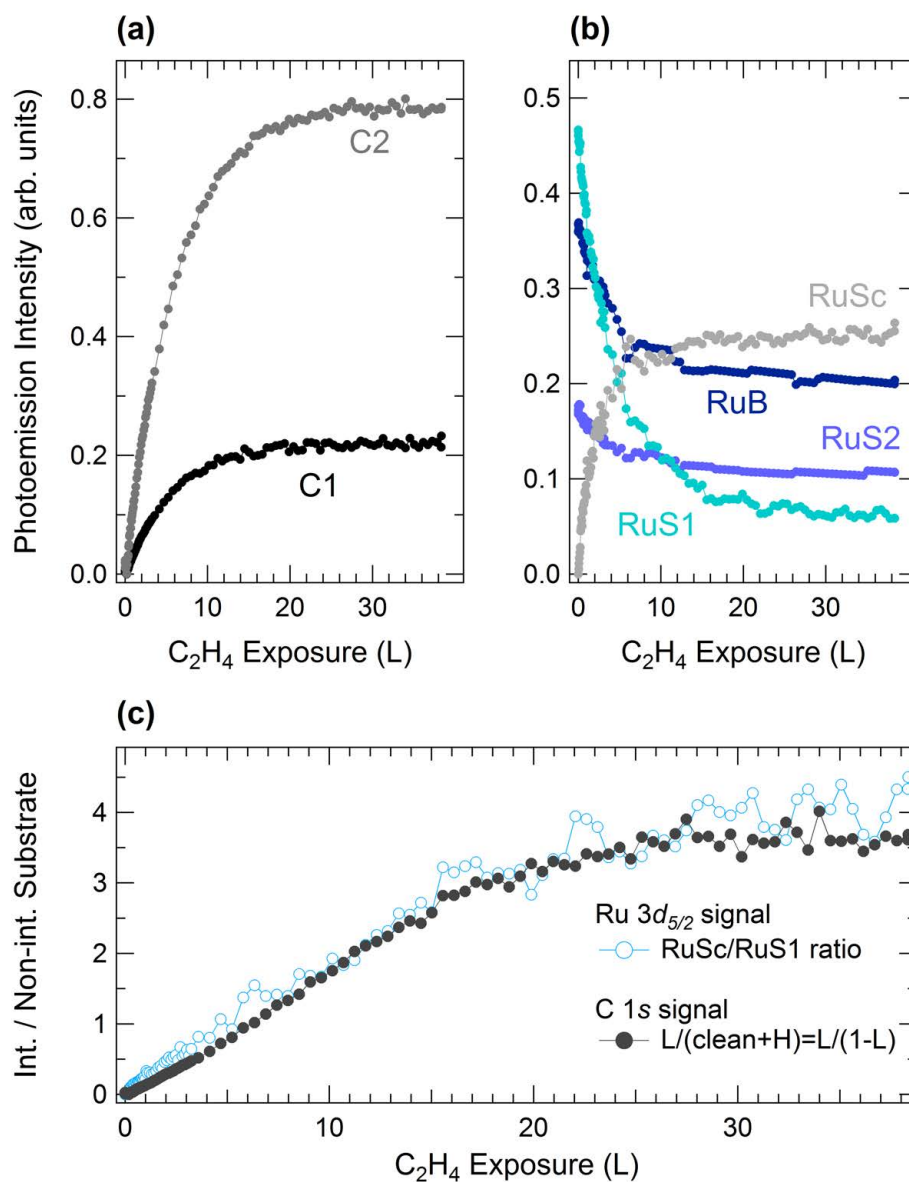


Figure 4.10: Evolution of (a) C $1s$, (b) Ru $3d_{5/2}$ and (c) ratio between interacting and non-interacting Ru surface atoms as a function of ethylene exposure during graphene growth at 1100 K. (c) Data represented with light blue open circles were obtained as the ratio between RuSc and RuS1 spectral components of the Ru $3d_{5/2}$ core level, while dark-grey filled circles have been calculated from C $1s$ spectra as $C2/(1-C2)$.

specifically, the blue open circles represent the RuSc/RuS1 ratio during ethylene exposure; the grey filled circles, on the other hand, were calculated from the carbon peaks intensities: the fraction of interacting substrate is given by the C2 intensity (normalized to the intensity of a complete graphene single layer), while the non-interacting fraction can be expressed as 1-C2, corresponding to the Ru surface atoms below graphene H regions and those still clean. The good agreement between the ratios calculated from different and independent data supports our interpretation, as can be appreciated in fig. 4.9c.

4.4.2 Oxygen Intercalation

In order to establish the intercalation conditions, the C 1s, Ru 3d and O 1s core level spectra were measured for graphene exposed to molecular oxygen at different substrate temperatures. Upon O₂ exposure at room temperature no O 1s signal was detected; only the combination of high temperature and high local pressure allowed oxygen intercalation. The same behaviour has been observed in the case of graphene/Ir(111) interface reported in Section 4.3, thus confirming the completeness of the graphene layer also for GR/Ru(0001).

At 420 K oxygen intercalates below graphene, but a full intercalation and the consequent complete decoupling is achieved at 450 K. The XPS spectra measured during a stepwise O₂ exposure of graphene at 450 K are shown in fig. 4.11, while fig. 4.12 shows the results of their analysis. After an exposure of $\sim 10^6$ L, an intense O 1s peak at 529.90 eV indicates the presence of oxygen on the sample. This is paralleled by strong modifications in the C 1s spectrum: the C1 and C2 components lose intensity, while a new feature (Clift) grows shifted by ~ 750 meV towards lower binding energy with respect to C1. As the oxygen coverage further increases, a depletion of C1 and C2 is observed, paralleled by the intensity increase of the Clift component (fig. 4.12a), which undergoes a further 100 meV shift reaching the final binding energy of 283.6 eV and a line shape narrowing (from 200 meV to ~ 100 meV), suggesting a final 'ordering' of the oxygen-lifted graphene layer (fig. 4.12b).

Effects of the oxygen exposure at 450 K can be observed also in the line shape of the Ru 3d_{5/2} core level. The RuSc component progressively disappears, indicating a gradual reduction of the Ru surface areas interacting with graphene (fig. 4.12d). In addition, two new spectral features appear at high binding energy, namely, Ru2O and Ru3O with a CLS of ~ 440 and ~ 880 meV, respectively. These components were already measured in previous investigations of the O/Ru(0001) interface, and were assigned to Ru surface atoms bound to 2 and 3 oxygen atoms, respectively [52]. The appearance of O-induced components in the Ru 3d spectrum, together with the constant C 1s intensity (see fig. 4.12a), suggests that an oxygen adlayer

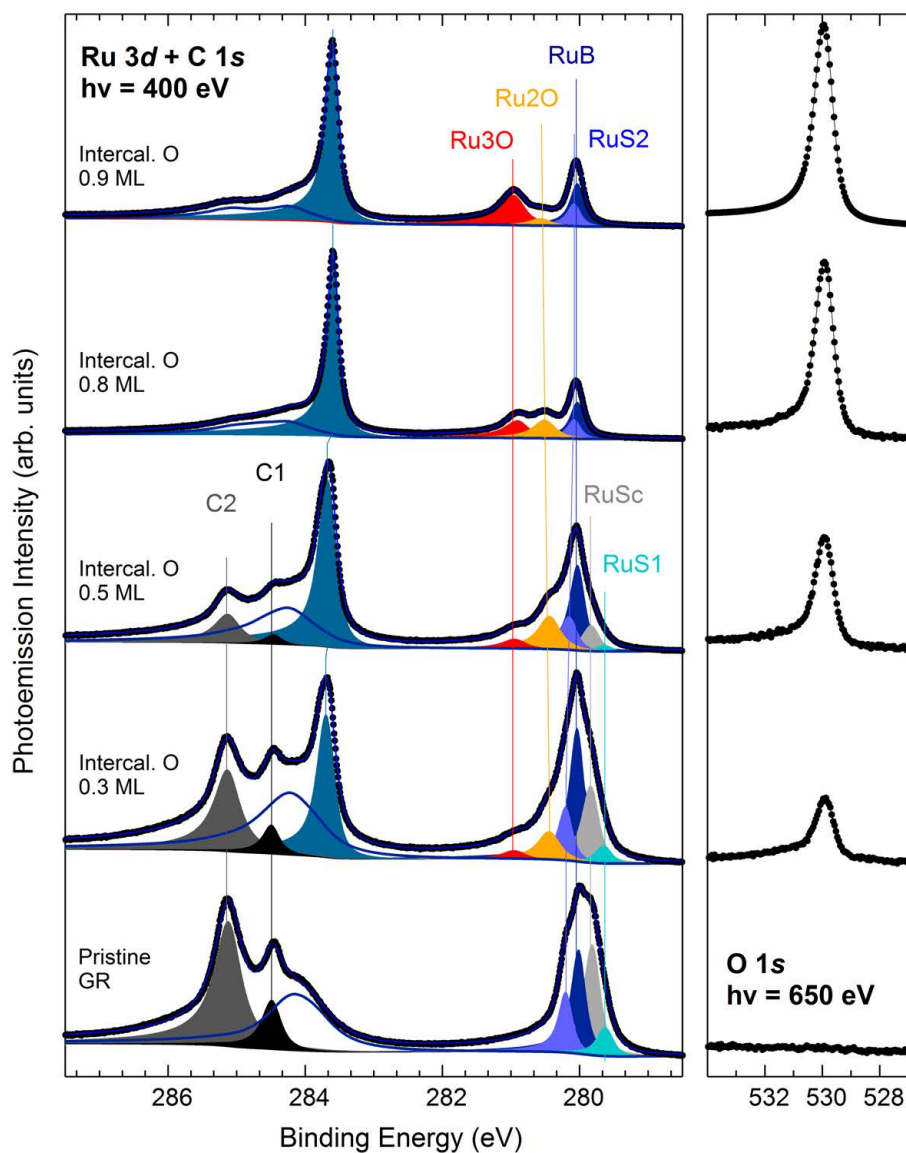


Figure 4.11: Evolution of C 1s, Ru 3d_{5/2} (left panel) and O 1s (right panel) spectral components as a function of the amount of intercalated oxygen. The O coverage of the Ru substrate was calculated from the intensity of the O 1s core level, assuming a final coverage of about 0.9 ML, estimated comparing the Ru2O and Ru3O intensities with those reported in Ref. [52].

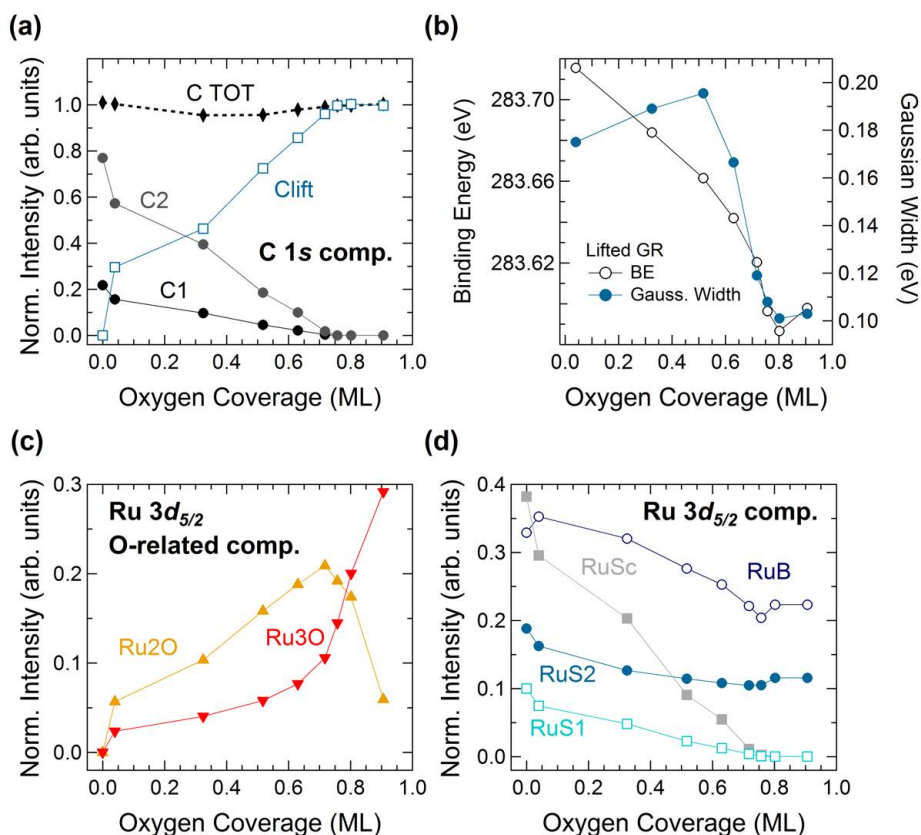


Figure 4.12: Evolution of the (a) C 1s and the (c), (d) Ru 3d_{5/2} intensity, during the stepwise O intercalation process. (b) Binding energy shift and Gaussian width of the Clift component in the C 1s core level *vs* oxygen coverage.

is forming underneath graphene, as already observed for graphene patches grown on Ru(0001) [25–27].

The strong hybridization between the Ru 4d and the graphene π states leads to the disruption of the graphene π -band [57], the opening of a gap and a pronounced downward shift of about 2 eV [26]. Indeed, as illustrated in fig. 4.13a, the ARPES measurements show no contribution of the graphene π -band close to the K point of the hexagonal Brillouin zone. The hybridization is lifted upon oxygen intercalation: linearly dispersing π -bands appear in the spectrum (fig. 4.13b), crossing at the Dirac point which is found well above the Fermi level, corresponding to a p -doped graphene layer, as is the case of the oxygen intercalated GR/Ir(111).

The reported core level evolution depicts a system where the whole carbon network is detached from the substrate because of an oxygen layer intercalated between the graphene layer and the Ru surface, the same situ-

ation described in the Section 4.3 for a complete layer epitaxially grown on Ir(111). It is worth noting that the binding energy of the C 1s component associated with the completely lifted graphene is the same (283.6 eV) on Ir and Ru. However, there is a major difference in the behaviour of the C 1s core level during oxygen intercalation for graphene grown on Ru(0001) and Ir(111). For the Ir(111) substrate a rather continuous shift towards lower binding energy is observed – paralleled by an evident broadening in the intermediate stage – and ascribed to the charge transfer from carbon to the oxygen-covered Ir substrate, leading to a *p*-doped graphene. In the case of Ru(0001), on the other hand, a new component is measured immediately after the first O₂ intercalation steps, but the characteristic peaks of the pristine GR/Ru(0001) interface, although lowered in intensity, are still detected. This finding can be rationalized by considering the different interaction of graphene with the two substrate. Because of the weak GR-Ir interaction, the main effect of the oxygen intercalation is a net charge transfer which affects the layer as a whole. In the Ru case, however, before the charge transfer could take place on the weakly interacting graphene, the strong GR-Ru chemisorption has to be weakened by the intercalated oxygen. The evolution of the C 1s core level line shape suggests that this process proceeds locally, as will be discussed in the following paragraph.

The mechanism driving the intercalation of oxygen below graphene can be identified, as in the case of Ir, in the penetration of O₂ molecules through pre-existing point defects and domain boundaries in the carbon lattice. Oxygen diffusion on the Ru surface can be reasonably expected to progress just like a water spill: the local O coverage is high close to the defects, so that the corresponding GR regions are detached and hole-doped, while it decreases at larger distance from the defects, until it is even not enough to weaken the strong GR-Ru coupling, thus leaving pristine regions as witnessed by the presence of C1 and C2 components (fig. 4.12a). Indeed, the Ru₃O and Ru₂O components start to develop already at very low coverages, where they are not present when oxygen is dosed on clean Ru(0001). In the latter case, Ru₂O and Ru₃O start are present from a coverage higher than 0.25 and 0.5 ML, respectively. Subsequent oxygen exposures result in larger areas of decoupled graphene, paralleled by a more effective hole-doping, as evidenced by the further binding energy shift undergone by the Clift component (fig. 4.12b). The described mechanism can be qualitatively applied also to the oxygen intercalation of the GR/Ir(111) interface. However, in that case, the progressive shift of the GR peak suggests a rather enhanced mobility of the oxygen atoms compared to that on GR/Ru(0001), leading to a more uniform O coverage and, consequently, to a more efficient decoupling of the graphene layer even at a low oxygen concentration. This is consistent with theoretical and experimental findings showing that graphene is more strongly bound to Ru(0001) than to Ir(111), thus making intercalation somewhat easier. In this sense, the L graphene regions on

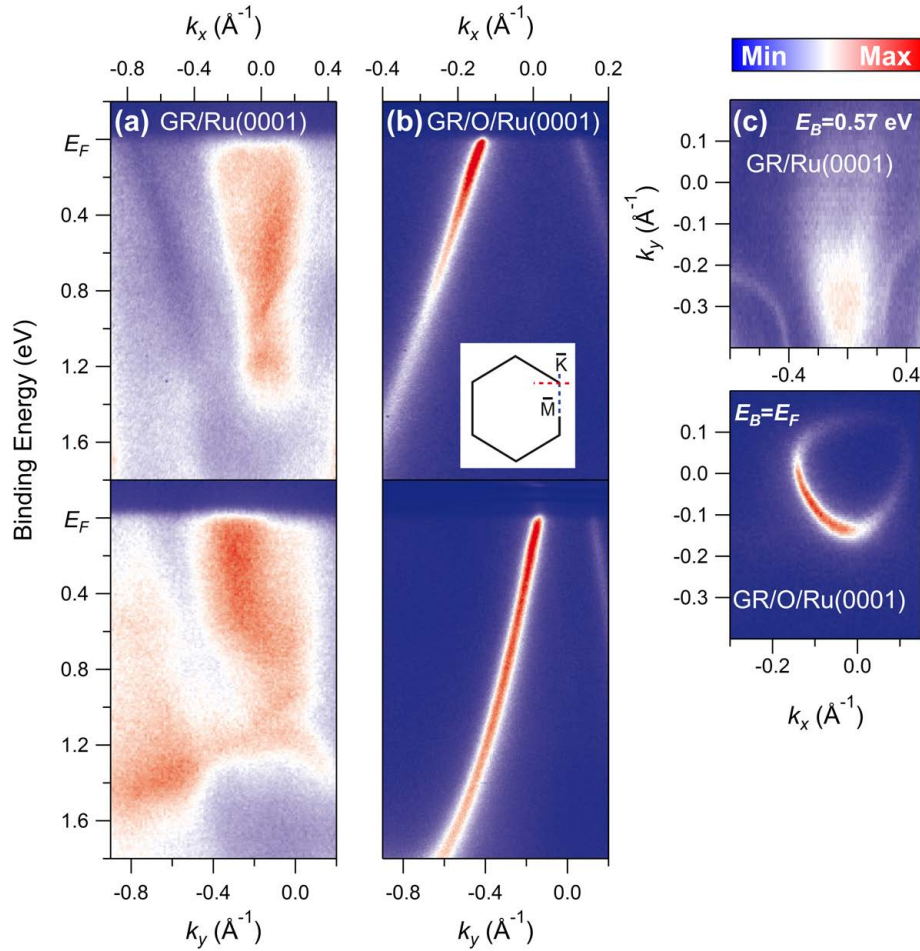


Figure 4.13: ARPES measurements of the spectral function of pristine and lifted graphene on Ru(0001). The spectra were acquired along a line orthogonal to $\overline{K}\overline{M}$ direction ((a–b) top panels) and along the $\overline{K}\overline{M}$ direction ((a–b) bottom panels) in the Brillouin zone (see inset in (b)). The wavevector components $\mathbf{k} = (k_x, k_y)$ are measured relative to the K -point. (a) Dispersion of as-grown graphene/Ru(0001) and (b) lifted graphene due to oxygen intercalation. (c) Constant binding energy cuts at the Fermi level for clean and lifted graphene.

Ru would act as ‘physical’ barriers which hinder the migration of oxygen atoms, thus resulting in a lower oxygen mobility. Furthermore, this also correlates with the observed critical amount of oxygen, 0.75 ML as illustrated in fig. 4.12a and b, above which the lifting of GR on Ru is achieved. This value is larger compared to that for GR on Ir(111), that is 0.45 ML oxygen coverage, because a higher critical coverage is probably needed to remove the stronger GR/Ru coupling.

Finally, the poor influence of the GR layer on the line shapes and binding energies of the O 1s and Ru 3d core levels is emphasized by the good agreement of these latter with those measured after oxygen uptake on a clean Ru(0001) surface [52].

In conclusion, the experimental investigation described in this Chapter demonstrates that it is possible to decouple a complete graphene layer from its metal substrate, either Ir(111) or Ru(0001), by oxygen intercalation. The proper tuning of the growth parameters allowed to find the optimum conditions to lift graphene avoiding appreciable etching of the carbon network. The lack of bare metal regions where O₂ could dissociate implies that molecular oxygen penetrates through graphene defects and dissociates on the metal surface below graphene. We cannot exclude that some defects in the lattice could be induced by the intercalation process itself. However, if so, the concentration of these defects is below our sensitivity (1%). The intercalation processes on Ru(0001) and Ir(111) show some minor differences, which are likely related to the different interaction of the two substrates with the graphene layer. Nevertheless, in both cases oxygen intercalation results in a *p*-doped, quasi-free standing graphene with a linear π -band dispersion. Abrupt oxygen deintercalation with a slight carbon etching occurs on Ir at around 600 K, leading to the recovery of the GR-Ir interaction. As a result of the deintercalation process, the damage caused to the carbon network allows for an easier oxygen intercalation. Indeed, repeated intercalation/deintercalation cycles cause further damage of the graphene layer so that it can be lifted even at room temperature and relatively low O₂ pressure. At this stage, the thermal stability of the O-intercalated GR/Ru(0001) interface has not yet been explored, but future investigations in this direction have been already planned.

Bibliography

1. Novoselov, K. S. *et al.* Electric field effect in atomically thin carbon films. *Science* **306**, 666 (2004).
2. Novoselov, K. S. *et al.* A roadmap for graphene. *Nature* **490**, 192 (2012).
3. Lin, Y.-M. *et al.* 100-GHz transistors from wafer-scale epitaxial graphene. *Science* **327**, 662 (2010).
4. Virojanadara, C., Yakimova, R., Zakharov, A. A. & Johansson, L. I. Large homogeneous mono-/bi-layer graphene on 6H-SiC(0001) and buffer layer elimination. *Journal of Physics D: Applied Physics* **43**, 374010 (2010).
5. Wintterlin, J. & Bocquet, M.-L. Graphene on metal surfaces. *Surface Science* **603**, 1841 (2009).
6. Voloshina, E. & Dedkov, Y. Graphene on metallic surfaces: problems and perspectives. *Physical Chemistry Chemical Physics* **14**, 13502 (2012).
7. Batzill, M. The surface science of graphene: Metal interfaces, CVD synthesis, nanoribbons, chemical modifications, and defects. *Surface Science Reports* **67**, 83 (2012).
8. Varykhalov, A. *et al.* Electronic and magnetic properties of quasifree-standing graphene on Ni. *Physical Review Letters* **101**, 157601 (2008).
9. Voloshina, E. N. *et al.* Structural and electronic properties of the graphene/Al/Ni(111) intercalation system. *New Journal of Physics* **13**, 113028 (2011).
10. Gao, L., Guest, J. R. & Guisinger, N. P. Epitaxial graphene on Cu(111). *Nano Letters* **10**, 3512 (2010).
11. Khomyakov, P. A. *et al.* First-principles study of the interaction and charge transfer between graphene and metals. *Physical Review B* **79**, 195425 (2009).
12. N'Diaye, A. T., Coraux, J., Plasa, T. N., Busse, C. & Michely, T. Structure of epitaxial graphene on Ir(111). *New Journal of Physics* **10**, 043033 (2008).

13. Miniussi, E. *et al.* Thermal stability of corrugated epitaxial graphene grown on Re(0001). *Physical Review Letters* **106**, 216101 (2011).
14. Moritz, W. *et al.* Structure determination of the coincidence phase of graphene on Ru(0001). *Physical Review Letters* **104**, 136102 (2010).
15. Voloshina, E. N., Dedkov, Y. S., Torbrügge, S., Thissen, A. & Fonin, M. Graphene on Rh(111): scanning tunneling and atomic force microscopy studies. *Applied Physics Letters* **100**, 241606 (2012).
16. Preobrajenski, A. B., Ng, M. L., Vinogradov, A. & Mårtensson, N. Controlling graphene corrugation on lattice-mismatched substrates. *Physical Review B* **78**, 073401 (2008).
17. Merino, P., Švec, M., Pinaridi, A. L., Otero, G. & Martín-Gago, J. A. Strain-driven moiré superstructures of epitaxial graphene on transition metal surfaces. *ACS Nano* **5**, 5627 (2011).
18. Murata, Y. *et al.* Orientation-dependent work function of graphene on Pd(111). *Applied Physics Letters* **97**, 143114 (2010).
19. Sicot, M. *et al.* Size-selected epitaxial nanoislands underneath graphene moiré on Rh(111). *ACS Nano* **6**, 151 (2012).
20. Mao, J. *et al.* Silicon layer intercalation of centimeter-scale, epitaxially grown monolayer graphene on Ru(0001). *Applied Physics Letters* **100**, 093101 (2012).
21. Coraux, J., N'Diaye, A. T., Busse, C. & Michely, T. Structural coherency of graphene on Ir(111). *Nano Letters* **8**, 565 (2008).
22. Wong, S. L. *et al.* Quasi-free-standing epitaxial graphene on SiC(0001) by fluorine intercalation from a molecular source. *ACS Nano* **5**, 7662 (2011).
23. Riedl, C., Coletti, C., Iwasaki, T., Zakharov, A. A. & Starke, U. Quasi-free-standing epitaxial graphene on SiC obtained by hydrogen intercalation. *Physical Review Letters* **103**, 246804 (2009).
24. Bostwick, A. *et al.* Observation of plasmarons in quasi-freestanding doped graphene. *Science* **328**, 999 (2010).
25. Zhang, H., Fu, Q., Cui, Y., Tan, D. & Bao, X. Growth mechanism of graphene on Ru(0001) and O₂ adsorption on the graphene/Ru(0001) surface. *The Journal of Physical Chemistry C* **113**, 8296 (2009).
26. Sutter, P., Sadowski, J. T. & Sutter, E. A. Chemistry under cover: Tuning metal-graphene interaction by reactive intercalation. *Journal of the American Chemical Society* **132**, 8175 (2010).
27. Starodub, E., Bartelt, N. C. & McCarty, K. F. Oxidation of graphene on metals. *The Journal of Physical Chemistry C* **114**, 5134 (2010).

28. Pletikosić, I. *et al.* Dirac cones and minigaps for graphene on Ir(111). *Physical Review Letters* **102**, 056808 (2009).
29. Kralj, M. *et al.* Graphene on Ir(111) characterized by angle-resolved photoemission. *Physical Review B* **84**, 075427 (2011).
30. Sutter, P., Flege, J.-I. & Sutter, E. A. Epitaxial graphene on ruthenium. *Nature Materials* **7**, 406 (2008).
31. Doniach, S. & Šunjić, M. Many-electron singularity in x-ray photoemission and x-ray line spectra from metals. *Journal of Physics C: Solid State Physics* **3**, 285 (1970).
32. Shirley, D. A. *Physical Review B* **5**, 4709 (1972).
33. Nechaev, I. A. *et al.* Hole dynamics in a two-dimensional spin-orbit coupled electron system: Theoretical and experimental study of the Au(111) surface state. *Physical Review B* **80**, 113402 (2009).
34. Bianchi, M. *et al.* Surface core level shifts of clean and oxygen covered Ir(111). *New Journal of Physics* **11**, 063002 (2009).
35. Lacovig, P. *et al.* Growth of dome-shaped carbon nanoislands on Ir(111): the intermediate between carbidic clusters and quasi-free-standing graphene. *Physical Review Letters* **103**, 166101 (2009).
36. Larciprete, R. *et al.* Dual path mechanism in the thermal reduction of graphene oxide. *Journal of the American Chemical Society* **133**, 17315 (2011).
37. Zhang, H., Soon, A., Delley, B. & Stampfl, C. Stability, structure, and electronic properties of chemisorbed oxygen and thin surface oxides on Ir(111). *Physical Review B* **78**, 045436 (2008).
38. Banhart, F., Kotakoski, J. & Krasheninnikov, A. V. Structural defects in graphene. *ACS Nano* **5**, 26 (2011).
39. Xia, C. *et al.* Si intercalation/deintercalation of graphene on 6H-SiC(0001). *Physical Review B* **85**, 045418 (2012).
40. Virojanadara, C., Zakharov, A. A., Watcharinyanon, S., Yakimova, R. & Johansson, L. I. A low-energy electron microscopy and x-ray photoemission electron microscopy study of Li intercalated into graphene on SiC(0001). *New Journal of Physics* **12**, 125015 (2010).
41. Hagen, D. I., Nieuwenhuys, B. E., Rovida, G. & Somorjai, G. A. Low-energy electron diffraction, Auger electron spectroscopy, and thermal desorption studies of chemisorbed CO and CO₂ on the (111) and stepped [6(111) × (100)] iridium surfaces. *Surface Science* **57**, 632 (1976).
42. Cornish, J. C. L. & Avery, N. R. Adsorption of N₂, O₂, N₂O and NO on Ir(111) by EELS and TPD. *Surface Science* **235**, 209 (1990).

43. Zhdan, P. A., Boreskov, G. K., Boronin, A. I., Jr., W. F. E. & Weinberg, W. H. An XPS investigation of the chemisorption of oxygen on the iridium (111) surface. *Surface Science* **61**, 25 (1976).
44. Marinova, T. S. & Kostov, K. L. Interaction of oxygen with a clean Ir(111) surface. *Surface Science* **185**, 203 (1987).
45. Lauterbach, J. *et al.* The adsorption of CO on Ir(111) investigated with FT-IRAS. *Surface Science* **350**, 32 (1996).
46. Wehner, S., Baumann, F., Ruckdeschel, M. & Küppers, J. Kinetic phase transitions in the reaction $\text{CO} + \text{O} \rightarrow \text{CO}_2$ on Ir(111) surfaces. *The Journal of Chemical Physics* **119**, 6823 (2003).
47. Cui, Y., Fu, Q., Zhang, H., Tan, D. & Bao, X. Dynamic characterization of graphene growth and etching by oxygen on Ru(0001) by photoemission electron microscopy. *The Journal of Physical Chemistry C* **113**, 20365 (2009).
48. Pletikosić, I., Kralj, M., Milun, M. & Pervan, P. Finding the bare band: Electron coupling to two phonon modes in potassium-doped graphene on Ir(111). *Physical Review B* **85**, 155447 (2012).
49. Forti, S. *et al.* Large-area homogeneous quasifree standing epitaxial graphene on SiC(0001): electronic and structural characterization. *Physical Review B* **84**, 125449 (2011).
50. Shirley, E. L., Terminello, L. J., Santoni, A. & Himpsel, F. J. Brillouin-zone-selection effects in graphite photoelectron angular distributions. *Physical Review B* **51**, 13614 (1995).
51. Emtsev, K. V., Speck, F., Seyller, T., Ley, L. & Riley, J. D. Interaction, growth, and ordering of epitaxial graphene on SiC(0001) surfaces: A comparative photoelectron spectroscopy study. *Physical Review B* **77**, 155303 (2008).
52. Lizzit, S. *et al.* Surface core-level shifts of clean and oxygen-covered Ru(0001). *Physical Review B* **63**, 205419 (2001).
53. Günther, S. *et al.* Single terrace growth of graphene on a metal surface. *Nano Letters* **11**, 1895 (2011).
54. Martoccia, D. *et al.* Graphene on Ru(0001): a 25×25 supercell. *Physical Review Letters* **101**, 126102 (2008).
55. Alfé, D. *et al.* Fine tuning of graphene-metal adhesion by surface alloying. *Scientific Reports* **3**, 2430 (2013).
56. Loginova, E., Bartelt, N. C., Feibelman, P. J. & McCarty, K. F. Factors influencing graphene growth on metal surfaces. *New Journal of Physics* **11**, 063046 (2009).

-
57. Brugger, T. *et al.* Comparison of electronic structure and template function of single-layer graphene and a hexagonal boron nitride nanomesh on Ru(0001). *Physical Review B* **79**, 045407 (2009).

Chapter 5

Placing Graphene on Insulating Substrates

5.1 Introduction

As already outlined in Chapter 1, graphene is one of the most promising materials for future electronic applications because of its very high carrier mobility, tolerance to high temperature and inertness [1, 2]. However, in order to exploit its electronic properties for technologically relevant applications, graphene has to be interfaced with insulating materials. Therefore, the realization of graphene-based devices requires, besides a well-established large-scale production method, a reliable approach to place graphene onto insulating substrates.

The first issue has been successfully tackled by the recent advances in the CVD growth on metallic substrates, which is, to date, the most promising approach towards a large-scale synthesis of graphene layers with low concentration of defects. Nevertheless, CVD growth on metal supports comes with a series of issues related to the possibility of damaging the carbon network by introducing defects during the transfer procedure from the metal to the oxide substrates. Indeed, the transfer process is usually complicated and includes a polymer cap, etching of the metal substrate and transfer of the polymer/graphene layer onto the insulating support. In order to avoid the transfer and reduce the number of processing steps, thin metal films can be used that are subsequently etched during [3] or after [4] the graphene growth. In addition, graphene can also be exfoliated directly onto a polymer support which is subsequently dissolved leaving the graphene layer on top of the desired substrate. Beside the fact that the latter procedure does not meet the scalability requirements, all the above described methods leads to the formation of defects, thicker layers and contaminants.

In order to overcome these issues, we developed a transfer-free method to electrically decouple CVD-synthesized graphene by growing an insulat-

ing layer directly underneath the carbon network. This process relies on the tendency of almost any adsorbate to intercalate below graphene [5–8], which can be exploited to promote the chemical synthesis of dielectrics underneath graphene. This route combines the advantages of high-quality large area graphene growth with an insulating substrate, opening new perspectives for device fabrication and fundamental studies of transport properties. In the first part of this Chapter, we demonstrate that a stepwise intercalation of Si and O below a graphene layer grown on the Ru(0001) surface results in the synthesis of an insulating SiO₂ layer. A similar approach is straightforwardly applied to show that the epitaxial growth of a graphene layer on a bimetallic Ni₃Al(111) alloy and its subsequent exposure to molecular oxygen results in the selective oxidation of the Al atoms and in the formation of a thick Al₂O₃ layer. The novel strategies we have adopted open the doors to the direct synthesis of a wide range of interfaces formed by graphene and high-*k* dielectrics.

5.2 Experimental Details

The cleaning procedure of the Ru crystal and the graphene growth on this substrate are described in Section 4.2. Silicon was evaporated at a rate of 0.03 ML/min by means of an electron beam evaporator, placed at around 60 mm from the sample surface that was kept at 720 K. During Si dose, fast XPS spectra of the C 1*s* and Ru 3*d*, as well as of the Si 2*p* region, were collected at a photon energy of 400 eV and 150 eV, respectively, with an energy resolution below 50 meV. After the Si dose, the sample was exposed to molecular oxygen at 640 K, through a doser in order to enhance the pressure on the sample (see Section 4.2 for details on the experimental setup). The background pressure was $\sim 4 \times 10^{-4}$ mbar. The overall oxygen dose was 2.1×10^7 L. At the end of the experiment, reference measurements of all the core levels of interest were collected. The thickness *d* of the SiO₂ layer was estimated by using the relation $I = I_0 \exp(-d/\lambda_{SiO_2})$, where the ratio I/I_0 was evaluated from the attenuation of the Ru 3*d*_{5/2} core level measured at normal emission on the graphene covered metal and on the same interface with the oxide layer. The photoelectron escape depth in the SiO₂ environment (λ_{SiO_2}) at a kinetic energy of 120 eV was taken to be 0.7 nm [9]. The resulting calculated *d* value is ~ 1.8 nm, which approximately corresponds to 7 ML of SiO₂ [10], considering that the Si atomic density in SiO₂ is 2.3×10^{22} atoms/cm³. Therefore, the amount of deposited Si corresponds to ~ 4 ML (1 ML = 1.4×10^{15} atoms/cm²).

The Ni₃Al(111) surface was cleaned by repeated cycles of Ar sputtering and annealing to 1170 K. The Al 2*p* and Ni 2*p*_{3/2} spectra were acquired with a photon energy of 230 and 950 eV, respectively. The ARPES measurements were performed at the SGM3 beamline at the ASTRID storage ring in

Aarhus (Denmark), at a photon energy of 50 eV, with an energy and k resolutions of 18 meV and 0.01 \AA^{-1} , respectively. The DFT calculations were performed with the Vienna *Ab initio* Simulation Package (VASP) code using the projector augmented wave potential and the local density approximation (LDA) exchange-correlation potential, plus a correction term to take into account van der Waals interactions. A 2×2 slab of Ni₃Al(111) containing 18 Ni and 6 Al atoms was employed to simulate the surface (for a total of 6 layers), with a vacuum region above the slab of approximately 16.5 Å. Relaxation was allowed only for the three top layers. Once the slab geometry was optimized, a graphene layer consisting of 8 atoms was placed on top of it, in various configurations (as discussed in Section 5.4) and the resulting structures were allowed to relax one more time. The same procedure was used to simulate the electronic structure of graphene on the α -Al₂O₃(001), but in this case the slab was formed by 12 Al and 18 O atoms. The core electron binding energies were calculated in the final state approximation. First, a standard calculation was performed on the fully relaxed system. An electron from the selected core level (surface and bulk electrons) was excited into the lowest conduction state, and the electronic structure was then re-calculated at fixed atomic positions. The difference between these two energies provides an estimate of the initial core level binding energy. The thickness d of the Al₂O₃ layer was estimated as in the case of SiO₂, taking into account the inelastic mean free path of the photoelectrons in alumina.

5.3 Graphene/SiO₂: Results and Discussion

The procedure used to insulate epitaxial graphene on Ru(0001) is shown in the right panel of fig. 5.1. Graphene is grown on Ru(0001) by CVD of ethylene. The GR/Ru(0001) interface is then exposed to silicon, that intercalates below the carbon network and forms a silicide with the metal substrate. Upon molecular oxygen exposure, the metal silicide is oxidized by the intercalated oxygen, resulting in an insulating SiO₂ layer that separates the metal from graphene. The thickness of the final SiO₂ layer can be adjusted by varying the amount of intercalated Si.

Fig. 5.1 shows the evolution of the C $1s$, Ru $3d$ and Si $2p$ core level spectra during the SiO₂ synthesis. The Ru $3d$ spectrum of the clean surface consists of the spin-orbit splitted components already described in detail in Section 2.3.1. The shifted component RuS1, on the low binding energy side of the bulk component RuB, is caused by the atoms in the first layer of the crystal. A component RuS2 due to Ru atoms in the second layer can also be distinguished.

The graphene layer was first grown on Ru(0001) by the standard CVD approach of hydrocarbon molecules dissociation on the hot metal

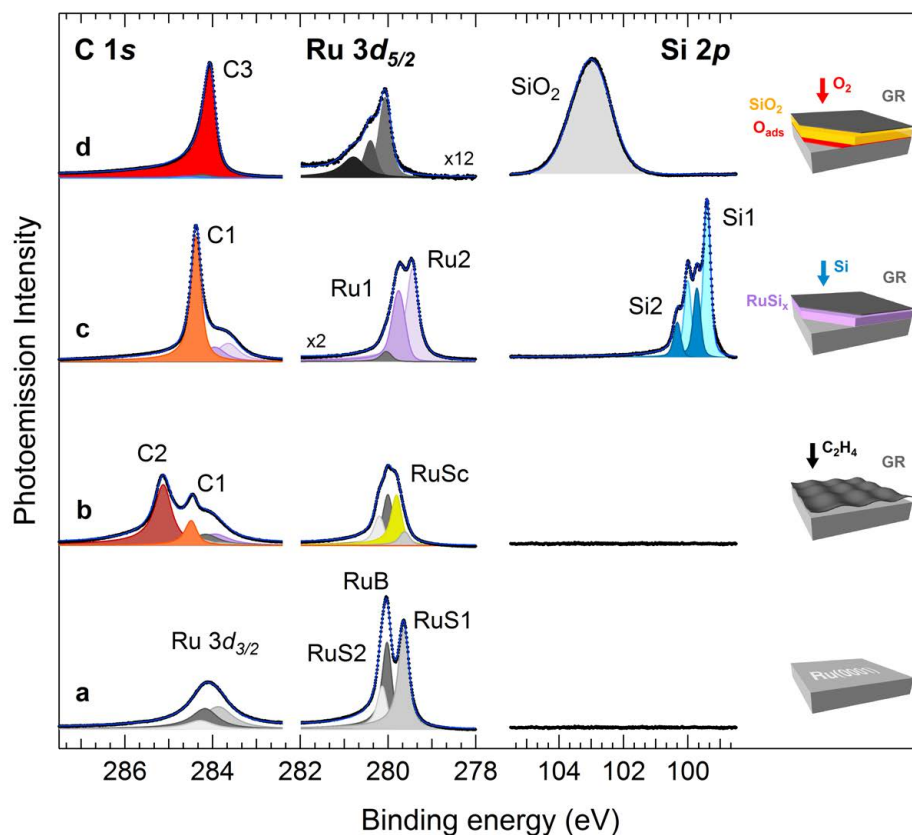


Figure 5.1: Following the synthesis of SiO_2 under epitaxial graphene on $\text{Ru}(0001)$ through XPS of the $\text{C } 1s$, $\text{Ru } 3d$ and $\text{Si } 2p$ core levels. Each process step is schematically illustrated on the right side. (a) C_2H_4 is adsorbed on a Ru single crystal surface, showing the bulk component RuB (280.01 eV) and the components due to Ru atoms in the first (RuS1 , 279.63 eV) and second (RuS2 , 280.12 eV) layers, and decomposed at high temperature, leading to (b) the formation of epitaxial graphene. One layer of graphene on $\text{Ru}(0001)$ shows two $\text{C } 1s$ peaks for carbon strongly (C2 , 285.11 eV) and weakly (C1 , 284.48 eV) interacting with the Ru surface. The $\text{Ru } 3d_{5/2}$ shows the additional RuSc component (279.81 eV) from Ru atoms strongly interacting with graphene. (c) The sample surface is exposed to Si that intercalates below the graphene and forms a Ru silicide with the metal substrate. This process gives rise to two $\text{Ru } 3d_{5/2}$ peaks (Ru1 , 279.72 eV; Ru2 , 279.41 eV), a single $\text{C } 1s$ peak C1 , and two $\text{Si } 2p$ doublets with the $3/2$ peaks at 99.40 and 99.71 eV. (d) The metal silicide is oxidized to form an insulating SiO_2 layer that separates the metal from graphene. The oxidation leads to a single $\text{C } 1s$ component (C3 , 284.04 eV) shifted in binding energy from C1 , a $\text{Ru } 3d_{5/2}$ spectrum characteristic for the oxygen-covered surface, and a broad $\text{Si } 2p$ peak characteristic for SiO_2 . The metal surface is terminated with chemisorbed oxygen.

substrate [11, 12]. As already explained in Section 4.4, the C 1s and Ru 3d_{3/2} core level fall within the same binding energetic region in the XPS spectrum, but, upon a proper deconvolution of the different contributions, a detailed information on the corrugation of the graphene layer can be inferred [13]. The C 1s spectrum shows the C1 and C2 components, stemming from regions of the graphene layer weakly and strongly interacting with the Ru atoms (see fig. 5.1). The corrugation of the graphene layer is reflected also in the appearance of an additional surface component in the Ru 3d spectrum (RuSc), due to the Ru atoms strongly interacting with graphene.

In a second step, silicon was evaporated on the metal substrate kept at 720 K [5]. Fig. 5.2 shows the evolution of the C 1s core level during Si evaporation. The spectral weight is gradually and completely transferred from the strongly interacting C2 component to the weakly interacting, narrow C1 component. As illustrated in the right panel in fig. 5.2 the total C 1s intensity remains constant during the process, indicating that all Si atoms are intercalated below graphene and do not form clusters on top of it. This is paralleled by the growth of two new features Ru1 and Ru2 in the Ru 3d_{5/2} core level at the expense of the RuS1 and RuS2 components, characteristic of the Ru-graphene interface (see fig. 5.1c). This behaviour clearly indicates the formation of Ru silicide [14, 15]. Moreover, the low intensity of the RuB peak suggests that the silicide formation extends over several layers.

In accordance with these results, the spin-orbit split Si 2p core level measured after Si intercalation exhibits two doublet components, Si1 and Si2, due to the formation of Ru-Si bonds. Fig. 5.3 shows some selected fast XPS spectra of the Si 2p core level collected during Si dose. The deconvolution of the spectral line shape highlights the formation of several phases with increasing Si coverage. The left panel and the right image in fig. 5.3 show the Si photoemission intensity for the different Si phases and the 2D plot of the Si 2p intensity evolution as a function of the Si deposition time, respectively. After the deposition of ~4 ML of Si, only the two silicides phases, Si1 and Si2, are present. By adjusting the Si deposition time, the total quantity of intercalated silicon atoms can be varied.

After the Si dose, the sample surface was exposed to molecular oxygen at a pressure of $\sim 4 \times 10^{-3}$ mbar and a temperature of 640 K (fig. 5.1d). This results in the intercalation of the molecular oxygen below graphene [7, 16], in the same way as it occurs for the graphene intercalation with oxygen on Ir(111) and Ru(0001) illustrated in Chapter 4, and in the progressive oxidation of the silicide.

The gradual oxidation of the ruthenium silicide is illustrated in fig. 5.4. The Si1 and Si2 peaks transform into a broad peak at 103.3 eV, indicating the consumption of the silicide layer and the formation of SiO₂. This is paralleled by the appearance of a O 1s peak at 532.4 eV. The evolution of both the Si 2p and the O 1s spectra indicate that no intermediate oxide phases are formed during this process.

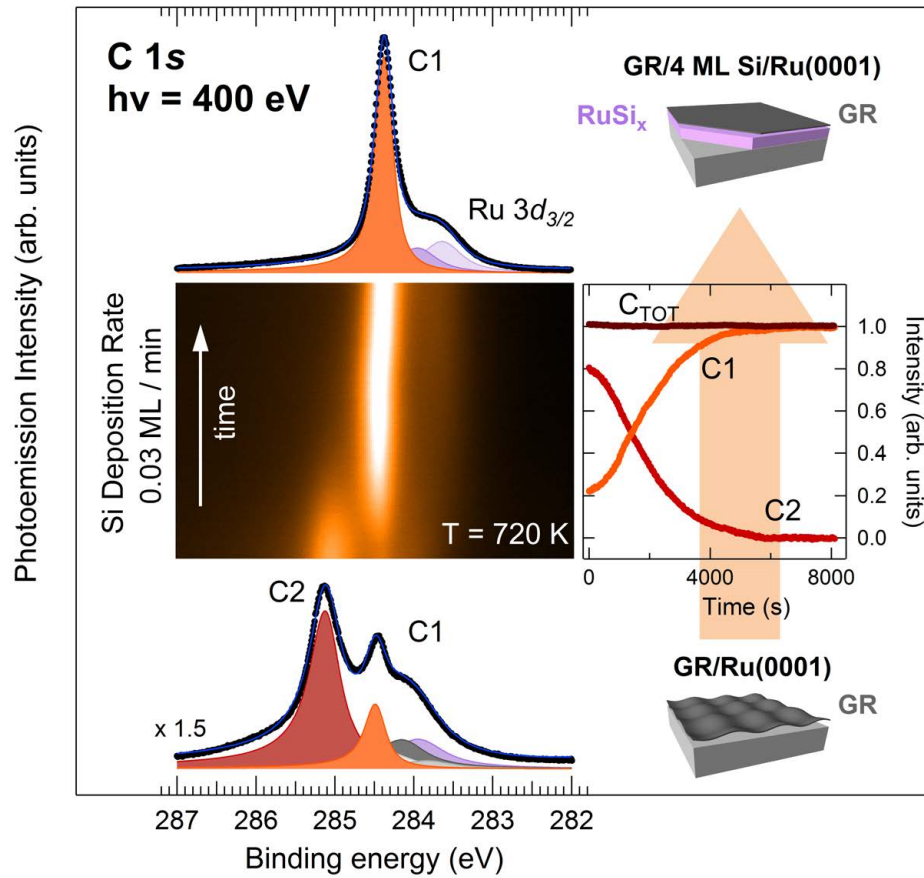


Figure 5.2: Following the Si evaporation on the GR/Ru(0001) interface at 720 K through XPS of the C 1s core level. Bottom and top spectra show the C 1s core level measured before and after Si evaporation, respectively. The central inset displays the fast XPS spectra measured during Si evaporation, showing the decay of C2 and the rise of C1 components. The right panel shows the evolution of the C 1s components as well as the sum of their intensity that remains constant in the intercalation process.

It is noteworthy that the SiO₂ layer is formed at a constant rate which is higher than that measured for the dry oxidation of the Si(001) surface with comparable temperature and O₂ pressure [17]. This rate-enhanced SiO₂ growth is an intrinsic advantage offered by the oxidation of the intermediate Ru silicide formed during the Si intercalation. In the Ru 3d_{5/2} spectrum the silicide components Ru1 and Ru2 decrease and the bulk component B recovers intensity (fig. 5.4). Moreover, in the C 1s spectrum, the C1 component transforms into the new C3 spectral feature, attributed to graphene lying on SiO₂. Neither the Ru 3d_{5/2} nor the C 1s spectra show any sign

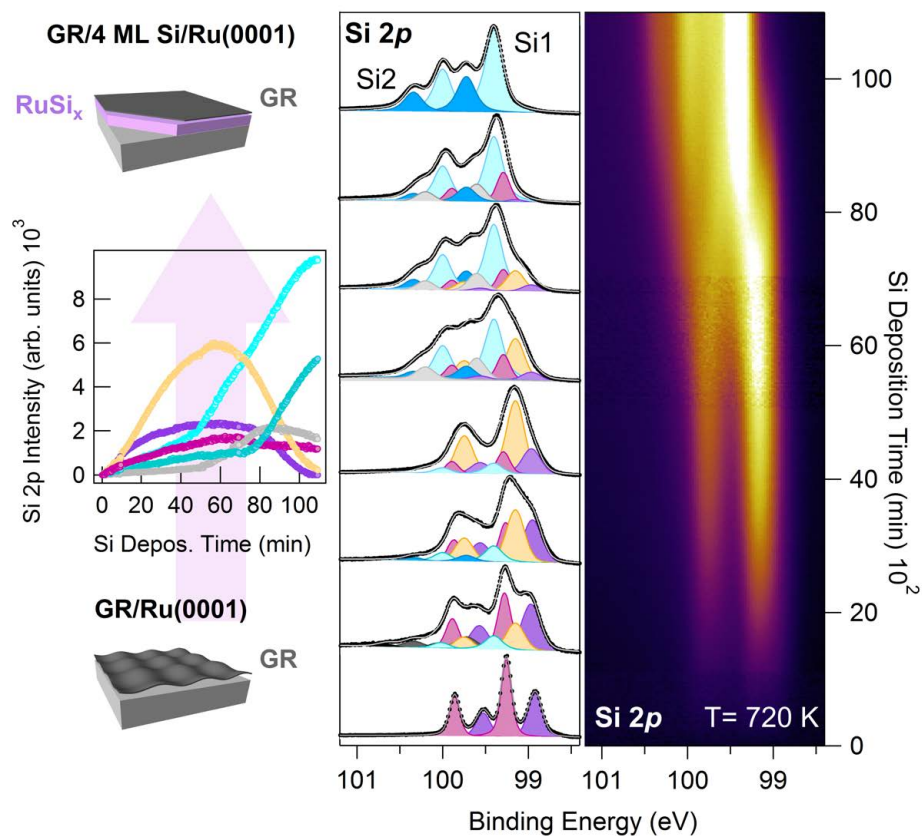


Figure 5.3: Following the Si evaporation of the GR/Ru(0001) interface at 720 K through XPS of the Si 2*p* core level. The central panel shows the evolution of the Si 2*p* line shape during the evaporation: several phases appear in the spectra with increasing Si coverage. After the intercalation of 4 ML of Si, only two silicides phases Si1 and Si2 are left. The left panel illustrates the time evolution of the intensity of the different Si phases, while the right image displays the 2D intensity plot of the fast XPS spectra measured during Si evaporation.

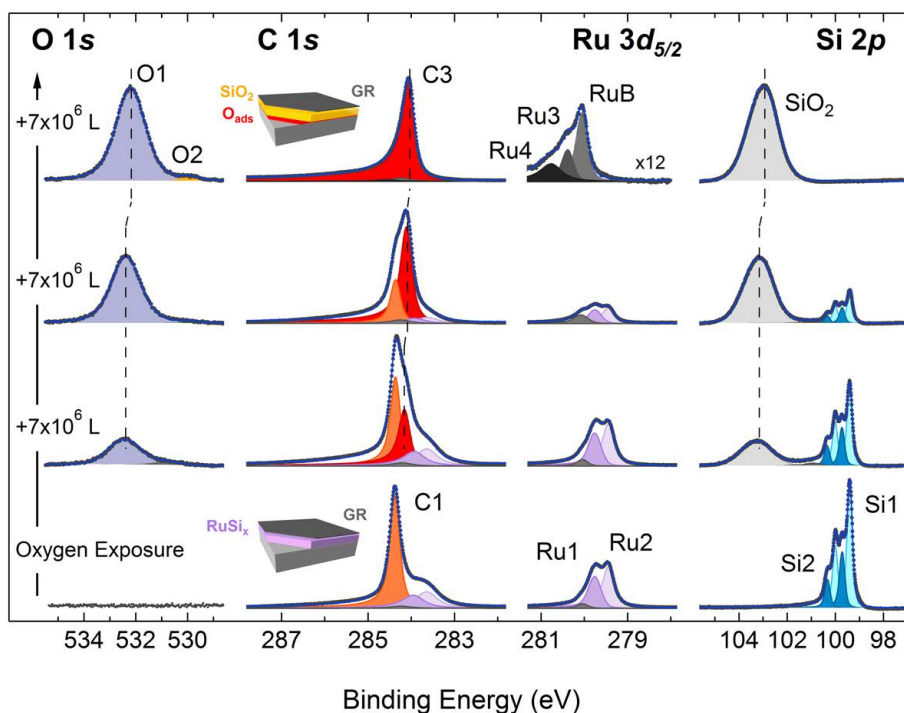


Figure 5.4: Oxidation of the Si intercalated GR/Ru(0001) interface. O 1s, C 1s, Ru 3d_{5/2} and Si 2p XPS spectra measured before and after exposing the sample to consecutive doses of 7×10^6 L of molecular oxygen at 640 K. Before oxidation the bottom Si 2p spectrum shows two doublets Si1 and Si2 due to Ru-Si bonds in the silicide phase. During oxidation the silicide decomposes and oxygen binds exclusively to Si inducing the SiO₂ component in the Si 2p and O1 component in O 1s core level spectra. During the last oxidation step, oxygen diffuses to the Ru-SiO₂ interface and chemisorbs on the metal forming the (2 × 2)-3O surface structure indicated by the Ru3 and Ru4 components, as well as by the small O2 component in the O 1s spectra.

of oxidation, demonstrating that the carbon network is not etched by the oxygen during intercalation and that during the Ru silicide decomposition the oxygen binds exclusively to Si [18, 19].

In the final oxidation step (top spectra in fig. 5.4), the Ru silicide is fully transformed into metallic Ru and SiO₂, and the C 1s region shows only the C3 component, in accordance with the fact that now all the graphene layer is supported on SiO₂. This process is accompanied by the diffusion of oxygen atoms at the Ru-SiO₂ interface [20], where they chemisorb forming a (2×2)-3O surface structure, as witnessed by the appearance of the two up-shifted Ru3 (280.35 eV) and Ru4 (280.72 eV) components in the top Ru 3d_{5/2} spectrum [21] and by the small O2 component at 529.8 eV in the O 1s spectrum. The shift towards lower binding energy by about 250 meV of both the SiO₂ peaks and the C3 component can be related to a different band alignment at the oxide interfaces with the Ru silicide and with the oxygen-terminated Ru metal [22]. As long as the thickness of the SiO₂ layer increases, the Ru 3d intensity progressively diminishes because of the inelastic scattering of the photoelectrons as they pass through the oxide film.

At this point, the graphene is separated from the Ru crystal surface by ~1.8 nm of SiO₂ (this value is calculated according to the procedure described in Section 5.2), which in principle should provide the electrical insulation of the graphene layer. In order to prove this, we performed lateral transport measurements on the surface, using a microscopic, commercial 12 point probe shown in fig. 5.5 (top).¹ The expected resistances measured with an equidistant four point probe for a semi-infinite 2D and 3D samples are $R_{2D} = \ln 2 / \pi \sigma_s$ and $R_{3D} = 1 / 2\pi s \sigma_b$, respectively, where σ_s is the surface conductivity, σ_b is the bulk conductivity and s is the distance between the contacts. The 2D graphene and the 3D metal can be viewed as parallel resistors, therefore graphene-dominated transport can be achieved only for a sufficiently small value of the contact spacing s , allowing $R_{2D} \ll R_{3D}$. However, this is not possible if the graphene layer is placed on a metal surface (unless the mechanical contact is made only to the graphene and not to the metal) since the required contact spacing would be unachievably small, of the order of the atomic spacing [23]. This also explains why the realization of graphene electronics on a metal substrate is not feasible.

Fig. 5.5 shows the measured resistance on the SiO₂-intercalated graphene on the Ru surface as a function of the contact spacing. More specifically, the figure shows the corrected resistance $\chi_{2D} R_{comb}$ as a function of the corrected spacing s_{eff} / χ_{2D} . This geometric correction allows to plot the data measured with unequal contact spacings as if they were measured with equidistant contacts, as explained in detail in Ref. [24].

¹www.capres.com

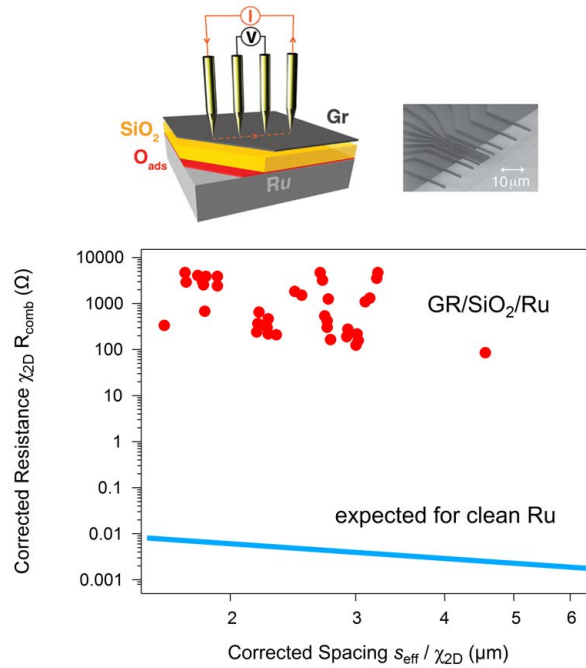


Figure 5.5: Surface resistance measurements of the resulting GR/SiO₂/Ru(0001) system using a micro four point probe. Shown is the corrected resistance $\chi_{2D}R_{comb}$ as a function of corrected spacing (s_{eff}/χ_{2D}). This essentially corresponds to the resistance as a function of contact spacing for a conventional four point probe measurement with four equidistant contacts, but the definition of $\chi_{2D}R_{comb}$ and s_{eff}/χ_{2D} permits measurements with nonequidistant contact spacings to be included in the plot. The blue line is the result that would be expected from a clean Ru surface or for a graphene layer on clean Ru. The top inset shows a simple sketch of the measurement setup as well as a picture of the type of probe used for this experiment.

As can be clearly seen in fig. 5.5, the resistance is almost independent of the distance between the contacts, thus suggesting that the transport is two-dimensional. In this regard, the spread observed in the data points can be attributed to a nonuniformity of the SiO₂ layer. The absolute value of the resistance has the same order of magnitude measured for epitaxial graphene on SiC [25] and exfoliated graphene on SiO₂ [26, 27]. Moreover, this is about 5 orders of magnitude higher than the value one would expect to measure on the clean Ru(0001) surface in this region of contact spacing, as indicated by the blue line. This definitely proves that the transport takes place on graphene, and is not dominated by the underlying substrate. Indeed, from one side the resistance of the clean surface would be too small to be detected. On the other hand, the clean SiO₂ has a resistivity that is 23 orders of magnitude higher than that of a good metal, making a measurable contact impossible in this case as well.

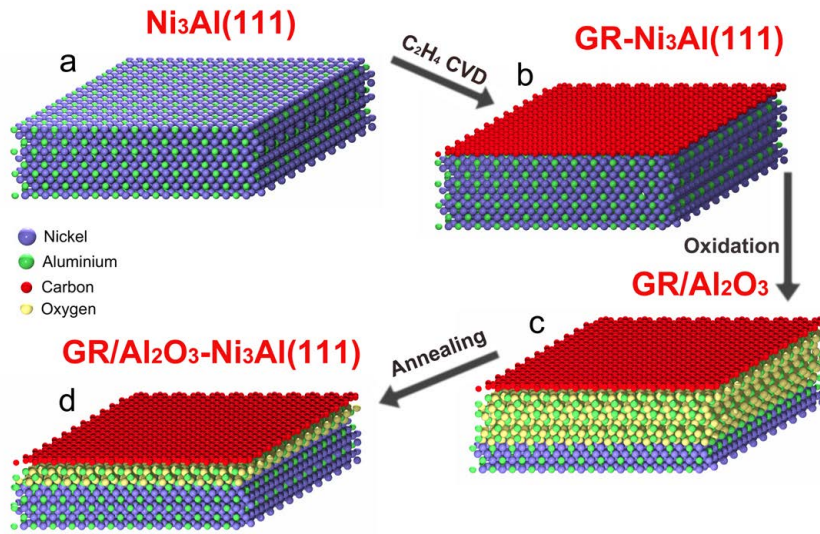


Figure 5.6: Schematic illustration of the three-step process for the synthesis of a thin Al_2O_3 film under epitaxial graphene on $\text{Ni}_3\text{Al}(111)$. (a) C_2H_4 exposure of Ni_3Al at high temperature leads to (b) the formation of epitaxial graphene. (c) The GR/alloy interface is then exposed to molecular oxygen that intercalates underneath graphene and selectively oxidize the Al atoms, resulting in an amorphous Al_2O_3 layer. (d) Annealing to high temperature leads to an ordered thin film.

The demonstrated process can be exploited even further to promote the chemical synthesis of other materials below graphene. Indeed, a similar approach has been used for the synthesis of an aluminum oxide layer, as described in the following section.

5.4 Graphene/ Al_2O_3 : Results and Discussion

Fig. 5.6 depicts a schematic of the procedure used to insulate a epitaxially grown graphene on a $\text{Ni}_3\text{Al}(111)$ surface by selective oxidation of the Al atom, leading to a thick Al_2O_3 dielectric layer. The first step consists in the graphene growth on the $\text{Ni}_3\text{Al}(111)$ alloy surface using the same approach already employed for the growth on transition metals, that is, via CVD deposition of ethylene at high temperature. In this case, however, particular attention was paid in order to avoid carbon diffusion into the bulk at high temperature, a problem which commonly affects the growth of graphene on Ni surfaces above 970 K [28]. Moreover, if the growth is performed at lower temperature, below 700-720 K, Ni exhibits a carbide phase [29]. On the other hand, a high temperature is usually required to provide the carbon atoms with sufficiently high mobility to let them rearrange into a highly ordered honeycomb structure. Given this, the sample

temperature during the ethylene uptake was fixed to 950 K, which almost corresponds to the upper limit at which the best graphene quality can be achieved on Ni [28, 30]. In addition, we also used a relatively high C_2H_4 pressure (2×10^{-6} mbar) to ensure the nucleation of graphene. It was possible to find these optimal conditions for graphene growth thanks to the fast-XPS, which allowed to monitor in real time the variations in the core level spectra of interest induced by modifications of the growth parameters.

As illustrated in fig. 5.7a (bottom), at low C coverage, the C 1s spectrum measured during the ethylene uptake shows a peak centered at 283.5 eV, which is likely due to carbidic carbon. This observation is in good agreement with the findings previously reported by Grüneis *et al.* [31] for the growth of graphene on Ni(111) performed at 900 K. As the coverage increases, a new broad peak appears at about 284.8 eV which eventually reaches saturation, suggesting that the Ni_3Al surface is now covered by a complete graphene layer. Interestingly, upon cooling, this spectral feature evolves into two narrow components separated by 410 meV, GR0 and GR1, which can be now clearly distinguished in the high-energy resolution C 1s core level spectrum reported in fig. 5.7a (central). The Al 2p spectrum of the graphene-covered $Ni_3Al(111)$ shown in fig. 5.7c, besides the spin-orbit splitted doublet characteristic of the clean surface (superimposed in red), shows an additional doublet (green components) induced by the growth of the graphene layer shifted by +160 meV. Taken together, these findings suggest that the double-peak components observed both in the C 1s and Al 2p spectra are related to carbon atoms differently interacting with the underlying substrate.

Besides the (2×2) hexagonal periodicity of the clean surface [32], indicated by the green circles in fig. 5.7b, the LEED pattern measured after graphene growth shows graphene-induced diffraction spots that overlap with the first-order substrate spots, indicated by the red circles. Furthermore, these spots are connected by a dashed ring, indicating the presence of azimuthally oriented graphene domains at $\pm 18.5^\circ$ with respect to the first-order substrate-induced spots.

In order to shed light on its structural and electronic properties, the graphene/ $Ni_3Al(111)$ interface was investigated by means of DFT calculations. In particular, we have performed total energy calculations for selected GR/ $Ni_3Al(111)$ stacking geometries, namely, the *top-fcc*, *top-hcp*, *fcc-hcp*, *bridge-top*, *bridge-fcc* and *bridge-hcp* configurations (see fig. 5.8). These labels indicates the high-symmetry adsorption sites, *i.e.*, *top*, *fcc*, *hcp* and *bridge* sites, for a C atom above the hexagonal $Ni_3Al(111)$ lattice. The DFT calculations yield two structures of minimum energy, the *top-fcc* and the *bridge-top*, with the latter being slightly more favorable, the energy difference being only ~ 60 meV. Interestingly, these structures were found to be energetically favorable in previous calculations also for graphene on the Ni(111) surface [33]. The *bridge-fcc* and the *bridge-hcp* do not have a local

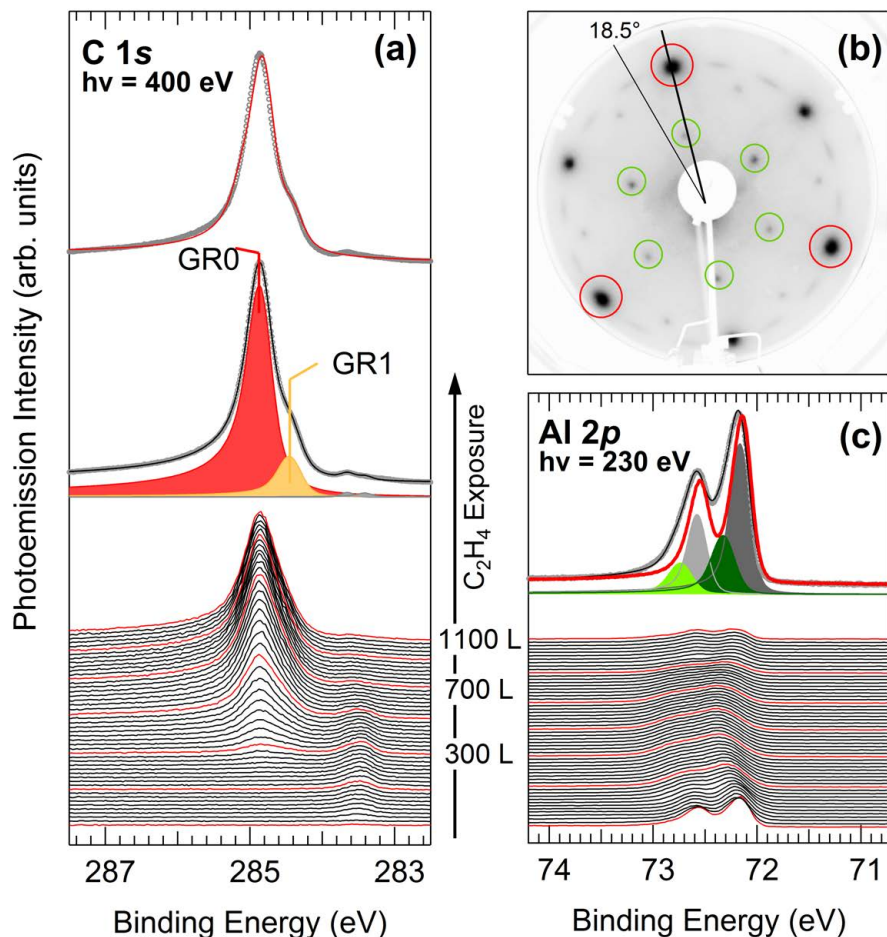


Figure 5.7: Graphene synthesis on Ni₃Al(111). Evolution of the (a) (bottom) C 1s core levels during C₂H₄ uptake at 950 K and (central) high-energy resolution spectrum measured at room temperature after GR growth; (top) photoemission spectrum calculated (red line) from the spectral distribution obtained by DFT calculations for the optimized *top-fcc* configuration (see text for details). (b) LEED pattern of GR/Ni₃Al(111). (c) (bottom) Al 2p core level spectra acquired at different exposures during C₂H₄ uptake at 950 K and (top) high-energy resolution spectrum measured at room temperature after GR growth. The fit result (black) is shown superimposed to the experimental data (grey circle) together with the fitting components: bulk 2p_{3/2} (dark grey), bulk 2p_{1/2} (light grey), surface 2p_{3/2} (dark green) and surface 2p_{1/2} (light green). The Al 2p spectrum of the clean surface is also shown superimposed (red).

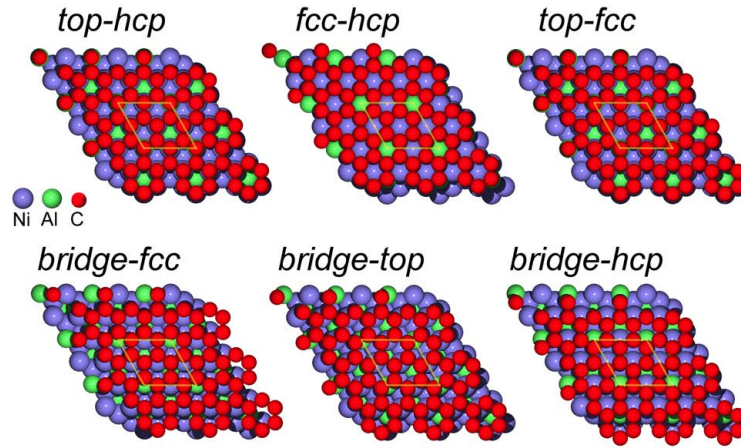


Figure 5.8: Schematic illustration of the different stacking geometries for graphene on $\text{Ni}_3\text{Al}(111)$.

minima and relax into the *top-fcc* and *top-hcp* geometries, respectively. Finally, the *top-hcp* and the *fcc-hcp* structures have a significantly higher energy.

The calculation of the C $1s$ core level binding energies for all non-equivalent carbon atoms within the unit cell has been already shown to be a powerful tool to get insight on the structure of the graphene layer on the $\text{Re}(0001)$ [34] and Pt-Ru alloy [35] surfaces. The combination of DFT calculations and XPS measurements proved to be a powerful approach also in the present investigation. In particular, the knowledge of the theoretical core level binding energies for the structures of minimum energy, *bridge-top* and *top-fcc*, allowed us to simulate the corresponding photoemission spectra. It turns out that the simulated photoemission spectrum corresponding to the *top-fcc* configuration shows a better agreement with the experimental one, as reported in the top part of fig. 5.7a.

The ARPES investigation of the electronic structure of $\text{GR}/\text{Ni}_3\text{Al}(111)$ has also been performed. This shows, compared to the case of quasi-free standing graphene [36], a downward shift of the π -band states, with the Dirac point at -2.7 eV, and the opening of a band gap at the K -point, as illustrated in fig. 5.9a. These findings indicate a strong interaction between graphene and Ni_3Al , and resemble the results previously reported for the case of $\text{GR}/\text{Ni}(111)$ [36]. On the other hand, the high density of states at the Fermi level observed near the M point is due to the metallic character of the alloy substrate, with the dominant contribution of the Ni d -band. Unfortunately, the strong intensity of the Ni states at the Fermi level does not allow to single out the contribution due to the graphene π^* states, and therefore to evaluate the width of the band gap. As illustrated in fig. 5.9b, the band

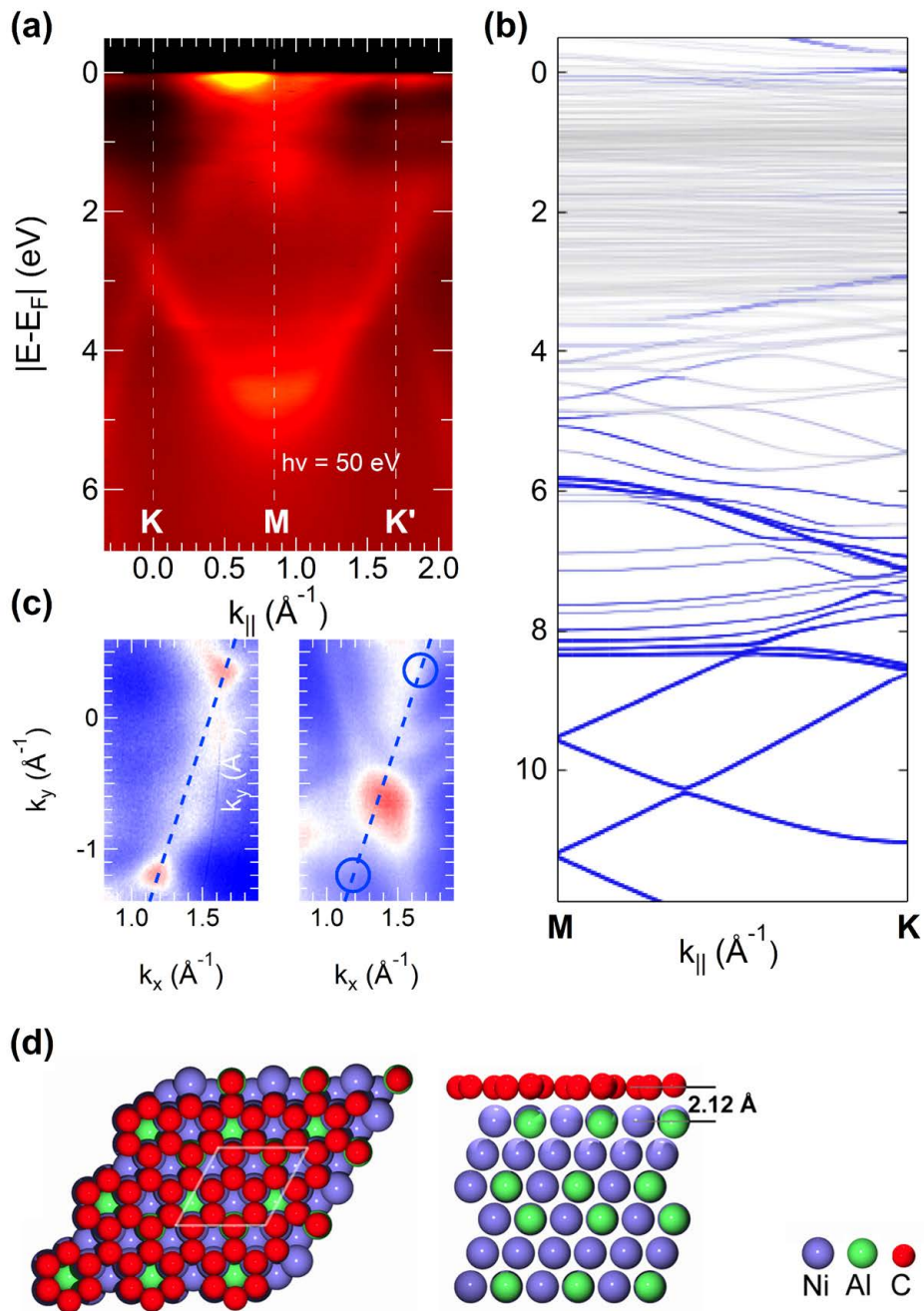


Figure 5.9: (a) Electronic band structure for GR/Ni₃Al(111) measured along the K - M - K' direction and (b) DFT calculated GR energy band dispersion along the M - K direction for the *top-fcc* structure. (c) Constant energy cuts at the Dirac point (left) and at the Fermi level (right). (d) Top and side views for the *top-fcc* GR/Ni₃Al(111) structure.

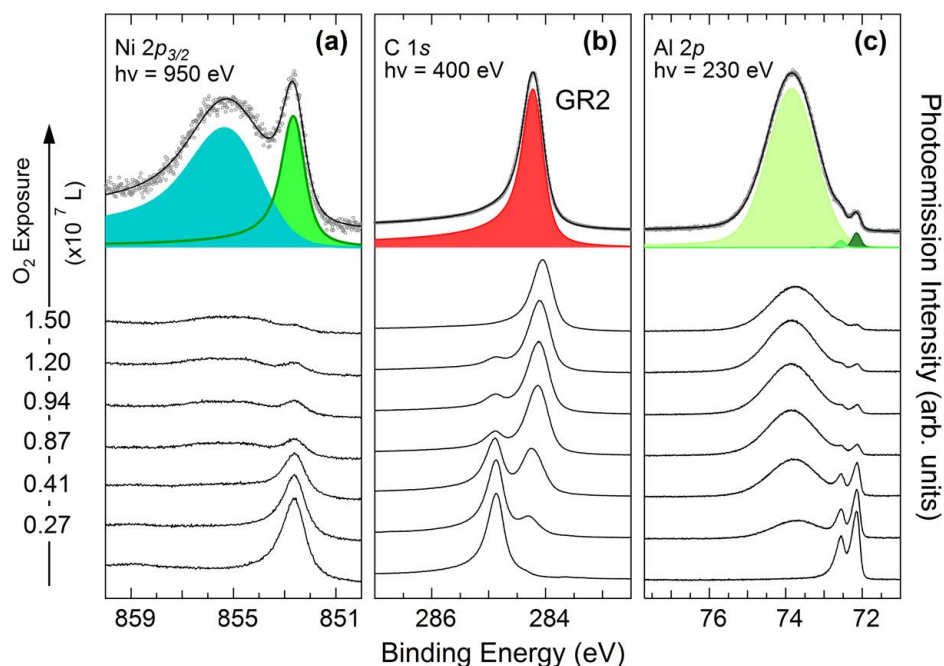


Figure 5.10: Following the O_2 intercalation of GR/ $\text{Ni}_3\text{Al}(111)$ at 520 K through XPS of the (a) $\text{Ni } 2p_{3/2}$, (b) $\text{C } 1s$ and (c) $\text{Al } 2p$ core level spectra measured (bottom) at different oxygen exposures and (top) after the formation of a thick Al_2O_3 layer below GR.

structure calculated for the *top-fcc* configuration shows a very good agreement with the experimental data.

The comparison between theoretical calculations and photoemission experiments points towards the predominant formation of the *top-fcc* phase, which is illustrated in fig. 5.9d. However, the coexistence of other configurations cannot be excluded, especially considering the presence of rotational domains indicated by the ring-shaped features in the LEED pattern.

In the second part of the experiment, the GR/ Ni_3Al interface was exposed to molecular oxygen at 520 K and at a pressure of 4×10^{-3} mbar, resulting in the intercalation of the oxygen underneath the graphene layer and in the selective oxidation of the Al atoms. Fig. 5.10b and c (bottom) shows a set of high-energy resolution XPS spectra acquired after different oxygen exposures for the $\text{C } 1s$ and $\text{Al } 2p$ core levels, respectively. The oxygen intercalation causes the appearance of a new spectral feature in the $\text{C } 1s$ spectra, GR2, at lower binding energy with respect to the as-grown graphene-related components, GR0 and GR1. As the oxygen exposure increases, the intensity of GR2 further increases while GR0 and GR1 disappear, indicating that the graphene layer is progressively decoupled from

the Ni₃Al surface through the formation of an Al₂O₃ layer. After the carbon network has been completely decoupled from the substrate, the C 1s spectrum shows a single, narrow peak centered at 284.2 eV. Interestingly, this value is very similar to that measured on the SiO₂-supported graphene layer described in the previous section, but also to the graphene peak characteristic of the weakly interacting GR-metal interfaces, such as GR/Ir(111) (Section 4.3) and GR/Pt(111) [13], and that of the H regions of GR/Ru(0001) (Section 4.4). The coexistence of GR0 and GR1, from one side, and GR2, from the other, at low oxygen exposures indicates that the decoupling proceeds through the progressive oxidation of the Al atoms, resulting in the expansion of the weakly interacting interface at the expense of the strongly-interacting regions. It is important to note that during oxygen intercalation, the total intensity of the C 1s spectrum decreases by less than 5%, meaning that the carbon network is not seriously damaged by this process.

The evolution of the Al 2p core level spectrum during the oxygen intercalation steps shows the appearance of a broad peak centered at 73.8 eV, which is close to the binding energy measured for the peak characteristic of the Al₂O₃ film [37]. In the latter case, however, the Al 2p region is characterized by a more structured line shape compared to that reported in fig. 5.10c. This behaviour is most probably due to the presence of unresolved spectral contributions related to non-equivalent Al atoms, thus suggesting an amorphous structure of the alumina layer, in agreement with the findings reported for the oxidation of several bimetallic alloys containing Al performed at low temperature [38]. On the other hand, as illustrated in fig. 5.10a, the evolution of the Ni 2p_{3/2} spectra, the Ni atoms are almost unaffected by the oxidation process, which merely causes the appearance of an oxide-related component. This result can be interpreted in terms of a temperature-enhanced segregation of the Al atoms towards the surface, leading to a Ni depletion in the first layers [38]. The estimated thickness of the Al₂O₃ layer is 1.5 ± 0.2 nm (see Section 5.2).

Upon O intercalation, strong modifications can be appreciated in the band structure reported in fig. 5.11a. The π-band undergoes an upward shift towards the Fermi level by ~2 eV, similar to that observed for the graphene band structure on Ni(111) upon Au intercalation [36]. Furthermore, the energy dispersion becomes linear close to the K-points. The group velocity estimated from the dE/dk gradient is $\sim 8 \times 10^5$ m/s, or 1/370 of the speed of light in vacuum. The Dirac point is slightly above the Fermi level by about 200 ± 40 meV (linearly extrapolated value), thus indicating that the graphene layer is p-doped. As a result, the measured band structure is very similar to that of the Au-intercalated quasi-free standing graphene on Ni(111) [36]. The band structure calculated for the GR/α-Al₂O₃(0001) interface well reproduces the ARPES measurements, as illustrated in fig. 5.11b. In particular, the Dirac point is calculated to be 220 meV above the Fermi level, which is quite close to the value extrapolated from the experimen-

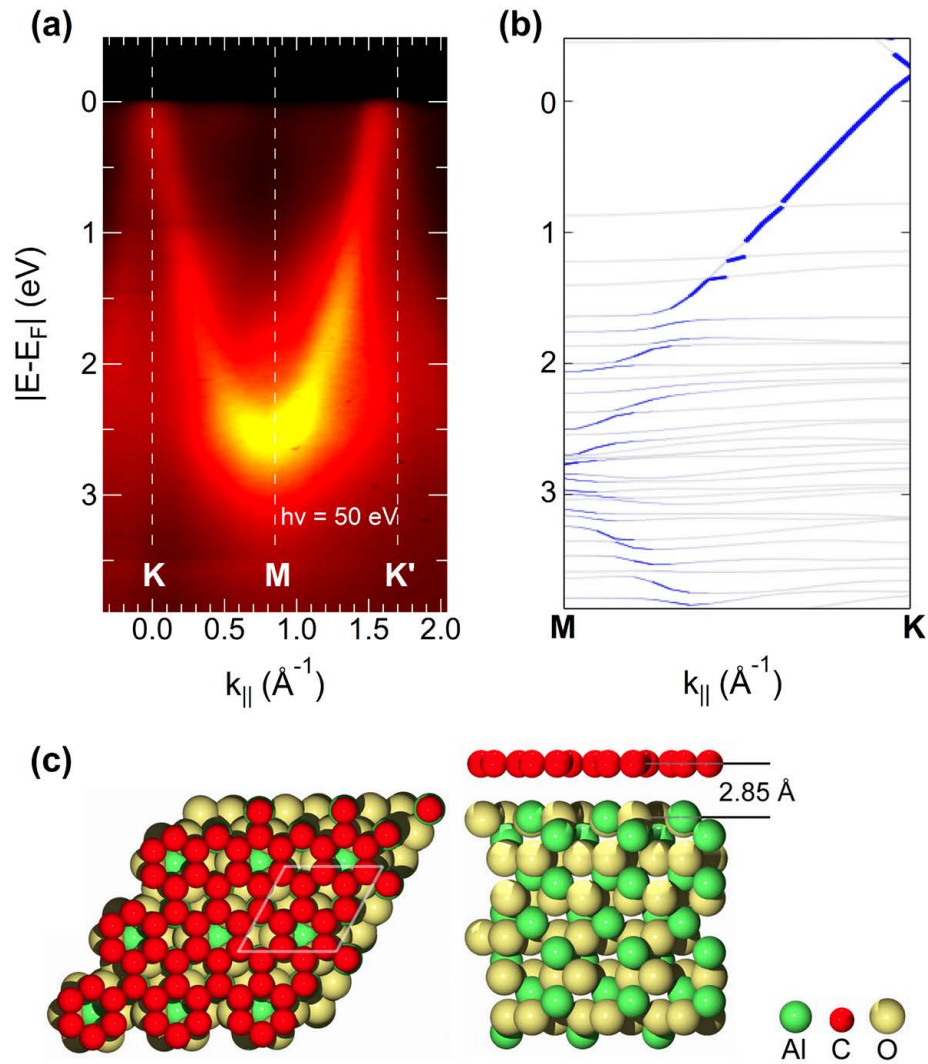


Figure 5.11: (a) Electronic band structure for GR/ Al_2O_3 measured along the K - M - K' direction and (b) DFT calculated GR energy band dispersion along the M - K direction for the GR/ α - Al_2O_3 structure. (c) Top and side views of the GR/ α - Al_2O_3 structure.

tal data. Fig. 5.11c depicts the DFT calculated structure for the GR/ Al_2O_3 , which shows that the graphene distance from the Al_2O_3 substrate is 2.85 Å (the GR- $\text{Ni}_3\text{Al}(111)$ distance is 2.12 Å, see fig. 5.9d).

In order to promote the rearrangement of the amorphous oxide layer into a more ordered structure the sample was annealed to high temperature. Fig. 5.12a and b (bottom) show the C $1s$ and Al $2p$ core level spectra measured during the annealing. The C $1s$ spectrum does not show ap-

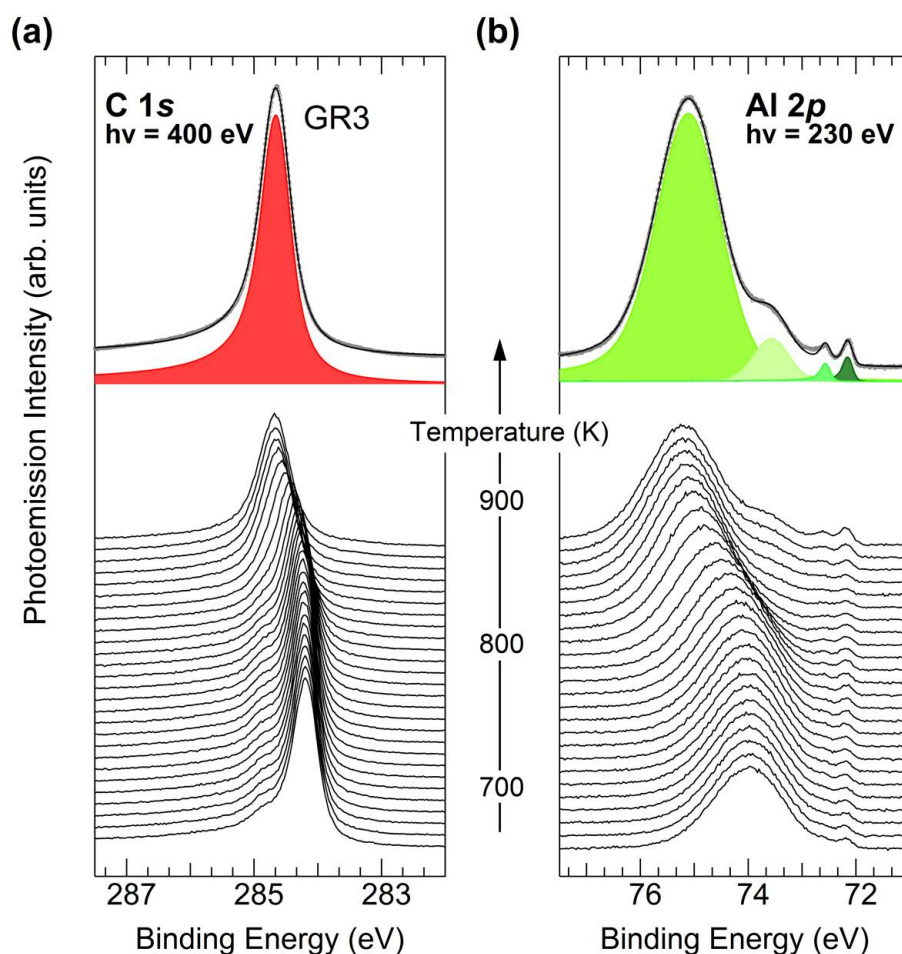


Figure 5.12: (a-b) (bottom) Following the evolution of the C 1s and Al 2p core level spectra during annealing of the GR/Al₂O₃ interface to 950 K. (top) High-energy resolution spectra acquired at room temperature after the annealing.

preciable modifications up to 650 K, when a weak shoulder rises at higher binding energy with respect to GR2. Upon further increasing the temperature, this component grows in intensity at the expense of GR2, and the transition ends at 820 K. The high-energy resolution C 1s spectrum measured at room temperature consists of a single peak, GR3, centered at 284.7 eV, shifted by about 0.5 eV to higher binding energy with respect to the peak measured for the amorphous alumina layer (see the top part of fig. 5.10b). It is noteworthy that the C 1s intensity undergoes a further decrease of $\sim 5\%$, corresponding to an overall intensity reduction of $\sim 8\%$ of the spectrum measured on the as-grown graphene layer.

The evolution of the Al 2p spectrum resembles that of the C 1s core

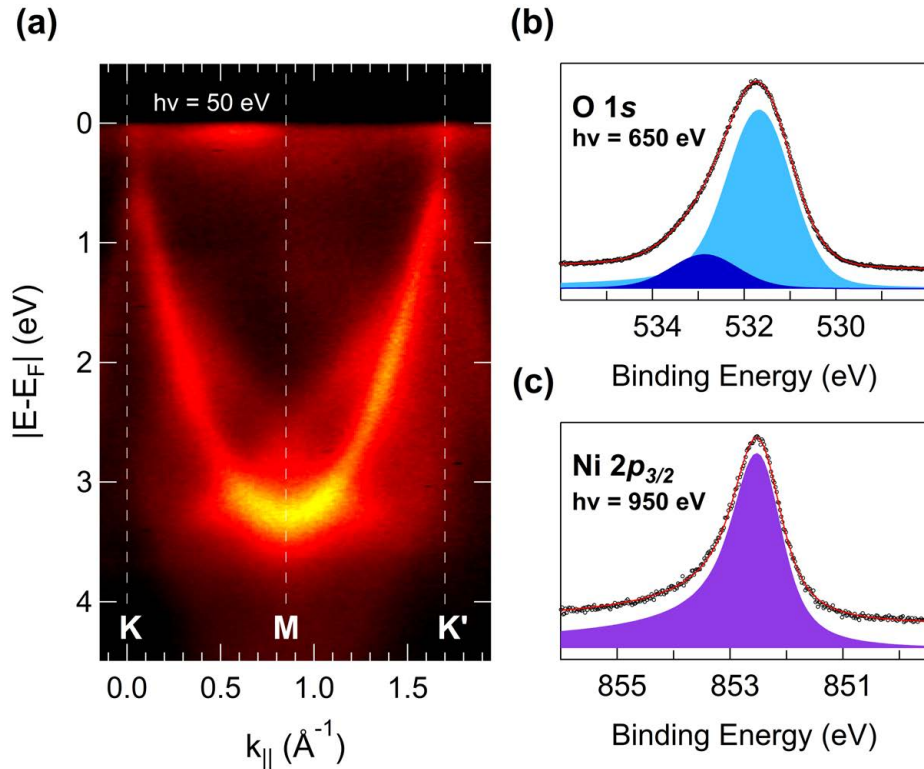


Figure 5.13: (a) Electronic band structure of GR/ Al_2O_3 measured along the K - M - K' direction. (b) O $1s$ and (c) Ni $2p_{3/2}$ core level spectra acquired after the annealing to 950 K.

level, and no modifications are observed up to 650 K. At higher temperature, instead, the broad peak associated with the Al atoms in the oxide layer shifts to higher binding energy and becomes more structured. Two oxide-related components, shifted by about 1.5 eV, can be distinguished in the Al $2p$ spectrum measured at room temperature, displayed in the top part of fig. 5.12b. The lineshapes and binding energies of the spectral components in the Al $2p$ core level are similar to those measured for the well-ordered Al_2O_3 ultra-thin film [37], thus suggesting the rearrangement of the amorphous oxide layer. In addition, also the intensity gain of the components stemming from the metallic Al atoms points towards a reduced thickness of the oxide layer upon annealing.

Fig. 5.13b and c display the O $1s$ and Ni $2p_{3/2}$ spectra measured after the annealing. In accordance with the decreased thickness of the Al_2O_3 layer, the comparison of these spectra with those measured before the annealing indicates an increase of the Ni $2p_{3/2}$ photoemission intensity. This intensity corresponds to a calculated thickness of the thin-film Al_2O_3 layer of $\sim 7 \text{ \AA}$, that is, a 50% reduction compared to the thickness of the amorphous

layer. The O 1s core level, on the other hand, shows an intensity drop of $\sim 14\%$, which correlates with the analogous observation made for the C 1s spectrum. Most likely, this is the effect of a partial consumption of the carbon network, that results in the production of CO or CO₂ species.

The ARPES measurements performed on the annealed GR/Al₂O₃ interface are reported in fig. 5.13a. The graphene π -band undergoes a downward shift, and the opening of band gap is observed at the *K*-points. This suggests that the GR-Ni₃Al(111) interaction is partly re-established. More precisely, the bottom of the π -band at the *M*-point is found at 3.3 eV below the Fermi level, corresponding to a shift of 700 meV with respect to the amorphous oxide (see fig. 5.11a).

In summary, in this Chapter it has been shown that intercalation is a viable and relatively simple route towards the synthesis of graphene/oxide interfaces of variable thickness. Such a method could be extended to other dielectrics of interest for graphene-based electronic devices. This proven concept open many design options and might thus have wide application in graphene research and device fabrication.

Bibliography

1. Kim, K., Choi, J.-Y., Kim, T., Cho, S.-H. & Chung, H.-J. A role for graphene in silicon-based semiconductor devices. *Nature* **479**, 338 (2011).
2. Avouris, P. Graphene: Electronic and photonic properties and devices. *Nano Letters* **10**, 4285 (2010).
3. Ismach, A. *et al.* Direct chemical vapor deposition of graphene on dielectric surfaces. *Nano Letters* **10**, 1542 (2010).
4. Su, C.-Y. *et al.* Direct formation of wafer scale graphene thin layers on insulating substrates by chemical vapor deposition. *Nano Letters* **11**, 3612 (2011).
5. Mao, J. *et al.* Silicon layer intercalation of centimeter-scale, epitaxially grown monolayer graphene on Ru(0001). *Applied Physics Letters* **100**, 093101 (2012).
6. Xia, C. *et al.* Si intercalation/deintercalation of graphene on 6H-SiC(0001). *Physical Review B* **85**, 045418 (2012).
7. Sutter, P., Sadowski, J. T. & Sutter, E. A. Chemistry under cover: Tuning metal-graphene interaction by reactive intercalation. *Journal of the American Chemical Society* **132**, 8175 (2010).
8. Riedl, C., Coletti, C., Iwasaki, T., Zakharov, A. A. & Starke, U. Quasi-free-standing epitaxial graphene on SiC obtained by hydrogen intercalation. *Physical Review Letters* **103**, 246804 (2009).
9. Himpsel, F. J. *et al.* Microscopic structure of the SiO₂/Si interface. *Physical Review B* **38**, 6084 (1988).
10. Seah, M. P. *et al.* Critical review of the current status of thickness measurements for ultrathin SiO₂ on Si part V: Results of a CCQM pilot study. *Surface and Interface Analysis* **36**, 1269 (2004).
11. Vázquez de Parga, A. L. *et al.* Periodically Rippled Graphene: Growth and Spatially Resolved Electronic Structure. *Physical Review Letters* **100**, 056807 (2008).
12. Günther, S. *et al.* Single terrace growth of graphene on a metal surface. *Nano Letters* **11**, 1895 (2011).

13. Preobrajenski, A. B., Ng, M. L., Vinogradov, A. & Mårtensson, N. Controlling graphene corrugation on lattice-mismatched substrates. *Physical Review B* **78**, 073401 (2008).
14. Lu, Z. H., Sham, T. K., Norton, P. R. & Tan, K. H. Photoemission studies of silicon on the Ru(001) surface. *Applied Physics Letters* **58**, 161 (1991).
15. Pasquali, L., Mahne, N., Montecchi, M., Mattarello, V. & Nannarone, S. Formation and distribution of compounds at the Ru-Si(001) ultrathin film interface. *Journal of Applied Physics* **105**, 044304 (2009).
16. Zhang, H., Fu, Q., Cui, Y., Tan, D. & Bao, X. Growth mechanism of graphene on Ru(0001) and O₂ adsorption on the graphene/Ru(0001) surface. *The Journal of Physical Chemistry C* **113**, 8296 (2009).
17. Enta, Y. *et al.* Real-time observation of the dry oxidation of the Si(100) surface with ambient pressure x-ray photoelectron spectroscopy. *Applied Physics Letters* **92**, 012110 (2008).
18. Abbati, I. *et al.* Interaction of oxygen with silicon *d*-metal interfaces: A photoemission investigation. *Journal of Vacuum Science & Technology* **21**, 409 (1982).
19. Cros, A., Pollak, R. A. & Tu, K. N. Room-temperature oxidation of Ni, Pd, and Pt silicides. *Journal of Applied Physics* **57**, 2253 (1985).
20. Löffler, D. *et al.* Growth and structure of crystalline silica sheet on Ru(0001). *Physical Review Letters* **105**, 146104 (2010).
21. Lizzit, S. *et al.* Surface core-level shifts of clean and oxygen-covered Ru(0001). *Physical Review B* **63**, 205419 (2001).
22. Rangan, S., Bersch, E., Bartynski, R. A., Garfunkel, E. & Vescovo, E. Band offsets of a ruthenium gate on ultrathin high- κ oxide films on silicon. *Physical Review B* **79**, 075106 (2009).
23. Sutter, P., Flege, J.-I. & Sutter, E. A. Epitaxial graphene on ruthenium. *Nature Materials* **7**, 406 (2008).
24. Wells, J. W. *et al.* The conductivity of Bi(111) investigated with nano-scale four point probes. *Journal of Applied Physics* **104**, 053717 (2008).
25. Jobst, J. *et al.* Quantum oscillations and quantum Hall effect in epitaxial graphene. *Physical Review B* **81**, 195434 (2010).
26. Zhang, Y., Tan, Y.-W., Stormer, H. L. & Kim, P. Experimental observation of the quantum Hall effect and Berry's phase in graphene. *Nature* **438**, 201 (2010).
27. Klarskov, M. B. *et al.* Fast and direct measurements of the electrical properties of graphene using micro four-point probes. *Nanotechnology* **22**, 445702 (2011).

28. Lahiri, J. *et al.* Graphene growth and stability at nickel surfaces. *New Journal of Physics* **13**, 025001 (2011).
29. Lahiri, J., Miller, T., Adamska, L., Oleynik, I. I. & Batzill, M. Graphene growth on Ni(111) by transformation of a surface carbide. *Nano Letters* **11**, 518 (2011).
30. Addou, R., Dahal, A., Sutter, P. & Batzill, M. Monolayer graphene growth on Ni(111) by low temperature chemical vapor deposition. *Applied Physics Letters* **100**, 021601 (2012).
31. Grüneis, A., Kummer, K. & Vyalikh, D. V. Dynamics of graphene growth on a metal surface: A time-dependent photoemission study. *New Journal of Physics* **11**, 073050 (2009).
32. Bikondoa, O., Castro, G. R., Torrelles, X., Wendler, F. & Moritz, W. Surface-induced disorder on the clean Ni₃Al(111) surface. *Physical Review B* **72**, 195430 (2005).
33. Zhao, W. *et al.* Graphene on Ni(111): coexistence of different surface structures. *The Journal of Physical Chemistry Letters* **2**, 759 (2011).
34. Miniussi, E. *et al.* Thermal stability of corrugated epitaxial graphene grown on Re(0001). *Physical Review Letters* **106**, 216101 (2011).
35. Alfé, D. *et al.* Fine tuning of graphene-metal adhesion by surface alloying. *Scientific Reports* **3**, 2430 (2013).
36. Varykhalov, A. *et al.* Electronic and magnetic properties of quasifree-standing graphene on Ni. *Physical Review Letters* **101**, 157601 (2008).
37. Vesselli, E., Baraldi, A., Lizzit, S. & Comelli, G. Large interlayer relaxation at a metal-oxide interface: The case of a supported ultrathin alumina film. *Physical Review Letters* **105**, 046102 (2010).
38. Franchy, R. Growth of thin, crystalline oxide, nitride and oxynitride films on metal and metal alloy surfaces. *Surface Science Reports* **38**, 195 (2000).

Chapter 6

Synthesis and Characterization of Nitrogen-Doped Graphene on Ir(111)

6.1 Introduction

The combination of many outstanding properties in a single material, makes graphene really attractive for a number of technological applications. In this regard, the use of graphene single layers into high-performance integrated circuits is one of the most intriguing prospects. However, the absence of a gap in its band structure, sets severe limits on the use of graphene in, *e.g.*, transistors because of the low high on-off ratio achievable [1]. This is the reason why the opening and fine tuning of an energy gap in the band structure of graphene has been an issue of fundamental importance since the discovery of this unique material. Different routes have been followed to tailor the electronic properties of graphene. The first to be explored were methods based on the morphology control over the graphene structure. For instance, by making graphene nanoribbons it is possible to laterally confine the charge carriers. In nanoribbons, different types of edges show either metallic (zigzag edge) or semiconducting (armchair edge) character [2]. Furthermore, the possibility of opening a band gap in bilayer graphene by applying a strong electric field [3] or by selectively controlling the carrier density in each layer [4] have also been explored. However, these approaches resulted in a small band gaps or in a strong degradation of the carrier mobility [1].

A promising approach to modify the electronic properties of graphene is chemical doping, which can be achieved by patterning the graphene surface with atoms [5] or molecules [6], or by introducing heteroatoms in the carbon network [7]. In the latter case, in particular, the substitution of carbon with nitrogen or boron atoms is of considerable interest because not

only it shifts the position of the Dirac point leading to *n*- or *p*-doped graphene, but can also modify the characteristic features of the graphene electronic band structure [8]. For carbon sp^2 structures, especially, the incorporation of nitrogen in the lattice has been already demonstrated to be a robust and efficient method to tune the electronic properties of graphene with only minor structural perturbations, due to the possibility to form covalent bonds [9, 10].

Several methods have been developed to synthesize N-doped graphene. For instance, direct synthesis of N-doped graphene can be achieved by CVD [11] or arc discharge [12] approaches. On the other hand, post-synthesis methods are also widely used, such as thermal annealing [13] in NH_3 atmosphere or plasma treatment [14]. Three different atomic configurations for the nitrogen atoms in the carbon network have been observed in these studies, namely, graphitic (also known as substitutional), pyridinic and pyrrolic nitrogen (see fig. 6.1). Despite several characterization tools have been used to investigate the resulting N-doped graphene layers, including STM [15, 16], TEM [17], XPS [9, 10] and Raman spectroscopy [11, 18], the connection between the nitrogen bonding configuration and the synthesis method is not always straightforward.

Motivated by this lack of information, we exploited the potential offered by the SuperESCA beamline to study the functionalization and to determine the surface structure of a N-doped graphene layer produced with nitrogen plasma exposure of GR/Ir(111). This Chapter is devoted to illustrate how a combined XPS and XPD investigation can provide insight on the correlation between the electronic and structural properties of N-doped graphene.

6.2 Experimental Details

The preparation of the Ir(111) single crystal and the subsequent growth of graphene were performed following the procedures already described in Section 4.2. The as-grown graphene was then exposed to nitrogen plasma at room temperature. Different combination of plasma pressure, position of the sample surface with respect to the plasma source and exposure time were tested. Optimal conditions were found for exposures with N_2 pressure of 2.5×10^{-5} mbar performed with the sample placed in front of the plasma source.

6.3 Results and Discussion

As a first step, we followed the formation of the nitrogen-doped graphene on Ir(111) by monitoring the N 1s, C 1s and Ir $4f_{7/2}$ core level spectra after 3 and 10 minutes of plasma exposure, as shown in fig. 6.1(a-c). After 3 min

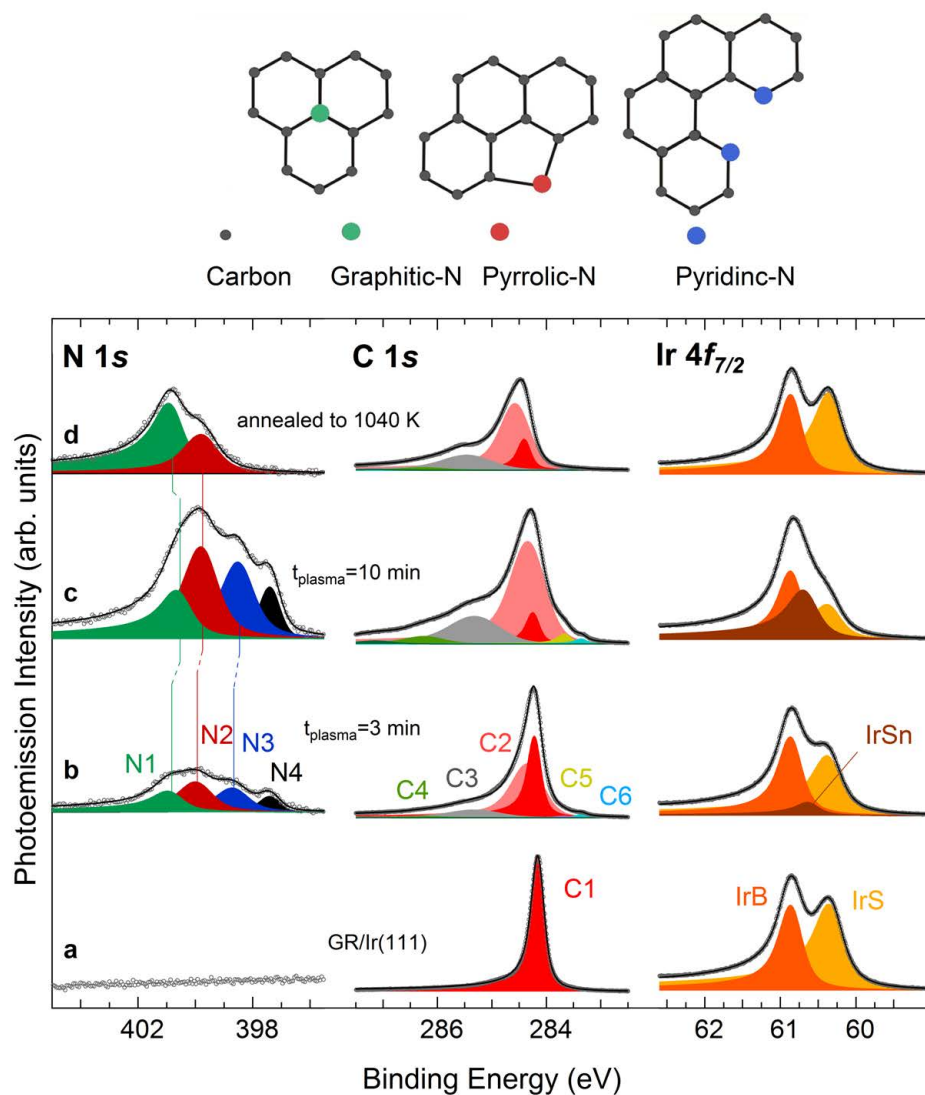


Figure 6.1: N $1s$, C $1s$ and Ir $4f_{7/2}$ core level spectra measured (a-c) after exposure of GR/Ir(111) to N_2 plasma and (d) after annealing to 1040 K. The colored peaks represent the result of a deconvolution into different contributions, as discussed in the text. The sketch on the top part shows the possible binding configurations of nitrogen atoms in graphene.

of nitrogen exposure, the N $1s$ core level region exhibits a broad spectrum, where at least four spectral features can be clearly distinguished, arising from nitrogen atoms in different chemical environments: N1 (400.3 eV), N2 (399.5 eV), N3 (398.2 eV) and N4 (397.4 eV). As the exposure time increases, N1, N2 and N3 progressively shift by about 0.3 eV towards lower binding energies, while N4 remains fixed. The measured binding ener-

gies match several previously reported photoemission data on N-doped graphene [10, 11, 13, 18–20], where the N1, N2 and N3 components were assigned to graphitic, pyrrolic and pyridinic nitrogen, respectively (see top part of fig. 6.1). On the other hand, the position of N4 is close to the N 1s core level binding energy measured for nitrogen atoms adsorbed on Ir(111), ranging between 397.3 and 397.6 eV [21]. Therefore, we assign N4 to nitrogen atoms that intercalate below graphene and chemisorb on the Ir substrate. It is noteworthy that, at this stage, the pyrrolic- and pyridinic-N are dominant in our sample (37 and 29% of the nitrogen total signal) with respect to the graphitic (21%) and atomic (13%) features.

The growth of several components in the N 1s core level region is paralleled by a broadening of the C 1s spectrum, reflecting the disruption of the graphene lattice induced by incorporation of nitrogen atoms. As a result, the main C 1s peak (C1) slightly shifts by 0.1 eV towards higher binding energy with respect to the position of the undoped graphene (284.1 eV), and a new, broad feature (C2) emerges at 284.3 eV. The latter is attributed to sp^2 C-C bonded atoms affected by the nitrogen inclusion in the carbon network. In parallel, several other components appear in the C 1s region: C3 (285.3 eV) and C4 (286.2 eV) are assigned to different C-N bonding structures, sp^2 C-N and sp^3 C-N bonds, respectively [22]. Carbon vacancies give rise to C5 (283.7 eV) [23], whereas the small C6 component (283.4 eV) is attributed to C atoms at the iridium steps [24].

The variations in the chemical composition of the graphene layer lead to noticeable changes also in the Ir $4f_{7/2}$ spectra. As already explained in Section 4.3, the Ir $4f_{7/2}$ spectrum of pristine GR/Ir(111) consists of two components, representing bulk (IrB at 60.84 eV) and surface (IrS at 60.31 eV) atoms, and it is very similar to that of clean Ir(111) [24]. Upon nitrogen plasma treatment, a new component IrSn appears between the surface and the bulk peaks at 60.60 eV, which eventually shifts by ~ 50 meV towards higher binding energies upon a second plasma exposure. This is paralleled by a decrease of the IrS photoemission intensity, due to the interaction of the N-doped graphene with the iridium substrate.

The XPS findings confirm the doping of the graphene layer and indicate that nitrogen atoms are embedded into the carbon network. However, a sizeable amount of N atoms intercalate underneath the graphene layer, as witnessed by the high intensity of the N4 peak. As already discussed for the O₂ intercalation process on the GR/Ir(111) interface (see Section 4.3), intercalation takes place at pre-existing graphene defects or wrinkles. In this case, however, the inclusion of nitrogen atoms in the graphene lattice introduces defects in graphene, fostering further intercalation. As a result, the carbon network is damaged upon nitrogen plasma exposure.

In order to shed light on the thermal stability of the N-doped graphene we performed a thermal desorption experiment and monitored the N 1s core level during the annealing. Fig. 6.2a shows a selection of the time-

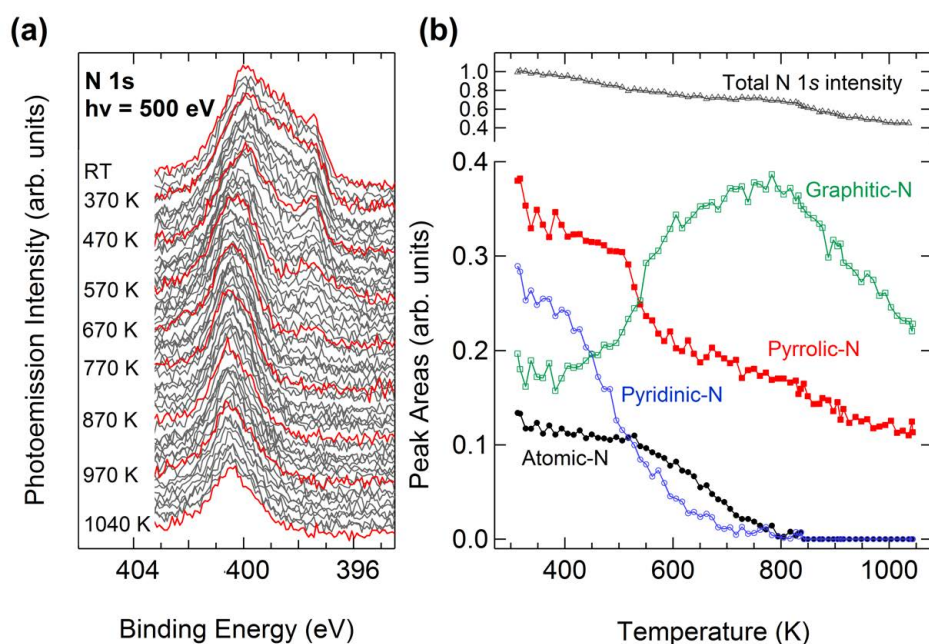


Figure 6.2: Annealing of N-graphene/Ir(111). (a) Selected N 1s spectra measured during the annealing ramp. (b) Quantitative analysis of the evolution of the different surface species.

lapsed N 1s spectra acquired during annealing of the substrate up to 1040 K. The quantitative analysis of these fast-XPS spectra is displayed in fig. 6.2b. Upon annealing, the total amount of nitrogen gets reduced to about 65% of the initial value. However, the most interesting aspect of the annealing process is the conversion of part of the pyridinic and pyrrolic species into graphitic nitrogen between 470 and 770 K, as indicated by the significant increase of the N1 component intensity at the expense of N2 and N3 in this temperature range. It should be noted that the transformation of nitrogen impurities upon postannealing has been already observed for similar interfaces [10, 20, 25]. Above 820 K, the intensity of the pyrrolic and graphitic components, which are the only ones still observed at this stage, gradually decreases. The behaviour of the atomic nitrogen component, which disappears above 770 K, resembles that observed on the pristine Ir(111) surface, where the nitrogen atoms desorb as N₂ between 400 and 700 K [21]. Therefore, most likely the atomic nitrogen is not involved in the conversion process. The analysis of the XPS spectra suggests the conversion of pyrrolic- into graphitic-N. This should be the main process, as evidenced by the correlation of the intensities of these two components in fig. 6.2a, but the transformation of pyridinic-N cannot be ruled out.

Fig. 6.1d shows the core levels of interest measured at room temperature after the annealing at 1040 K. As described above, now the sample

contains nitrogen atoms only in graphitic and pyrrolic configurations with an intensity ratio of about 2:1. Remarkably, the Ir $4f_{7/2}$ spectrum measured after the annealing (d) is almost indistinguishable from that of the undoped system (a). Indeed, upon annealing the IrSn component is completely depleted, while the IrS intensity is fully restored. It is even more interesting to compare the Ir spectrum registered after the annealing and that measured after 3 minutes of plasma exposure, spectra (d) and (b), respectively. In both cases, the carbon lattice is N-doped. In particular, since the amount of nitrogen is smaller for the GR/Ir interface exposed to 3 min of plasma dose with respect to the annealed sample, as indicated by the corresponding N $1s$ integrated areas, one would expect the intensity of the IrSn component to be lower for the latter system. Surprisingly, what happens is just the opposite: although the larger number of nitrogen atoms included in the graphene layer, the IrSn component, which is related to the Ir surface atoms interacting with the N-doped graphene layer, cannot be detected after the annealing. This finding suggests that the interaction between N-doped graphene (with graphitic- and pyrrolic-N) and the Ir surface is weak and resembles that of the as grown graphene on Ir(111). This result indicates that the graphene layer is not significantly deformed upon nitrogen inclusion in substitutional and pyrrolic form, *i.e.*, the nitrogen impurities are located in the lattice plane and do not induce a vertical deformation of graphene.

The major change in the C $1s$ spectra is a shift by ~ 200 meV towards higher binding energy of C1, C2 and C3. The disappearance of the C4, C5 and C6 is interpreted as a great reduction of the defective sites caused by the plasma exposure, *i.e.*, the high temperature annealing allows to partly recover the hexagonal lattice. The intensity ratio between the other components is roughly the same as it was before the annealing.

To gain further insight into the structure of the N-doped graphene, we performed XPD measurements by collecting N $1s$ photoemission spectra at different emission angles. These measurements were carried out on a graphene layer exposed to N_2 plasma for 30 min, and subsequently annealed to about 800 K in order to allow the conversion of the nitrogen species, with the maximum concentration of graphitic-N (see fig. 6.2b). Fig. 6.3a shows the stereographic projection of the N $1s$ photoemission intensity modulation of the graphitic component. The most interesting result of the XPD measurements is the striking similarity between the diffraction patterns of the N $1s$ graphitic component (N1) and the C $1s$ component (C1) of the pristine GR/Ir(111) interface (fig. 6.3b) measured at the same photoelectron kinetic energy. This further confirms that the inclusion of substitutional of nitrogen does not affect the local structural geometry of the carbon network.

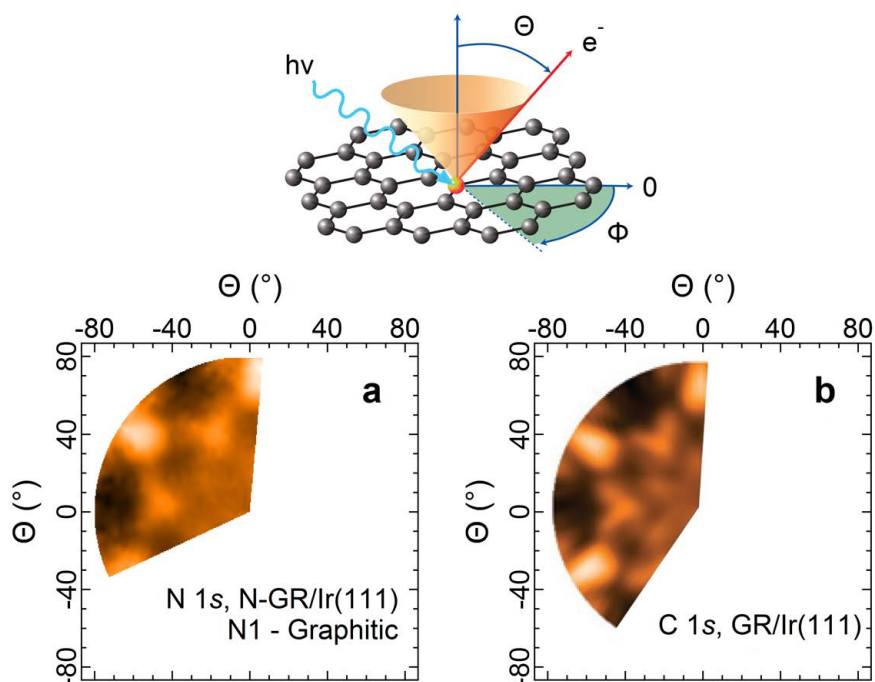


Figure 6.3: Stereographic projection of the integrated photoemission intensity modulation $I(\theta, \phi)$ as a function of emission angle (see fig. 3.9 caption) for (a) the N $1s$ graphitic component and (b) the C $1s$ component of the pristine GR/Ir(111) interface. The N $1s$ and C $1s$ scans are taken at $h\nu = 515$ and 400 eV, respectively, which correspond to the same photoelectron kinetic energy of 115 eV. A schematic of the experimental configuration for the XPD measurements is shown at the top.

In conclusion, in the experiment described in this Chapter, XPS proved to be a powerful tool to characterize in detail the composition of the nitrogen species and to understand how their concentrations modify upon annealing. Furthermore, the XPD investigation of N-doped graphene allowed for a deeper understanding of the bonding geometry of nitrogen atoms embedded in the graphene lattice.

Bibliography

1. Schwierz, F. Graphene transistors. *Nature Nanotechnology* **5**, 487 (2010).
2. Zhan, D. *et al.* Engineering the electronic structure of graphene. *Advanced Materials* **24**, 4055 (2012).
3. Zhu, W., Neumayer, D., Perebeinos, V. & Avouris, P. Silicon nitride gate dielectrics and band gap engineering in graphene layers. *Nano Letters* **10**, 3572 (2010).
4. Ohta, T., Bostwick, A., Seyller, T., Horn, K. & Rotenberg, E. Controlling the electronic structure of bilayer graphene. *Science* **313**, 951 (2006).
5. Balog, R. *et al.* Bandgap opening in graphene induced by patterned hydrogen adsorption. *Nature Materials* **9**, 315 (2010).
6. Schedin, F. *et al.* Detection of individual gas molecules adsorbed on graphene. *Nature Materials* **6**, 652 (2007).
7. Banhart, F., Kotakoski, J. & Krasheninnikov, A. V. Structural defects in graphene. *ACS Nano* **5**, 26 (2011).
8. Ci, L. *et al.* Atomic layers of hybridized boron nitride and graphene domains. *Nature Materials* **9**, 430 (2010).
9. Wang, Y., Shao, Y., Matson, D. W., Li, J. & Lin, Y. Nitrogen-doped graphene and its application in electrochemical biosensing. *ACS Nano* **4**, 1790 (2010).
10. Sheng, Z.-h. *et al.* Catalyst-free synthesis of nitrogen-doped graphene via thermal annealing graphite oxide with melamine and its excellent electrocatalysis. *ACS Nano* **5**, 4350 (2011).
11. Wei, D. *et al.* Synthesis of N-doped graphene by chemical vapor deposition and its electrical properties. *Nano Letters* **9**, 1752 (2009).
12. Li, N. *et al.* Large scale synthesis of N-doped multi-layered graphene sheets by simple arc-discharge method. *Carbon* **48**, 255 (2010).
13. Li, X. *et al.* Large-area synthesis of high-quality and uniform graphene films on copper foils. *Science* **324**, 1312 (2009).
14. Lin, Y.-C., Lin, C.-Y. & Chiu, P.-W. Controllable graphene N-doping with ammonia plasma. *Applied Physics Letters* **96**, 133110 (2010).

15. Zhao, L. *et al.* Visualizing individual nitrogen dopants in monolayer graphene. *Science* **333**, 999 (2011).
16. Joucken, F. *et al.* Localized state and charge transfer in nitrogen-doped graphene. *Physical Review B* **85**, 161408 (2012).
17. Meyer, J. C. *et al.* Experimental analysis of charge redistribution due to chemical bonding by high-resolution transmission electron microscopy. *Nature Materials* **10**, 209 (2011).
18. Zhang, C. *et al.* Synthesis of nitrogen-doped graphene using embedded carbon and nitrogen sources. *Advanced Materials* **23**, 1020 (2011).
19. Kim, K.-J. *et al.* Surface property change of graphene using nitrogen ion. *Journal of Physics: Condensed Matter* **22**, 045005 (2010).
20. Usachov, D. *et al.* Nitrogen-doped graphene: Efficient growth, structure, and electronic properties. *Nano Letters* **11**, 5401 (2011).
21. Weststrate, C., Bakker, J., Gluhoi, A., Ludwig, W. & Nieuwenhuys, B. Ammonia oxidation on Ir(111): why Ir is more selective to N₂ than Pt. *Catalysis Today* **154**, 46 (2010).
22. Chan, L. H. *et al.* Resolution of the binding configuration in nitrogen-doped carbon nanotubes. *Physical Review B* **70**, 125408 (2004).
23. Barinov, A. *et al.* Initial stages of oxidation on graphitic surfaces: Photoemission study and density functional theory calculations. *The Journal of Physical Chemistry C* **113**, 9009 (2009).
24. Lacovig, P. *et al.* Growth of dome-shaped carbon nanoislands on Ir(111): the intermediate between carbidic clusters and quasi-free-standing graphene. *Physical Review Letters* **103**, 166101 (2009).
25. Kumar, A., Ganguly, A. & Papakonstantinou, P. Thermal stability study of nitrogen functionalities in a graphene network. *Journal of Physics: Condensed Matter* **24**, 235503 (2012).

Chapter 7

Concluding Remarks and Outlook

Graphene and *h*-BN grown by chemical vapour deposition on metal supports have been introduced and their structural and electronic properties have been discussed in this thesis.

Chapter 3 has been devoted to the optimization of the CVD growth procedure of *h*-BN on Ir(111), which is so far the most promising candidate substrate for high-quality graphene-based electronics. Starting from the characterization of the adsorption of the *h*-BN molecular precursor, borazine, we found that molecular dissociation occurs already near room temperature, yielding molecular fragments readily available for the formation of the *h*-BN honeycomb structure. The annealing of the borazine saturated surface at high temperature leads to the formation of the *h*-BN layer, and repeated cycles of this procedure ensure an extended *h*-BN monolayer covering the whole Ir(111) surface. We observed that, compared to the standard CVD approach consisting in borazine deposition at high temperature, the method described above leads to a well-defined orientation of the *h*-BN layer. More precisely, while the ordinary high-temperature deposition gives rise to the nucleation of *h*-BN domains with opposite *fcc* and *hcp* orientations, our approach yields to a *h*-BN monolayer formed only by *fcc* domains. This result is explained as due to a different interplay between the thermal energy and the energy difference between *fcc* and *hcp* adsorption configurations in the first stages of the CVD process. It is important to stress that the merging of different domains leads inevitably to the formation of defects and grain boundaries. Therefore, our CVD approach is an important step towards the development of reliable routes for the controlled growth of high quality *h*-BN monolayers.

Another objective of my PhD project has been to explore the possibility of tuning the interaction of graphene with different metallic substrates by oxygen intercalation. This idea was successfully pursued for two ex-

treme situations of weak, GR/Ir(111), and strong, GR/Ru(0001), interaction as illustrated in Chapter 4. We found that oxygen intercalation can be achieved on a complete epitaxial graphene layer on Ir(111) by choosing the proper combination of oxygen pressure (in the 10^{-3} mbar range), and substrate temperature (520 K). Oxygen intercalation is followed by dissociative chemisorption on the metal substrate below graphene, this process being similar to the adsorption of oxygen on the clean Ir(111) surface. The characteristic spectral features of the graphene-Ir(111) interaction, such as minigaps and replica bands, are missing in the case of the O-intercalated graphene. At the same time, an upward shift of the π -band is observed, corresponding to an electron transfer from graphene to the oxygen-covered Ir surface, which leads to a quasi-free standing *p*-doped graphene with a single Dirac cone around the K -point. Similar results were found for the oxygen intercalation through graphene on Ru(0001), proving that intercalation is a viable route also for decoupling a strongly interacting graphene-metal interface. Oxygen deintercalation was also investigated for GR/O/Ir(111), this process occurring in a rather abrupt way at about 600 K. After deintercalation the graphene-Ir interaction is re-established. However, deintercalation causes also a slight etching of the carbon network, allowing additional intercalation/deintercalation cycles to occur at lower oxygen pressure and temperatures. Oxygen intercalation is therefore an effective method to change the graphene-metal substrate interaction. Furthermore, this approach opens a series of opportunities in the field of fundamental studies on graphene, where free-standing, highly ordered and extended layers of graphene are of outmost importance.

We made one step further and developed a novel transfer-free method based on intercalation, to achieve electrical decoupling of graphene from the metal substrate it is grown on. In particular, in Chapter 5 we have shown that it is possible to electrically insulate graphene from Ru(0001) by a stepwise intercalation of Si and O₂. Intercalation of 4 ML of Si at the GR/Ru(0001) interface leads to the formation of a Ru-silicide, which is then oxidized by additional reaction with intercalated O₂, eventually resulting in a 1.8 nm-thick SiO₂ layer. Si intercalation and oxidation were followed by high-energy resolution XPS, while the electrical insulation was demonstrated by performing lateral transport measurements. We extended the intercalation approach to the GR/Ni₃Al(111) system to achieve the electrical insulation of graphene. In particular, we have shown that epitaxial graphene grown on a bimetallic Ni₃Al(111) alloy surface and its subsequent intercalation with molecular oxygen results in the selective oxidation of the Al atoms and in the formation of a 1.5 nm-thick Al₂O₃ layer. It should be possible to take advantage of the intercalation to promote the chemical synthesis of other dielectric of high interest for graphene-based electronic devices, such as high-*k* oxides or even *h*-BN. This approach would represent an encouraging prospect for the fabrication of devices based on graphene.

Finally, in Chapter 6 we have discussed the functionalization of graphene by substitution of C lattice atoms with N atoms. We have shown that it is possible to synthesize nitrogen-doped graphene on Ir(111) by nitrogen plasma treatment of the CVD-grown graphene. Different types of bonding configurations were identified by means of high energy resolution core level photoemission, namely, graphitic, pyridinic and pyrrolic nitrogen. We investigated the thermal stability of the N-doped graphene and found that graphitic nitrogen is the most stable configuration. Furthermore, the connection of the graphitic nitrogen arrangement with its corresponding spectroscopic fingerprint was unequivocally stated by performing photoelectron diffraction measurements, which gave a direct insight on the local geometry of the nitrogen atoms incorporated in the carbon network.

In conclusion, in this PhD project I have investigated the interaction of graphene and hexagonal boron nitride layers with different materials. In spite of the structural perfection achieved in graphene single layers, the development of procedures that allow the separation of the film from the metal substrates is still in its infancy. While quasi-free standing graphene could be useful for fundamental research, carbon-based electronics will require graphene to be placed on insulating substrates. Therefore many breakthroughs are soon expected in the field of graphene/insulator interfaces. These are fundamental issues to address, since in any technical application metallic contacts to graphene will be unavoidable and graphene will be likely placed on insulating substrates, including *h*-BN. We have shown that the comprehension of the atomic scale properties is a powerful approach towards a deeper understanding of graphene properties and optimization of graphene-based materials. I hope that the proven concepts and methods used in this work will foster further contributions to the development of a new generation of technologies specifically designed for 2D atomic crystals.

Appendix A

Publications

- [1] M. Bianchi, D. Cassese, A. Cavallin, R. Comin, **F. Orlando**, L. Postregna, E. Golfetto, S. Lizzit, and A. Baraldi. Surface core level shifts of clean and oxygen covered Ir(111), *New Journal of Physics* **11**, 063002 (2009).

Part of the study on the *h*-BN/Ir(111) (Chapter 3) can be found in:

- [2] **F. Orlando**, R. Larciprete, P. Lacovig, I. Boscarato, A. Baraldi, and S. Lizzit. Epitaxial growth of hexagonal boron nitride on Ir(111), *The Journal of Physical Chemistry C* **116**, 157 (2012).

The investigation of the oxygen-intercalated graphene/Ir(111) interface (Chapter 4) can be found in:

- [3] R. Larciprete, S. Ulstrup, P. Lacovig, M. Dalmiglio, M. Bianchi, F. Mazzola, L. Hornekær, L. Barreto, **F. Orlando**, A. Baraldi, Ph. Hofmann, and S. Lizzit. Oxygen switching of the epitaxial graphene-metal interaction, *ACS Nano* **6**, 9551 (2012).

Highlighed in *Nature Materials* **12**, 3 (2013).

The work on the transfer-free method to decouple the graphene/Ru(0001) interface through a SiO₂ layer (Chapter 5) can be found in:

- [4] S. Lizzit, R. Larciprete, P. Lacovig, M. Dalmiglio, **F. Orlando**, A. Baraldi, L. Gammelgaard, L. Barreto, M. Bianchi, E. Perkins, and Ph. Hofmann. Transfer-free electrical insulation of epitaxial graphene from its metal substrate, *Nano Letters* **12**, 4503 (2012).

Highlighed in *Nature Nanotechnology* **7**, 613 (2012).

Further works have been submitted or are currently in preparation:

- **F. Orlando**, P. Lacovig, R. Larciprete, A. Baraldi, and S. Lizzit. Epitaxial growth of large-area single-domain hexagonal boron nitride (submitted).
- **F. Orlando**, R. Larciprete, P. Lacovig, A. Baraldi, and S. Lizzit. Synthesis of N-doped graphene via plasma-assisted method (in preparation).

List of the Acronyms

AES	Auger Electron Spectroscopy
ARPES	Angle Resolved PhotoEmission Spectroscopy
BE	Binding Energy
CLS	Core Level Shift
CVD	Chemical Vapor Deposition
DFT	Density Functional Theory
EDAC	Electron Diffraction in Atomic Clusters
EELS	Electron Energy Loss Spectroscopy
ESCA	Electron Spectroscopy for Chemical Analysis
EXAFS	Extended X-ray Absorption Fine Structure
HOPG	Highly Oriented Pyrolytic Graphite
LEED	Low Energy Electron Diffraction
MDC	Momentum Distribution Curve
NEXAFS	Near Edge X-ray Absorption Fine Structure
SCLS	Surface Core Level Shift
STM	Scanning Tunneling Microscopy
TM	Transition Metal
TPD	Temperature Programmed Desorption
UHV	Ultra-High Vacuum
XPD	X-ray Photoelectron Diffraction
XPS	X-ray Photoelectron Spectroscopy